Metabolic Flux, Transport Activity, and Subcellular Communication
in Intact Hearts from Dynamic ^{13}C NMR Spectroscopy

by

Xin Yu

Bachelor of Science, Electrical Engineering
University of Science and Technology of China (1986)

Master of Science, Electrical Engineering
The Johns Hopkins University (1991)

Submitted to the Department of Nuclear Engineering and
the Harvard-MIT Division of Health Sciences and Technology
in Partial Fulfillment of the Requirements for the Degree of

DOCTOR OF SCIENCE
in RADIOLOGICAL SCIENCES

at the
Massachusetts Institute of Technology
January 1996

The author hereby grants to MIT permission to reproduce and to distribute publicly paper and
electronic copies of this thesis document in whole or in part.

Signature of Author _____

Department of Nuclear Engineering
Harvard-MIT Division of Health Sciences and Technology
ary, 1996

Certified by __

E. Douglas Lewandowski, Ph.D.
Thesis Supervisor

Accepted by _____

Jeffrey P. Freidberg, Ph.D.
Chairman, Graduate Committee

Approved by _____

David G. Cory, Ph.D.
Reader, Thesis Committee

Approved by _____

Bruce R. Rosen, M.D., Ph.D.
Reader, Thesis Committee

Approved by _____

Nathaniel M. Alpert, Ph.D.
Reader, Thesis Committee

TO THE MEMORY OF MY GRANDMOTHER

SHIZHU JIN

Metabolic Flux, Transport Activity, and Subcellular Communication in Intact Hearts from Dynamic ^{13}C NMR Spectroscopy

by

Xin Yu

Submitted to the Department of Nuclear Engineering and the Harvard-MIT Division of Health Sciences and Technology on January 12, 1996 in Partial Fulfillment of the Requirements for the Degree of Doctor of Science in Radiological Sciences

ABSTRACT

The control of oxidative metabolism was studied using carbon-13 (^{13}C) nuclear magnetic resonance (NMR) spectroscopy to determine the rate-limiting steps in ^{13}C labeling of glutamate. ^{13}C NMR spectra were acquired from isolated rabbit hearts perfused with either 2.5 mM [2-^{13}C] acetate or 2.5 mM [2-^{13}C] butyrate, and with or without KCl arrest. The tricarboxylic acid (TCA) cycle flux and the interconversion rate between α-ketoglutarate and glutamate were determined by least-square fitting of a kinetic model to NMR data. Rates were compared to flux through glutamate-oxaloacetate transaminase (GOT). Despite similar oxygen use, hearts oxidizing butyrate showed delayed incorporation of ^{13}C label into glutamate and lower TCA cycle flux due to the influence of β-oxidation: 8.0±0.2 µmoles/min/g dry weight with butyrate versus 10.5±0.4 with acetate at normal workload; 1.7±0.1 with butyrate versus 2.9±0.1 with acetate at potassium arrest (mean±SD). The interconversion rate between α-ketoglutarate and glutamate ranged from 4.1±0.9 (butyrate+KCl) to 10.7±1.0 µmoles/min/g dry weight (acetate), at least 20-fold slower than the flux through GOT, and this proved to be the rate-limiting step in glutamate labeling. The results indicate that dynamic ^{13}C NMR is sensitive not only to TCA cycle flux but also to metabolite transport rate across the mithochondrial membrane.

To explore the effect of altered transport rates on the kinetics of glutamate labeling, metabolite exchange across the mitochondrial membrane was observed with ^{13}C NMR spectroscopy in hearts oxidizing 2.5 mM [2-^{13}C] butyrate at normal (no lactate) or high cytosolic redox state (2.5 mM lactate). High cytosolic redox state showed little effect on substrate utilization and TCA

cycle activity. The TCA cycle flux was 9.7±0.5 µmoles/min/g dry weight with butyrate only and 10.2±0.3 with butyrate plus lactate. However, lactate induced a more than four-fold increase in the interconversion rate, from 3.1±0.2 µmoles/min/g dry weight to 14.3±2.0. These data indicate increased metabolite transport across the mitochondrial membrane due to stimulated malate-aspartate shuttle activity in response to elevated cytosolic redox state.

Thesis Supervisor: Dr. E. Douglas Lewandowski
Title: Assistant Professor of Radiology
                               Massachusetts General Hospital
                               Harvard Medical School

Acknowledgments

I would like to acknowledge the efforts of those people without whom this thesis would not have been possible.

It has been a wonderful experience to be a student of Professor E. Douglas Lewandowski. Doug's outstanding guidance was essential to the success of this project. His genuine concern for the well being of his student made Doug an excellent mentor whom I have always been able to count on for advice and support.

I am indebted to all the collaborators at MGH for teaching me the techniques necessary for this work. Dr. Nathaniel M. Alpert served as a member of my thesis committee and has guided each important step in developing the kinetic analysis method. Mr. Lawrence T. White has taught me all the experimental techniques from animal surgery, NMR data acquisition, tissue extraction, to enzymatic analysis. Without his hard working, this thesis would not have been finished within two and half years.

I thank Professor Bruce R. Rosen and Professor David G. Cory, members of my thesis committee, for their excellent suggestions and fruitful discussions. Although not directly involved in this work, they have provided enormous help with their expertise in NMR and its medical applications. Also deserving special recognition is Professor Thomas J. Brady, Director of MGH-NMR center. Tom's encouraging attitude and good spirit allowed me to grow professionally and made my research at MGH-NMR center an enjoyable experience.

I am grateful to my parents for their sacrifice and support. Many of my teachers back in China, both in high school and in college, have influenced me at different stages of my life. I am thankful to them for their effort and dedication to educating the younger generations.

I would like to thank my husband Hui for his sharing my anxieties and for his understanding of me working through many late nights and weekends. His criticisms of my work have always been as valuable as his encouragement. I feel most fortunate that we have had the chance to go through the ups and downs of graduate school at MIT together. This will be part of our most valuable memories as we continue our journey into this new world.

This thesis is prepared while a new life is forming inside me. It is with all the love and good wishes that I await his/her coming into my life.

Table of Contents

List of Symbols and Abbreviations

ADP	adenosine 5'-diphosphate
ATP	adenosine 5'-triphosphate
ATA	alanine aminotransferase
ATT	aspartate aminotransferase
ATPase	adenosine triphosphatase
CoA	coenzyme A
F_1	interconversion rate between α-ketoglutarate and glutamate
F_2	interconversion rate between oxaloacetate and aspartate
FAD	flavin adenine dinucleotide, oxidized form
$FADH_2$	flavin adenine dinucleotide, reduced form
Fc	fraction of ^{13}C enriched acetyl-CoA entering the TCA cycle
GOT	glutamate-oxaloacetate transaminase
GTP	guanosine 5'-triphosphate
HR	heart rate
LDH	lactate dehydrogenase
LVDP	left ventricular developed pressure
MDH	malate dehydrogenase
MVO_2	oxygen consumption
NAD^+	nicotinamide adenine dinucleotide, oxidized form
NADH	nicotinamide adenine dinucleotide, reduced form
NMR	nuclear magnetic resonance
NOE	nuclear Overhauser enhancement
OAA	oxaloacetate
PCr	phosphocreatine
PDH	pyruvate dehydrogenase
P_i	inorganic phosphate
RPP	rate-pressure-product
TCA	tricarboxylic acid
V_{TCA}	TCA cycle flux
y	ratio of anaplerotic flux to citrate synthase flux

Chapter 1

Introduction

"Organisms, composed of material which is characterized by the utmost inconstancy and unsteadiness, have somehow learned the methods of maintaining constancy and keeping steady in the presence of conditions which might reasonably be expected to prove profoundly disturbing."

— Walter B. Cannon, *"The Wisdom of the Body"*

Myocardial performance in functioning heart is closely related to the metabolic events in cardiac cells. Like any other organs, the heart consists of a complex system of interactive proteins, energy-providing intermediates, membranes, ions, and signal molecules, all of which are in a constant state of flux. Heart muscle has retained its ability to adapt to environmental changes by changing flux through metabolic pathways to maintain its state of equilibrium. And the balance of energy production and utilization is therefore achieved in support of contractile function. Only the most severe environmental changes, such as those induced by an interruption of oxygen supply, result in a collapse of energy production. Hence, it is important to understand how the pathophysiological state of the myocardium is translated into the cell organelle to coordinate the metabolic activity of the myocardium.

Substrate metabolism in the heart has been the subject of intense research since the beginning of the century. A great deal of the detailed understanding of metabolic pathways has come from studies on isolated enzymes and on organelles. With the search for the relationship between several co-existent pathways and their regulation in intact heart, progress in the understanding of metabolic regulation has always been closely linked to advances in biochemical and physiological methods. Among these exciting advances, nuclear magnetic resonance (NMR) spectroscopy has rapidly become a powerful tool in the study of cardiac metabolism, largely due to its non-invasive nature and being chemically specific. These unique features allow simultaneous assessment of metabolic and contractile functions in intact, beating heart.

The work presented in this thesis aimed at developing new analysis techniques in the evaluation and interpretation of data obtained from dynamic carbon-13 (^{13}C) NMR spectroscopic studies. A kinetic model was

developed to facilitate the analysis of dynamic ^{13}C NMR data. The model was extensively tested by introducing various metabolic perturbations to the chosen physiological model. Experimental methods, including the acquisition and analysis of NMR data, the evaluation of physiological function and metabolic states of the tissue, and the biochemical analysis of tissue metabolism, were established. The work explored the potential of using dynamic ^{13}C NMR technique to investigate metabolic communications between subcellular compartments.

Following this introduction, various experimental components of this work are discussed in Chapter 2. Chapter 3 describes the construction of a mathematical model and the optimization technique employed in kinetic analysis. Some practical considerations in using this technique are also discussed. The results derived from applying kinetic analysis to the interpretation of NMR data are presented in Chapter 4. Furthermore, the potential for using ^{13}C NMR spectroscopic method to monitor metabolite transport between subcellular compartments is explored in Chapter 5, followed by a brief summary and the discussion of some future research directions in Chapter 6.

1.1 Physiological Functions and Intermediary Metabolism

The heart converts chemical energy into mechanical energy to develop pressure and to pump blood. The main purpose of cardiac metabolism is to provide energy to support rhythmic contraction, ion transport, biosynthesis and degradation. Like any other living organ, the immediate source of chemical energy in myocardium is in the form of adenosine triphosphate (ATP), a molecule with high energy bonds. The free energy in ATP is utilized by the controlled hydrolysis of ATP to adenosine diphosphate (ADP) and inorganic phosphate (P_i) by various adenosine-triphosphatases (ATPases) in the cytosol to perform work. The tissue content of ATP is normally around 20 μmoles/g dry weight, and the heart muscle utilizes 1400 μmoles ATP/min/g dry weight (25). Thus, under steady state conditions, ATP has to be continuously regenerated from its breakdown products, ADP and P_i. Because the heart is at constant rhythmic contraction, the rate of ATP turnover in the heart is far greater than in other organs of the mammalian body. It was estimated that a human heart produces 35 kg of ATP in the

course of 24 hours, more than 100 times its own weight and more than 10,000 times the amount of ATP stored in the heart (122).
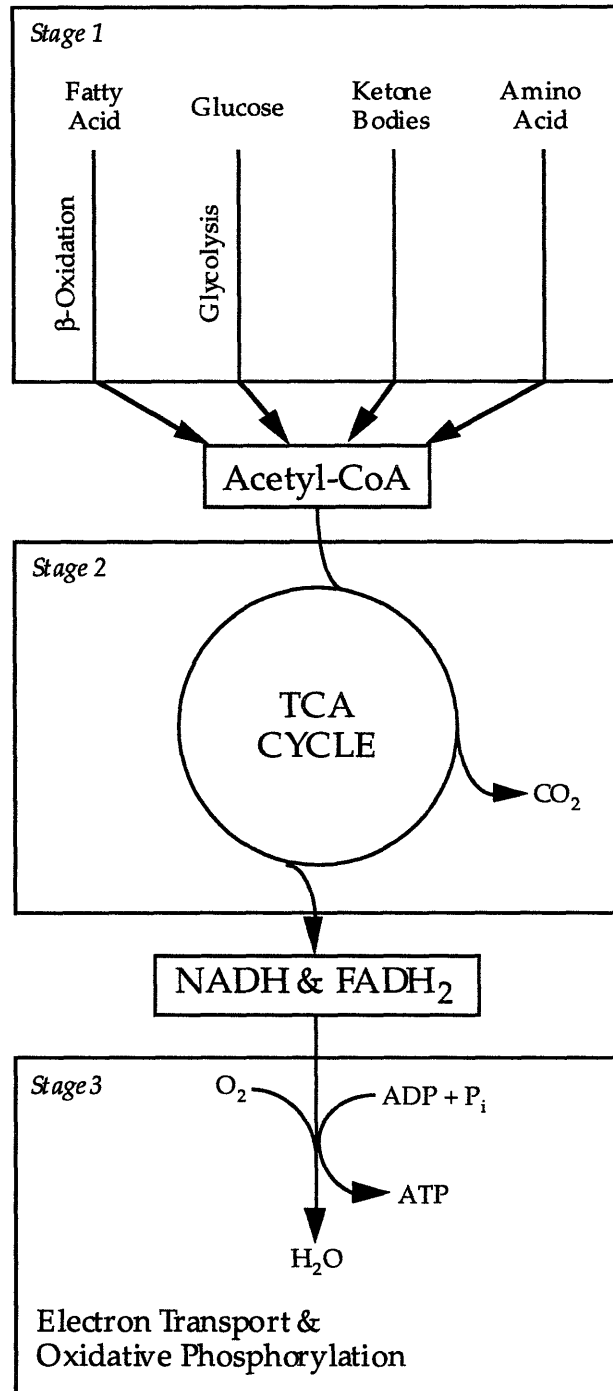

Figure 1.1 Stages of cardiac energy metabolism. The first stage comprises all pathways leading to acetyl-CoA; the second stage is the oxidation of acetyl-CoA in the TCA cycle; the third stage consists of the flow of electrons down the respiratory chain leading to release of free energy.

The major source of ATP in myocardium is oxidative phosphorylation of ADP coupled to the electron transport chain, phosphorylation of ADP in glycolysis and the tricarboxylic acid (TCA) cycle, and by the action of creatine kinase (46, 92). Quantitatively, oxidative phosphorylation is the main source of ATP. Oxidative phosphorylation of ADP depends on the production of electron rich reducing equivalents, i.e. flavin adenine dinucleotide ($FADH_2$) and nicotinamide adenine dinucleotide (NADH), and the transfer of electrons along the electron transport chain. Reducing equivalents are produced in the process of substrate catabolism to acetyl-CoA and subsequent oxidation of the acetyl group in the tricarboxylic acid (TCA) cycle. Cardiac metabolism can, therefore, be grouped into three stages: the formation of acetyl-CoA, the TCA cycle, and the oxidative phosphorylation (Figure 1.1).

The end-product of stage 1 is the formation of acetyl-CoA that prepares carbons for oxidation. The synthesis of acetyl-CoA is irreversible and is under close control by hormonal, cation and substrate level regulation. Stage 2 consists of the oxidation of acetyl-CoA to CO_2 and the production of reducing equivalents in the TCA cycle. In stage 3, further oxidation of NADH and $FADH_2$ generated in the TCA cycle is accomplished by the transfer of electrons down the electron transport chain, or the respiratory chain, generating an electrochemical gradient that provides the free energy for ATP synthesis.

1.1.1 Fatty Acid Metabolism

Under aerobic conditions, mammalian heart is capable of deriving energy from a variety of fuel sources such as fatty acids, glucose, lactate, ketone bodies, and even certain amino acids (25). Among these, free fatty acids are the preferred substrate (115). The biochemical strategy of fatty acid oxidation was discovered by Franz Knoop in 1904 (50), long before the advent of modern biochemical techniques involving enzyme purification or the use of radioactive tracers. However, it was not until after 1950, following the discovery of coenzyme A, that the enzymes of fatty acid oxidation were isolated and their reaction mechanisms elucidated (120).

The complete oxidation of fatty acid requires first its activation to acyl-CoA in the extramitochondrial compartment. This activation process is an ATP-dependent reaction and is catalyzed by a family of at least three chain length specific acyl-CoA synthetase.

Fatty acid + ATP + HSCoA $\xleftrightarrow{\text{acyl-CoA synthetase}}$ Acyl-CoA + AMP + PP_i
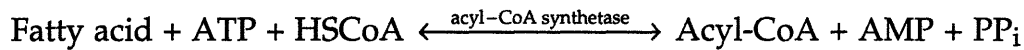
The acyl-CoA is then transported into the mitochondrial matrix to be oxidized (11). Since acyl-CoA molecules cannot penetrate the inner mitochondrial membrane, the transfer of acyl-CoA into mitochondria requires the participation of two membrane-bound enzymes called carnitine acyltransferases (Figure 1.2). Carnitine acyltransferase I, located on the cytosolic side of the mitochondrial membrane, transfers acyl-CoA to acyl-carnitine. Acyl-carnitine is then transported into mitochondria by carnitine carrier. Once inside the mitochondrial matrix, the acyl-carnitine is reconverted to carnitine and acyl-CoA by carnitine acyltransferase II located on the inner side of the mitochondrial membrane. Carnitine formed by the latter reaction is then transported back into the cytosol where it exchanges for more acyl-CoA. The rate of this transport process is determined mainly by the concentrations of the reactants.
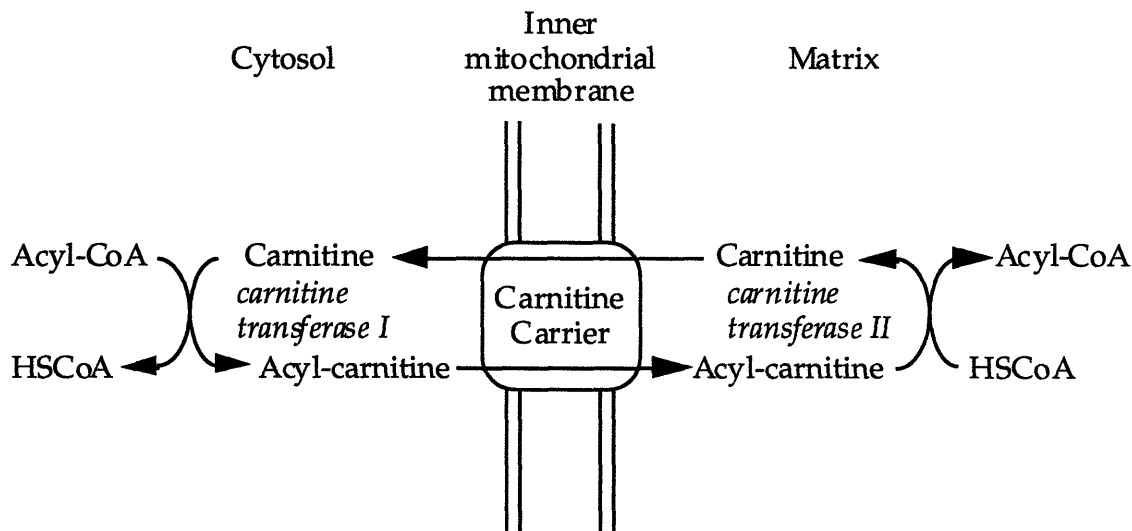
Figure 1.2 The transport of fatty acids into the mitochondrion. Fatty acid is first activated to acyl-CoA in the cytosol. The acyl group of a cytosolic acyl-CoA is transferred to carnitine thereby releasing the CoA to its cytosolic pool. The resulting acyl-carnitine is transported into the mitochondrial matrix by the transport system. The acyl group is then transferred back to a CoA molecule from the mitochondrial pool. And the product carnitine is returned to the cytosol.

Once inside the mitochondria, acyl-CoA enters the TCA cycle as acetyl-CoA. Acetyl-CoA is generated by the stepwise breakdown of long-chain fatty acyl chains by a series of reactions. This process is called β-oxidation, it

involves four reactions that are catalyzed by different enzymes and require several cofactors including CoA, FAD, and NAD$^+$ (Figure 1.3).

$$CH_3 - (CH_2)_n - CH_2 - CH_2 - \overset{\overset{\displaystyle O}{\|}}{C} - S - CoA \qquad \text{Fatty acyl-CoA}$$

acyl-CoA
dehydrogenase — FAD ⟶ FADH$_2$

$$CH_3 - (CH_2)_n - \underset{\underset{\displaystyle H}{|}}{\overset{\overset{\displaystyle H}{|}}{C}} = \overset{}{C} - \overset{\overset{\displaystyle O}{\|}}{C} - S - CoA \qquad \textit{trans}\text{-}\Delta^2\text{-Enoyl-CoA}$$

enoyl-CoA
hydratase — H$_2$O

$$CH_3 - (CH_2)_n - \underset{\underset{\displaystyle OH}{|}}{\overset{\overset{\displaystyle H}{|}}{C}} - CH_2 - \overset{\overset{\displaystyle O}{\|}}{C} - S - CoA \qquad \text{3-L-Hydroxyacyl-CoA}$$

3-L-hydroxyacyl-CoA
dehydrogenase — NAD$^+$ ⟶ NADH+H$^+$

$$CH_3 - (CH_2)_n - \overset{\overset{\displaystyle O}{\|}}{C} - CH_2 - \overset{\overset{\displaystyle O}{\|}}{C} - S - CoA \qquad \beta\text{-Ketoacyl-CoA}$$

β-ketoacyl-CoA
thiolase — CoASH

$$CH_3 - (CH_2)_n - \overset{\overset{\displaystyle O}{\|}}{C} - S - CoA \quad + \quad CH_3 - \overset{\overset{\displaystyle O}{\|}}{C} - S - CoA$$

Fatty acyl-CoA
(2 C atomes shorter)   Acetyl-CoA

Figure 1.3 The β-oxidation pathway of fatty acyl-CoA. Each turn of β-oxidation involves four reactions, two of oxidation, one of hydration, and one of thiolysis. Each turn shortens fatty acyl-CoA by two carbons by releasing one acetyl-CoA molecule. The shortened acyl-CoA is then able to reenter another turn of β-oxidation. This process continues until the fatty acyl-CoA is converted entirely to acetyl-CoA.
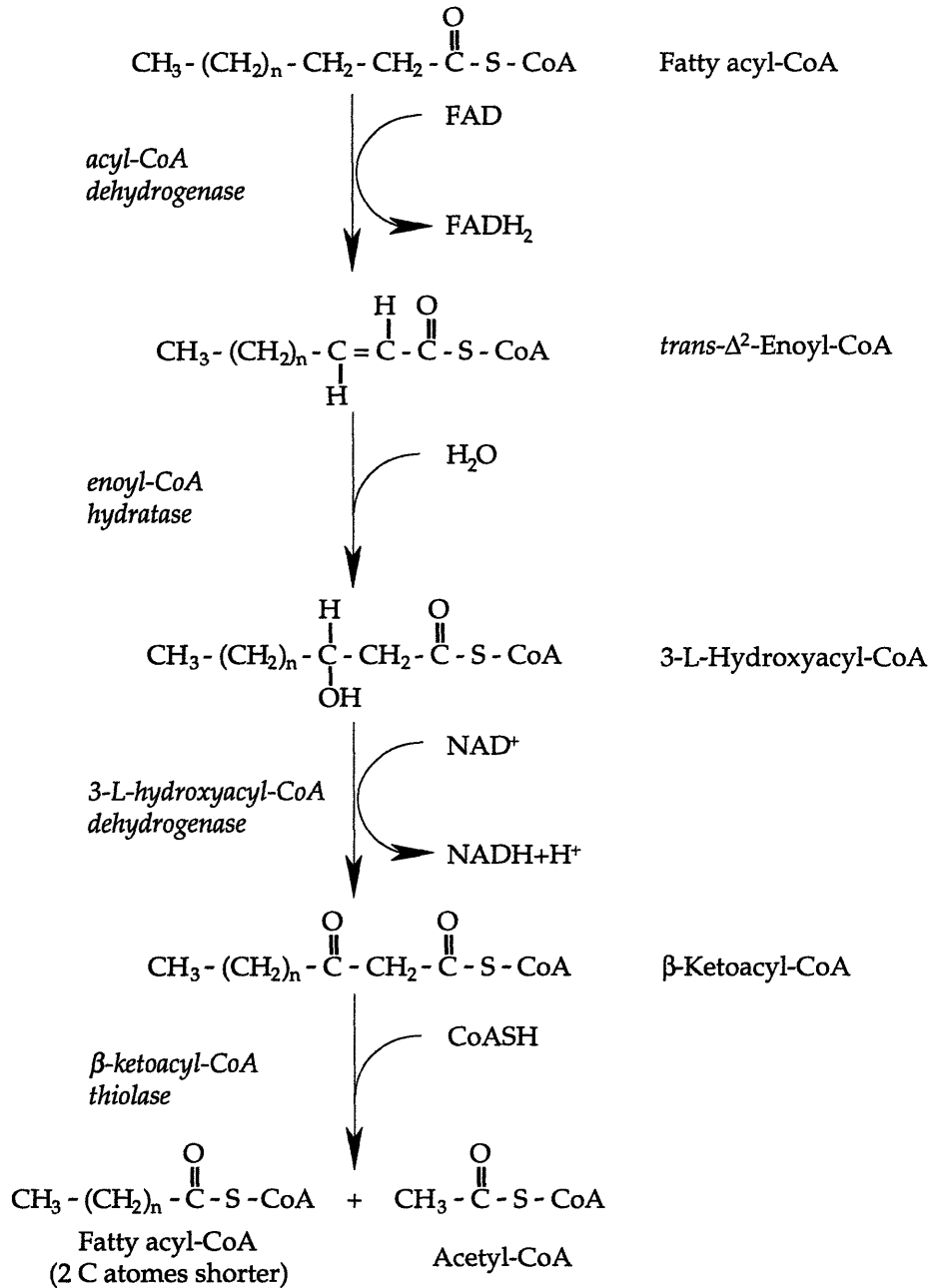
The four sequential reactions in β-oxidation are very tightly coupled to each other, so that the concentrations of the fatty acyl intermediates are normally very low. The energy that becomes available in the two oxidative steps of β-oxidation is trapped in reduced $FADH_2$ and NADH; these generate ATP when they are subsequently oxidized in the electron transport chain coupled to oxidative phosphorylation.

Regulation of β-oxidation in intact cells occur through the availability of acyl-CoA and oxidized NAD^+ and FAD (12). The rate of β-oxidation is geared to flux through the TCA cycle and to the rate of oxidative phosphorylation. A high $NADH/NAD^+$ ratio inhibits the 3-L-hydroxyacyl-CoA dehydrogenase. The presence of succinate inhibits the overall rate of β-oxidation in isolated mitochondria by competing for FAD (86). Under normal conditions, the rate of β-oxidation is much faster than that of fatty acid activation, so that the overall rate of fatty acid oxidation in the well-oxygenated heart is normally governed by the reactions responsible for fatty acid entry into the mitochondria.

The metabolism of short-chain fatty acids (C_{4-10}) is different from the long-chain fatty acids in that their activation to acyl-CoA by specific acyl-CoA synthetases takes place in the mitochondrial matrix. The short-chain fatty acids therefore bypass the extramitochondrial processes and the carnitine-dependent transfer mechanism (13, 36). Their metabolism consequently appears to be subject to little regulation.

1.1.2 The Tricarboxylic Acid Cycle and Its Regulation

The tricarboxylic acid cycle (TCA cycle), also known as the citric acid cycle or the Krebs cycle, accounts for the major portion of carbohydrate, fatty acid, and amino acid oxidation and generates numerous biosynthetic precursors. Discovered by Hans Krebs in 1937 (53), the discovery of the TCA cycle is ranked as one of the most important classical achievements in metabolic chemistry.

Reactions of the TCA cycle are shown in Figure 1.4. Most of the enzymes for the TCA cycle are soluble enzymes in the mitochondrial matrix (38). The major role of the TCA cycle in heart is to accomplish the oxidation of the acetyl group of acetyl-CoA to CO_2 and water. Reducing equivalents are

thereby produced in the mitochondria, their reoxidation by the enzymes of the electron transport chain being coupled to ATP synthesis. A small amount of ATP is also generate by transferring the high energy bond from guanosine triphosphate (GTP) to ADP. In summary, one turn of the TCA cycle results in the following chemical transformation:

1. One acetyl group is oxidized to two molecules of CO_2;
2. Three molecules of NAD^+ are reduced to NADH;
3. One molecule of FAD is reduced to $FADH_2$;
4. One high-energy phosphate group is produced as GTP.
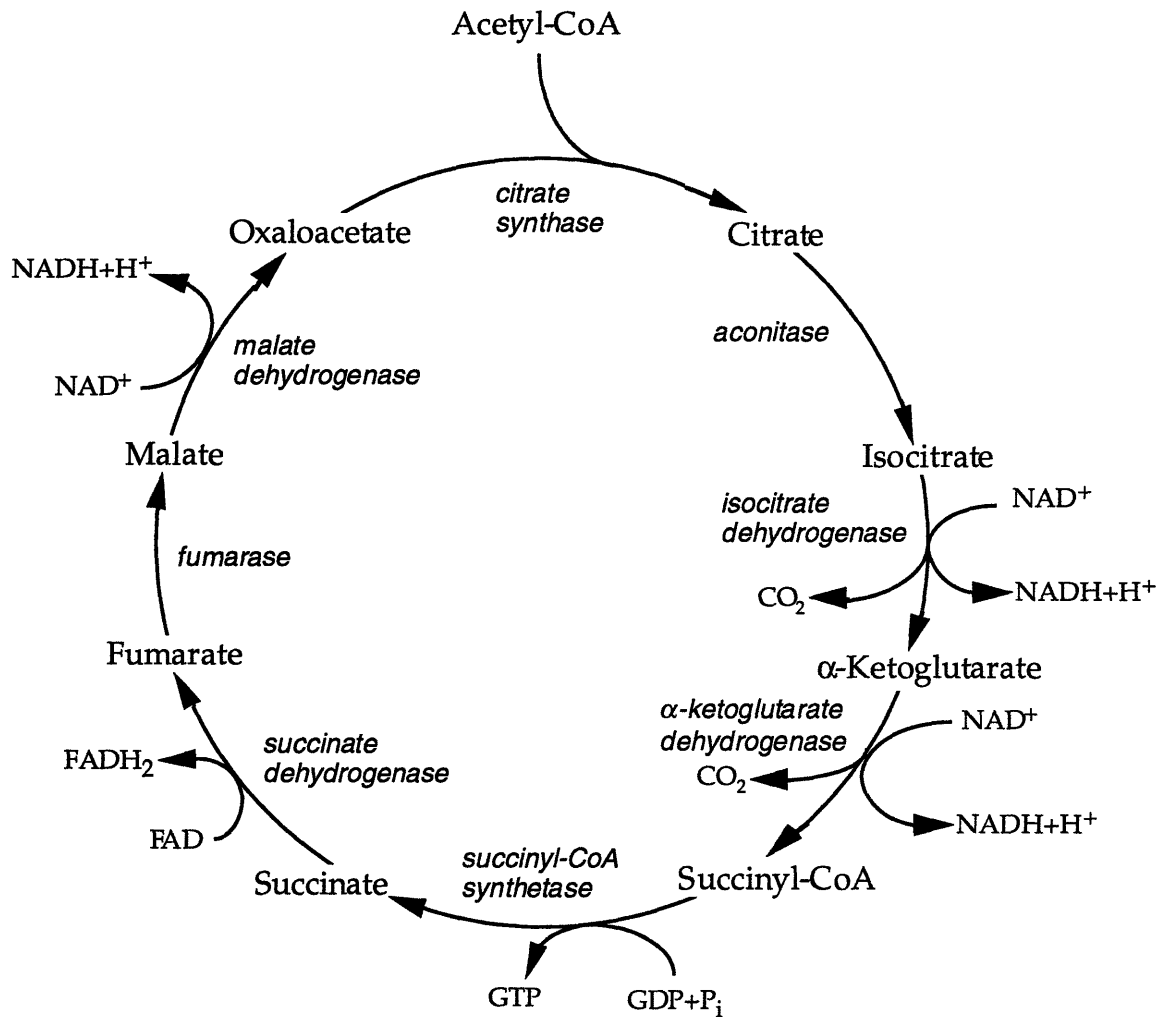
Figure 1.4 The TCA cycle pathway. Condensation of the two-carbon acetyl group from acetyl-CoA with the four-carbon oxaloacetate yields a six-carbon citrate. The latter, after isomerization to isocitrate, is oxidized and decarboxylated. The resulting five-carbon α-ketoglutarate is oxidized and decarboxylated in a reaction that yields succinyl-CoA. Oxaloacetate is regenerated after succinyl-CoA undergoes two steps of oxidation and one step of hydration.

Acetyl groups are thereby completely oxidized to CO_2 with the following stoichiometry:

$$Acetyl\text{-}CoA + 3NAD^+ + FAD + GDP + Pi \longrightarrow$$
$$2CO_2 + CoA + 3NADH + FADH_2 + GTP$$
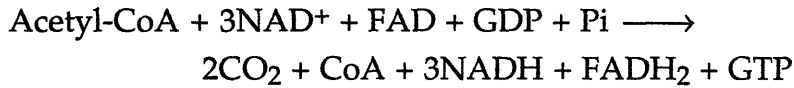
Regulation of the TCA cycle is associated with feedback interactions that allow flux through the cycle to keep pace with the energy expenditure by the heart. Establishing the rate-determining steps of the TCA cycle is difficult because most of the cycle's metabolites are present in both mitochondria and cytosol and we do not know their distribution between these two compartments. Many of the conclusions have been drawn either from studies of isolated mitochondria or by making the assumption that metabolites distribute equally between the two compartments.

Three enzymes are likely to function far from equilibrium under physiological condition and act as the regulatory enzymes of the TCA cycle (135): citrate synthase, isocitrate dehydrogenase, and α-ketoglutarate dehydrogenase. These enzymes are controlled almost entirely in three simple ways: substrate availability, production inhibition, and competitive feedback inhibition by intermediates further along the cycle.

Citrate synthase, which catalyzes the condensation of acetyl-CoA and oxaloacetate, is one of the earliest sites to be proposed as a key point of regulation (3, 57). Acetyl-CoA and oxaloacetate are present in mitochondria at concentrations that do not saturate citrate synthase (124). The metabolic flux through the enzyme therefore varies with substrate concentration and is subject to control by substrate availability. In addition, citrate synthase is inhibited by an allosteric effect of ATP.

Isocitrate dehydrogenase controls the production of α-ketoglutarate from isocitrate. It is strongly inhibited by NADH. *In vitro* studies also suggest that ADP acts as an allosteric activator of isocitrate dehydrogenase by decreasing its apparent K_m for isocitrate. ATP, on the other hand, inhibits this enzyme. Thus, a fall in the high-energy phosphate levels within the cell accelerates the TCA cycle. However, whether high-energy phosphate levels also act as regulatory factors in intact heart is not clear, as studies using nondestructive phosphorus-31 nuclear magnetic resonance techniques demonstrated *in vivo*
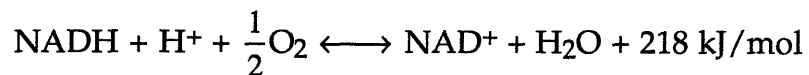
that there is little correlation between workload and ATP, ADP or P_i levels (4).

α-Ketoglutarate dehydrogenase is also strongly inhibited by its product, NADH and succinyl-CoA. Succinyl-CoA production is inhibited in the anaerobic heart because of NADH. Succinyl-CoA also competes with acetyl-CoA in the citrate synthase reaction. In addition, Ca^{2+} activates both isocitrate dehydrogenase and α-ketoglutarate dehydrogenase.

At metabolic steady state, all the TCA cycle intermediates are at constant levels. Changes in workload or substrate utilization can induce a change in these metabolite concentrations. However, since the entry of two carbon acetyl group into the TCA cycle is balanced by the release of two CO_2 molecules, other reactions must be responsible for the regulation of TCA cycle intermediates. Reactions that replenish the TCA cycle intermediates are called anaplerotic reactions, and reactions contributing to net efflux of carbon from the TCA cycle are called cataplerotic reactions (70, 95). Besides regulating intermediate pool sizes of the TCA cycle, these two types of reactions are also involved in both the feedback control of TCA cycle flux and the metabolic communication between the mitochondrial and cytosolic compartments (52).

1.1.3 Electron Transport and Oxidative Phosphorylation

Oxidative phosphorylation provides quantitatively the most important mechanism by which energy derived from fuel molecules can be transferred to ATP. The overall reaction of oxidative phosphorylation can be viewed as the transfer of hydrogen from NADH and $FADH_2$ to oxygen.

$$NADH + H^+ + \frac{1}{2}O_2 \longleftrightarrow NAD^+ + H_2O + 218 \text{ kJ/mol}$$

and

$$FADH_2 + \frac{1}{2}O_2 \longleftrightarrow FAD + H_2O + 157 \text{ kJ/mol}$$

The standard free energy required to synthesize 1 mole of ATP from ADP and P_i is 30.5 kJ/mol. The standard free energy of oxidation of NADH, when coupled to ATP synthesis, is therefore sufficient to drive the formation of several moles of ATP. This coupling is achieved by an electron transport

chain in which electrons are passed through three protein complexes containing redox centers, or cytochromes, with progressively greater electron affinity. The free energy in NADH and $FADH_2$ is harnessed to create an electrochemical gradient by the movement of protons out of the mitochondria.

The proton electrochemical gradient across the mitochondrial membrane is used in the synthesis of ATP by proton-translocating ATP synthase, or F_0F_1-ATPase, which projects from the surface of the inner mitochondrial membrane into the matrix. Transduction of the electrochemical energy of the proton gradient into the chemical bond energy of ATP occurs when proton translocation energizes ATP synthase, which is followed by a subsequent step in which this energy is transferred to a high-energy bond between ADP and P_i. In this way, the large overall free energy change in NADH and $FADH_2$ is broken up into three smaller packets, each of which is coupled with ATP synthesis. Oxidation of one NADH therefore results in the synthesis of three ATPs. Oxidation of $FADH_2$, whose entrance into the electron-transport chain is regulated by a fourth protein complex, is similarly coupled to the synthesis of two ATPs. Therefore, when the oxidation of acetyl group in the TCA cycle is coupled to oxidative phosphorylation, a total of 12 ATPs are generated for the oxidation of one acetyl molecule, with the consumption of two oxygen molecules.

1.2 Intracellular Compartmentation and Metabolic Communication between Intracellular Compartments

Like any other eukaryotic cells, cardiac cells contain extensive internal membranes that define a collection of highly organized, subcellular structures called organelles, each with a specialized function. Among these numerous organelles, mitochondria, equipped with the key enzymes of oxidative metabolism, are the sites of energy production. The primary role of mitochondria in the myocardium is to supply the cardiac cells with ATP for contraction and for the maintenance of ion homeostasis, protein synthesis, and other important cellular functions. Since the energy requirement is much higher in myocardium than in any other tissues due to constant rhythmic contraction, mitochondria are quite abundant in cardiac cells (83, 99, 135). It has been estimated that the total mitochondrial content in cardiac

cells is close to 250 mg/g dry tissue weight, and mitochondrial protein is 40% of the total noncollagenous protein of cardiac tissue (44).

Electron microscopic studies reveals that mitochondrion has two membranes: a smooth outer membrane and a highly folded inner membrane. Thus the mitochondrion contains two compartments, the inner membrane space and the internal matrix space. The enzymes that catalyze the reactions in oxidative metabolism are located in either the gel-like matrix or the inner mitochondrial membrane. The inner membrane space provides a controlled compartment for some metabolic enzymes such as creatine kinase and nucleoside diphosphate kinase (83).

The outer membrane provides structural support of the organelle. It is relatively porous and does not limit permeability of molecules up to 10,000 daltons (83). The inner membrane is the most active compartment of the mitochondria. It is selectively permeable and thus controls the transport of essential components into the mitochondria. This function is accomplished by various carrier systems or translocases such as the adenine nucleotide translocase, the phosphate carrier, the calcium carrier and the substrate transporters, the mono- and dicarboxylate carriers and the carnitine-acylcarnitine translocase. These carriers or translocases are essential for the function of the mitochondrion, because all the enzymatic reactions related to ATP synthesis take place in either the inner membrane or in the matrix space.

Glycolysis takes place in the cytosol and also generates reducing equivalents. However, while the NADH formed in mitochondria has direct access to the enzymes of oxidative phosphorylation, NADH produced in the cytosol must be transported into the mitochondria before it can be reoxidized, and the reoxidized NAD^+ must be returned to the cytosol since it is essential for glycolysis. Because the inner mitochondrial membrane is not permeable to this coenzyme, the exchange of NADH produced in the cytosol for NAD^+ produced in the mitochondria cannot take place by simple diffusion. In myocardium, transfer of NADH into the mitochondria in exchange for NAD^+ is accomplished by a special membrane transport system, the malate-aspartate shuttle (105).
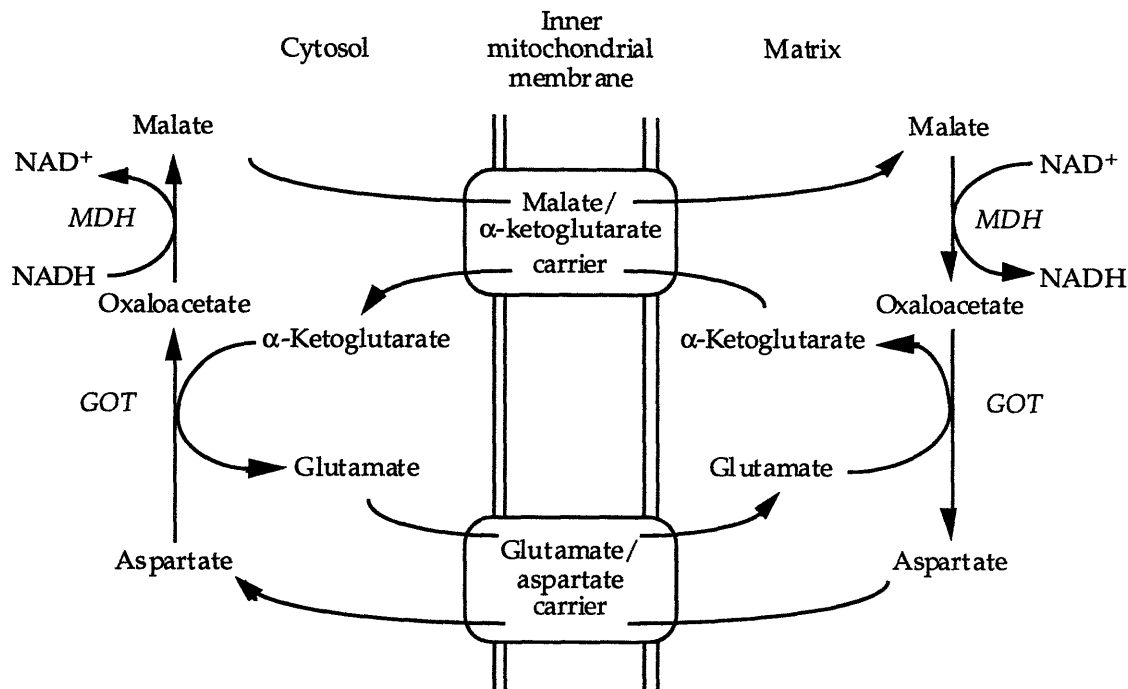
Figure 1.6 The malate-aspartate shuttle. The operation of the shuttle involves oxidation-reduction and transamination reactions in both cytosolic space and mitochondrial matrix, accompanied by the efflux of aspartate and α-ketoglutarate and the influx of glutamate and aspartate. MDH: malate dehydrogenase; GOT: glutamate-oxaloacetate transaminase.

The malate-aspartate shuttle involves not only oxidation and reduction reactions, but also transaminations (Figure 1.6). The reduced NADH formed in the cytosol is oxidized to NAD^+ by the coupled reduction of oxaloacetate to malate catalyzed by malate dehydrogenase (MDH). Malate is then transported into the mitochondria by the malate/α-ketoglutarate carrier. Once inside the mitochondria, malate is reoxidized to oxaloacetate. In the mean time, NADH is regenerated. The net effect of this reaction is the same as if NADH from the cytosol were exchanged for NAD^+ in the mitochondria.

To complete the malate-aspartate cycle, additional reactions are needed to return the excess oxaloacetate from the mitochondria to the cytosol, since the inner mitochondrial membrane is impermeable to oxaloacetate. The glutamate-oxaloacetate transaminase (GOT) first converts mitochondrial oxaloacetate to aspartate with concomitant conversion of mitochondrial glutamate to α-ketoglutarate. Aspartate is then transported to the cytosol by the glutamate/aspartate carrier in exchange for cytosolic glutamate. Cytosolic aspartate is then converted back to oxaloacetate in conjunction with the

conversion of α-ketoglutarate to glutamate, thereby restoring the initial level of oxaloacetate in the cytosol.

Two carriers are involved in the malate-aspartate shuttle: the electroneutral malate/α-ketoglutarate carrier and the electrogenic glutamate/aspartate carrier. The malate/α-ketoglutarate carrier catalyzes the exchange of malate and α-ketoglutarate. As there is no net movement of electrical charge across the mitochondrial membrane, the exchange of malate for α-ketoglutarate can occur in both directions, yet the affinity for intra- and extra-mitochondrial substrates are different (117). On the contrary, besides the exchange of glutamate and aspartate, a proton is also transported with glutamate in glutamate/aspartate carrier mediated transport (58). Since there is a large negative potential across the mitochondrial membrane under physiological conditions, entry of glutamate and efflux of aspartate from the mitochondria is virtually a unidirectional process.

In addition to regulating the transport of reducing equivalents across the inner mitochondrial membrane, the malate-aspartate shuttle also provides means for metabolic control and the integration of the many individual catalytic reactions that are responsible for energy production in the heart. It influences the flux through the TCA cycle by modulating the concentrations of oxaloacetate and α-ketoglutarate within the mitochondria. Distribution of other intermediates provides additional means of communication between cytosolic and mitochondrial metabolism (61, 105, 137).

1.3 Tracing Metabolic Pathways by NMR Spectroscopic Methods

Since its discovery by Bloch and Purcell in 1946, nuclear magnetic resonance (NMR) has evolved into a highly successful tool of physics, chemistry, and biochemistry. In the last twenty years, NMR spectroscopy has become a widely used technique for the evaluation of cardiac biochemistry, function, and pathology (94). The value and role of NMR spectroscopy in solving biochemical problems derives from its exquisitely detailed informational content concerning the chemistry and physical environment of the component being detected. Because of the non-invasive nature of NMR spectroscopy, metabolic activities in intact organ system can be studied in conjunction with physiological measurements (2, 9, 35, 40). Of particular

interest is the information that can be obtained with phosphorus-31 (^{31}P) and carbon-13 (^{13}C) NMR.

^{31}P is by far the most commonly studied nucleus in cardiac NMR spectroscopy. ^{31}P isotope is present at 100% natural abundance and requires no isotopic enrichment for measurement. ^{31}P NMR allows measurement of cellular levels of ATP, phosphocreatine (PCr), and inorganic phosphate (P_i) as well as intracellular pH estimates (37). Furthermore, using magnetization transfer techniques, unique information has been obtained concerning the rate constants for physiologically important processes such as phosphate exchange via creatine kinase in the intact heart (7, 8). Thus, ^{31}P NMR methods can directly investigate the mechanism whereby the myocardium synthesizes, transfers, and uses the high-energy phosphate compounds for contraction.

^{13}C NMR spectroscopy is especially useful for studying metabolic turnover, as well as the effects of drugs and hormones on such turnover. Unlike ^{31}P, ^{13}C is present naturally at only 1.1% and is 1.6% as sensitive as ^{1}H. Thus, the application of ^{13}C NMR requires the use of substrates enriched in ^{13}C to obtain adequate spectral sensitivity. However, enriched compounds are useful for determining the flux through a particular biochemical pathway or for following substrate metabolism in general, because any observed signal arises either from the exogenous label or from its metabolic products. This capability provides useful experimental control in evaluating specific metabolic pathways. Another major advantage of ^{13}C NMR is that ^{13}C resonances display a much wider chemical shift range than ^{1}H (~200 ppm versus ~10 ppm). This permits resolution of ^{13}C resonances in molecules that are structurally quite similar, whereas the corresponding ^{1}H resonances may overlap. Therefore, ^{13}C NMR provides unique and detailed information about tracer distribution in intermediary metabolites and allows more comprehensive mathematical modeling of the metabolic processes.

An important early contribution in ^{13}C NMR spectroscopy was the analysis of steady-state isotopomer distribution in certain metabolites, especially glutamate (69, 74-77, 110, 111). From high resolution ^{13}C NMR spectra of tissue extracts taken at steady-state conditions, the multiplet structures in glutamate resonance signals due to ^{13}C-^{13}C coupling allowed the

relative concentrations of the various isotopomers to be determined. The analysis of such isotopomer distribution allowed the relative contribution of various substrates to the overall TCA cycle flux, as well as relative anaplerotic flux to be calculated. These approaches, however, are limited in that they do not provide estimates of absolute metabolic fluxes. And the necessity for tissue sampling due to the requirement for high resolution spectrum also has limited its applications to *in vivo* studies.

Dynamic ^{13}C NMR spectroscopy allows absolute metabolic flux along a particular metabolic pathway to be estimated. As ^{13}C-enriched substrate is metabolized, ^{13}C label is transferred to various metabolic intermediates. The labeling pattern is dependent on the chemistry of the enzyme reactions, and the rate of labeling is determined by flux through the pathway and the pool sizes of the intermediates. From the ^{13}C NMR spectra, resonances attributable to specific carbon atoms of particular intermediates are identified by their chemical shifts. The area of the resonance peak, when corrected for nuclear Overhauser enhancement (NOE), is proportional to the ^{13}C content of the particular carbon site, and the fractional ^{13}C enrichment can be calculated if the intermediate pool size is known. The type of information obtained is similar to that obtained by use of ^{14}C isotopes, but with the advantages that the metabolites of interest need not be isolated, purified, and chemically degraded to obtain the fractional ^{13}C enrichment at each position within a molecule. More importantly, the ^{13}C NMR technique permits data to be obtained continuously and nondestructively while metabolism is in progress. Hence, integrated biochemical and physiological response of the tissue to external interventions may be explored.

Since its first application to cell suspensions in following metabolic routes of exogenous ^{13}C enriched substrates in 1972 (30), ^{13}C NMR spectroscopy has been applied to a wide range of biological systems including isolated cells (21, 22), perfused liver (20, 23) and heart (1, 18, 71, 112), and *in vivo* organs (34, 100, 116). It has generated widespread interest for application to laboratory investigations of intact organs and *in vivo* animal models (16). The first perfused heart study by ^{13}C NMR (1) showed that it is possible to detect enriched aspartate and glutamate signals and follow the time dependence of ^{13}C incorporation into these pools in hearts supplied with [2-^{13}C] acetate. Chance *et al.* measured the time dependence of ^{13}C fractional enrichment at

each carbon position in these same pools in freeze-clamped extracts of perfused hearts and fit the data to a mathematical model of the TCA cycle to obtain carbon flux information (17). Neurohr et al. (90) have demonstrated the feasibility of detecting ^{13}C-enriched glutamate signals from the heart of an open-chested guinea pig during intravenous infusion of [2-^{13}C] acetate. To date, numerous studies have exploited this unique technique to quantify several aspects of metabolism in intact heart at both normal (63, 65, 68, 100) and diseased state (18, 67, 71, 72, 132).

1.4 Motivations and Objectives

A disadvantage of NMR spectroscopy is its low sensitivity. Hence, the carbon resonance cannot be resolved above the base-line unless ^{13}C level is high. With present instrumentation, ^{13}C resonances can only be detected in intact tissues if their concentration exceeds a limit of about 0.5 mM. Since most TCA cycle intermediates are normally present in tissues below this concentration, and hence cannot be observed directly by NMR even with ^{13}C enrichment, current ^{13}C NMR technique relies almost exclusively on the observation of isotope incorporation into glutamate, a metabolite that is in constant exchange with TCA cycle intermediates through transamination with α-ketoglutarate. However, as glutamate itself is not a TCA cycle intermediate, glutamate labeling remains an indirect indicator of ^{13}C labeling of the TCA cycle intermediates. And the influence of isotope exchange rate between glutamate and α-ketoglutarate on isotope turnover within the glutamate pool is not well characterized.

Many of the studies have drawn their conclusion based on the assumption that α-ketoglutarate is in rapid exchange with glutamate (81, 82, 130, 132). Until now, this assumption has not been tested in intact tissues, although isolated enzyme measurements of liver glutamate-oxaloacetate transaminase (GOT), the enzyme that catalyzes this reaction, does show that the enzyme has a large V_{max} value (32, 33). Another frequently overlooked factor is that since about 90% of the glutamate is located in the cytosol (55), the labeling of glutamate also involves the transport of metabolites across the mitochondrial membrane through carrier mediated transporters. And the transport of metabolites is inevitably influenced by mitochondrial membrane potential and the redox-dependent malate-aspartate shuttle (105, 106). Whether this

transport is fast enough to be negligible in studies of intact tissues is even less well established. Thus, the evolution of presteady state ^{13}C NMR spectra is unlikely to be determined solely by TCA cycle activity and may, in fact, be dominated by metabolic communication between subcellular compartments.

In an effort to further the application of dynamic ^{13}C NMR spectroscopy, this work was aimed at targeting the above stated problems in presteady-state ^{13}C NMR observation of tissue metabolism. It was based on the hypothesis that dynamic observation of glutamate labeling is an index of the TCA cycle flux and can be used to ascertain rate limiting steps in metabolic pathway. In order to approach a solution to this problem, a mathematical model describing the kinetics of glutamate labeling was developed for the analysis and comprehensive evaluation of acquired NMR data. The model allowed absolute fluxes to be determined and rate-limiting steps in glutamate labeling to be identified through kinetic analysis of dynamic NMR data. The model was applied to evaluate variations in ^{13}C kinetics through manipulation of the TCA cycle flux by either workload or metabolic regulation, and the contribution of both the TCA cycle flux and the interconversion rate between α-ketoglutarate and glutamate to ^{13}C turnover in glutamate was compared. Finally, the potential of using dynamic ^{13}C NMR technique to observe other metabolic processes was also explored.

Chapter 2

Experimental Design

Described in this chapter are several experimental techniques used in this study, including preparation of physiological model, enzymatic assays for the analysis of tissue metabolites, and various NMR techniques. These experiments provide data and information necessary in the analysis of dynamic ^{13}C NMR data. The kinetic analysis method is discussed in a separate chapter (Chapter 3).

2.1 Physiological Model - Isolated Rabbit Heart

Isolated heart models are used to study myocardial metabolism without the complications of neurogenic input, plasma-borne hormones, and the metabolic activities of other organ systems. In well-oxygenated preparations, ventricular performance is stable for periods in excess of three hours with only slightly deterioration (87). In addition, isolated heart preparation allows frequent perfusate sampling during the time course of perfusion.

Among the available perfusion techniques, the Langendorff perfusion technique has become a widely used technique, particularly in conjunction with nuclear magnetic resonance spectroscopy (72, 114). First devised by Oscar Langendorff (54), the Langendorff perfusion refers to a preparation in which blood or any other oxygenated and substrate containing fluid appropriate to maintain cardiac activity was forced towards the heart through a cannula inserted into the ascending aorta. After passing through the coronary vascular system the perfusate flows out of the coronary sinus and the opened right atrium. Since the perfusate is supplied to the heart through the physiological ejection path, this technique is also referred to as retrograde perfusion technique. Originally, the cardiac ventricle was beating empty throughout the experiment. Hence, the heart was said to perform no defined work. By inserting a balloon catheter into the left ventricle, the heart can also perform isovolumic contraction. Unless special efforts are made to drain the left ventricle, intraventricular pressure increases to levels slightly above the perfusion pressure with each beat, due to a limited degree of ventricular filling, arising either from the Thebesian circulation or from incompetence of the aortic valve due to use of low viscosity perfusate.

The isovolumic Langendorff perfused heart model is not an ejecting heart preparation and as such "ejecting" heart model has been employed in the study of cardiac physiology. However, the Langendorff perfused heart model is frequently used in the study of both cardiac metabolism and mechanics. It has been shown that the bioenergetics and mechanics of ejecting and isovolumic perfused hearts are indistinguishable (107). One of the limitations of the typical "ejecting" heart model is that it is potentially unstable since perfusion of the coronary arteries is dependent on the contractile activity of the heart. Therefore, it is more difficult to maintain the heart at stable function due to experimental variations. In contrast, with the isovolumic Langendorff model coronary perfusion pressure is constant, regardless of contractile activity. Thus, the Langendorff perfused heart model is generally accepted for assessing the mechanics, coronary flow, and metabolism of the mammalian heart. It is a stable, highly reproducible, low work preparation (29, 138). Therefore, Langendorff perfused rabbit hearts were used in this study in order to have precise control over substrate availability and workload.

Since aerobic metabolism generates most of the ATP for myocyte contraction, myocardial oxygen consumption is coupled closely to myocardial energy production and mechanical work in the normal heart (85, 88). Oxygen consumption can therefore be used as an index of myocardial metabolic rate. Myocardial oxygen consumption (MVO_2) is calculated by following equation (85):

$$MVO_2 = \frac{(\text{Solubility of } O_2 \text{ at } 37°C) \cdot (\text{coronary flow}) \cdot \Delta pO_2}{(\text{weight of the heart})}$$

here ΔpO_2 is the arterio-venous O_2 difference in mmHg, it can be calculated from the difference in oxygen content of perfusion medium and coronary effluent. The solubility of oxygen in perfusate at 37°C and atmospheric pressure is about 0.0016 μmoles/ml/mmHg. If the coronary flow rate is expressed in ml/min, and the heart weight in grams of dry tissue, this will give MVO_2 in μmoles O_2/min/g dry tissue weight.

Contractile function, on the other hand, is frequently assessed by rate-pressure-product (RPP) which is defined as the product of heart rate (HR) and left ventricular developed pressure (LVDP), i.e. $RPP = HR \times LVDP$ (48). If

heart rate and left ventricular developed pressure are expressed in beats/min and mmHg respectively, rate-pressure-product has the unit of beats·mmHg/min, or simply mmHg/min. Numerous studies have characterized the relationship between myocardial oxygen consumption and cardiac workload in isolated heart (8, 51, 66, 85, 131). A linear relation exists between oxygen consumption and rate-pressure product over a wide range of cardiac work in several heart preparations (8, 66, 89). The slope of the relationship, or the ratio of oxygen consumption to rate-pressure-product, may be considered to represent an index of the heart's aerobic metabolic efficiency.

Dutch belted rabbits weighing between 550 and 700 g have been used. The animals were heparinized (1,000 units) and anesthetized with sodium pentobarbital (100 mg/kg, intraperitoneal injection). The abdominal cavity was opened by making a transverse incision just below the rib cage. The diaphragm was transected, and lateral incisions were made along both sides of the rib cage. Heart was then raised and excised. Immediately upon excision, the heart was immersed in a solution containing 20 mM KCl and 120 mM NaCl for cardioplegia at 0°C. During cardioplegia, the pericardium and excess fat was cut from the heart to permit cannulation. The aorta was then cannulated for retrograde perfusion at 100 cm hydrostatic pressure with a modified Krebs-Henseleit buffer. The buffer contained 116 mM NaCl, 4 mM KCl, 1.5 mM $CaCl_2$, 1.2 mM $MgSO_4$, 1.2 mM NaH_2PO_4, and 25 mM $NaHCO_3$. Adequate oxygen delivery was achieved by equilibrating the buffer with a 95% O_2 - 5% CO_2 gas mixture. The buffer has a physiological pH value of 7.4 and was kept at constant temperature of 37°C.
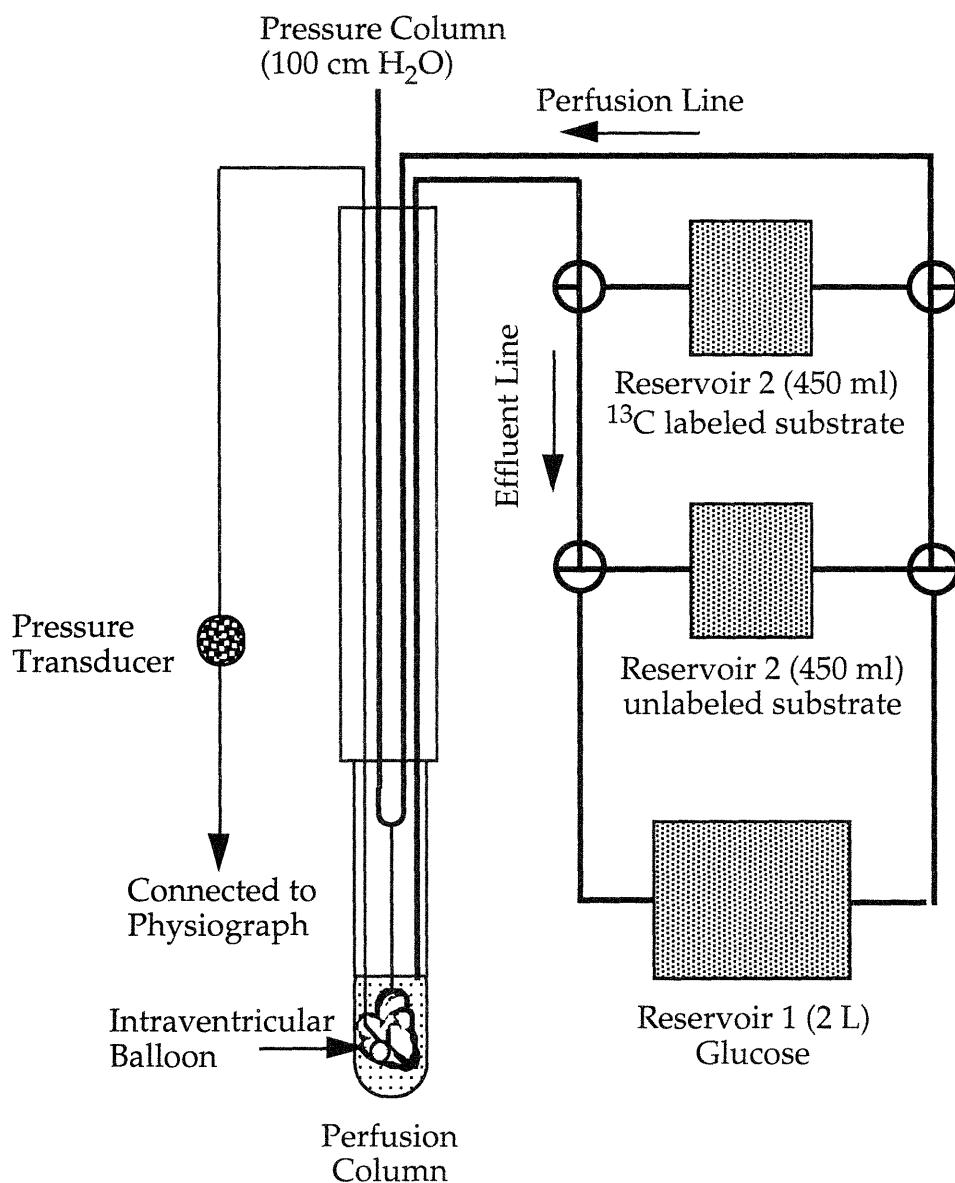
Figure 2.1 Schematic diagram of the perfusion system. The aorta is cannulated so that the perfusate flows retrogradely down the aorta and directly into the coronary arteries. A balloon placed through the left atrium into the left ventricle enables measurement of left ventricular pressure.

A schematic diagram of the perfusion system is shown in Figure 2.1. Isolated perfused hearts were placed within a sample tube in a 20 mm broadband NMR probe (Bruker Instruments). The perfusion column together with the NMR probe was situated in a vertical-bore superconducting NMR magnet operating at a field strength of 9.4-tesla (Bruker Instruments). Temperature of the hearts was continuously maintained at 37°C by warm air flow controlled at the NMR system console. A latex balloon was placed in the

left ventricle to allow the heart perform isovolumic contraction. The balloon was inflated with water to create a diastolic pressure of 5-10 mmHg and was connected to a pressure transducer line and physiograph (Gould, Inc., Cleveland, OH). Left ventricular developed pressure and heart rate were continually monitored and recorded with this intraventricular balloon. Coronary flow rate was also measured at different stages of perfusion. Oxygen content of both perfusion medium in the supply line and coronary effluent collected from the pulmonary artery was measured using a blood-gas analyzer (Instrumentation Laboratory, Lexington, MA).

2.2 Experimental Protocol

During initial preparation, hearts were perfused with buffer containing 5 mM glucose (Reservoir 1 in Figure 2.2). Exogenous substrates were added to the buffer after the heart was placed inside the magnet and the magnetic field was shimmed for optimal homogeneity. Before each protocol, a start-point ^{31}P spectrum was acquired to confirm the viability and metabolic stability of the preparation. At the beginning of each protocol, hearts were perfused with unlabeled substrate from a second reservoir for metabolic equilibrium, i.e. steady-state metabolic fluxes and constant metabolite concentrations. Although some investigators have reported that metabolite levels may stabilize in a period of 3 to 5 minutes (137), all the hearts were perfused with unlabeled substrate for 10 minutes to ensure that metabolic equilibrium was established (98). During this period, a natural abundance ^{13}C spectrum was acquired. The substrate supply was then switched to the corresponding ^{13}C labeled substrate in the third reservoir. Sequential ^{13}C spectra were then acquired with time resolution of 1 to 2.5 minute until steady-state enrichment was reached. Depending on the substrate and workload, it took approximately 30 to 70 minutes for the heart to reach isotopic steady-state enrichment. At the end of each protocol, an end-point ^{31}P spectrum was acquired for the final energetic state of the heart. After the perfusion column was taken out from the magnet, the heart was freeze clamped in liquid nitrogen and weighed. The freeze-clamped tissue was reserved for biochemical assays and high resolution ^{13}C NMR analysis. This protocol is summarized in Figure 2.2.
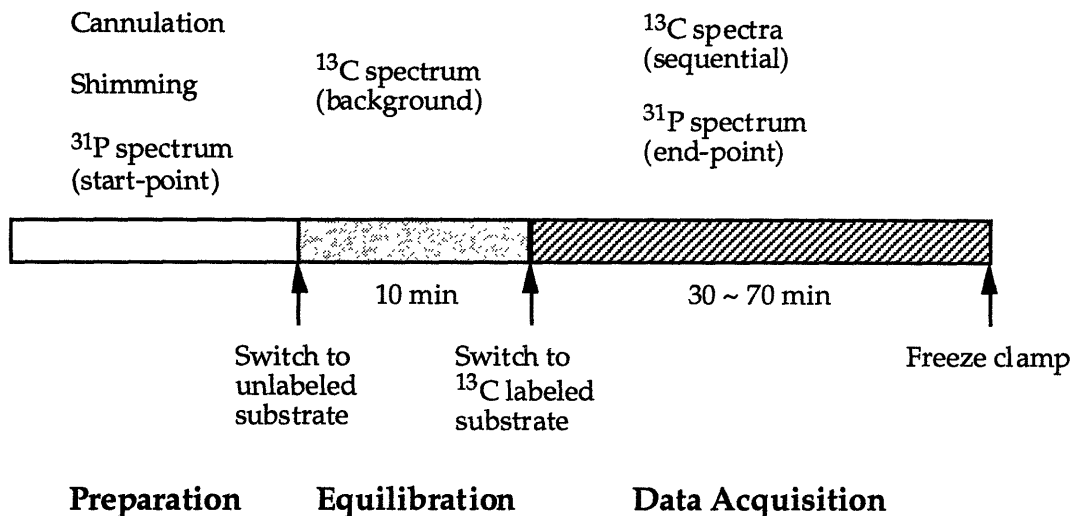
Cannulation

Shimming

^{13}C spectrum
(background)

^{13}C spectra
(sequential)

^{31}P spectrum
(start-point)

^{31}P spectrum
(end-point)

10 min   30 ~ 70 min

Switch to
unlabeled
substrate

Switch to
^{13}C labeled
substrate

Freeze clamp

Preparation   **Equilibration**   **Data Acquisition**

Figure 2.2. **Perfusion protocol.** Preparation is followed by a 10 minute period of equilibration with unlabeled substrate. At the end of data acquisition, heart was freeze clamped for *in vitro* analysis.

2.3 Tissue Biochemistry

Acid extracts were obtained from freeze-clamped ventricular muscle of hearts perfused in the magnet. Approximately 2 ml/g tissue weight of 7% perchloric acid ($HClO_4$) was added to the frozen tissue. The tissue was ground to powder in liquid nitrogen and the homogenate was defrosted at 0°C. The precipitated protein was centrifuged away. The acidic supernatant was then neutralized to pH 6.5 ~ 7.0 with KOH and recentrifuged to remove the precipitated $KClO_4$. Part of the tissue extract was reserved for biochemical analysis, the rest was lyophilized and reconstituted in 0.5 ml deuterium oxide (D_2O). High-resolution ^1H and ^{13}C spectra of reconstituted extract material were obtained.

Glutamate, α-ketoglutarate, aspartate, and citrate contents in myocardium were determined by spectrophotometric or fluorometric techniques (5, 136). The basic principles for these assays are described below, with detailed description of the assay systems included in Appendix A.

The measurements of all four metabolites have used coupled reactions in which the substance to be determined is first transformed by the auxiliary reaction, while an indicator reaction that reacts stoichiometrically with the substance to be analyzed in the auxiliary reaction is used for actual measurement. Especially in the measurement of α-ketoglutarate, aspartate,

and citrate, the reaction catalyzed by malate dehydrogenase (MDH, EC 1.1.1.37) has been used as indicator reaction in all three assays. Malate dehydrogenase catalyzes the following reaction with the equilibrium lies in favor of the oxidation of NADH (K_{eq}=36,000) (61)

$$\text{Oxaloacetate} + \text{NADH} + H^+ \xrightarrow{MDH} \text{L-Malate} + NAD^+$$
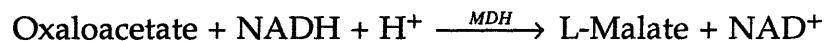
Therefore, with oxaloacetate in stoichiometric proportion to the transformed substance to be determined in the auxiliary reaction, the disappearance of NADH in the combined assay system, which can be measured either fluorometrically or spectrophotometrically, is also stoichiometrically proportional to the concentration of the substance to be determined.

2.3.1 Glutamate Assay

Glutamate level was determined with glutamate dehydrogenase (GDH, EC 1.4.1.2) and diaphorase. Glutamate dehydrogenase catalyzes the oxidative deamination of L-glutamate to α-ketoglutarate and NH_4^+.

$$\text{L-Glutamate} + NAD^+ + H_2O \xleftrightarrow{GDH} \alpha\text{-Ketoglutarate} + NH_4^+ + \text{NADH} + H^+$$
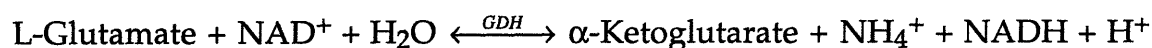
In the reaction catalyzed by diaphorase the NADH formed in the above reaction converts iodonitro tetrazolium chloride (INT) to a formazan which is measured in the visible range at 492 nm.

$$\text{NADH} + \text{INT} + H^+ \xrightarrow{diaphorase} NAD^+ + \text{Formazan}$$
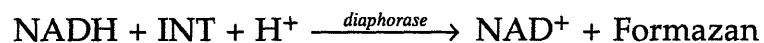
The equilibrium of glutamate dehydrogenase lies far on the side of L-glutamate. However, by trapping the NADH formed with INT, the equilibrium is displaced in favor of α-ketoglutarate

2.3.2 α-Ketoglutarate Assay

α-Ketoglutarate content was measured by coupling glutamate-oxaloacetate transaminase (GOT, EC 2.6.1.1) with malate dehydrogenase (MDH). Glutamate-oxaloacetate transaminase catalyzes the transamination of L-aspartate and α-ketoglutarate to oxaloacetate and L-glutamate.

$$\alpha\text{-Ketoglutarate} + \text{L-Aspartate} \xleftrightarrow{GOT} \text{L-Glutamate} + \text{Oxaloacetate}$$
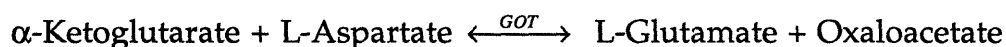
With an excess of L-aspartate, when oxaloacetate is reduced to malate with malate dehydrogenase and NADH, the disappearance of NADH in the combined assay system is stoichiometrically proportional to the concentration of α-ketoglutarate.

$$\alpha\text{-Ketoglutarate} + \text{L-Aspartate} + \text{NADH} + \text{H}^+ \xrightarrow{GOT,MDH}$$
$$\text{L-Glutamate} + \text{Malate} + \text{NAD}^+$$
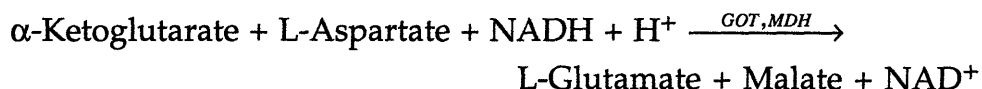
2.3.3 Aspartate Assay

Aspartate concentration was also measured by coupling glutamate-oxaloacetate transaminase with malate dehydrogenase. The assay system is similar to that described above for the α-ketoglutarate assay, with the exception that excess α-ketoglutarate is used in place of aspartate.

2.3.4 Citrate Assay

Citrate content was determined with citrate lyase (CL, EC 4.1.3.6) and malate dehydrogenase (MDH). Citrate lyase, when activated by Mg^{++}, catalyzes the cleavage of citrate to oxaloacetate and acetate with the equilibrium constant in favor of citrate synthesis.

$$\text{Citrate} \xleftarrow{CL,Mg^{++}} \text{Oxaloacetate} + \text{Acetate}$$

The reaction is coupled to malate dehydrogenase for the quantitative removal of oxaloacetate, thereby pulling the overall reaction from left to right.

$$\text{Citrate} + \text{NADH} + \text{H}^+ \xrightarrow{CL,MDH} \text{Malate} + \text{Acetate} + \text{NAD}^+$$

The accompanying decrease in fluorescence of NADH can then be followed spectrophotometrically by the change in optical density at 340 nm.

2.4 NMR Techniques

All NMR data were collected on a Bruker 400MSL NMR spectrometer interfaced to a 9.4-tesla, 89 cm vertical bore, superconducting magnet (Bruker Instruments). Signal intensity of resonance peaks was determined for all spectra by curve-fitting each resonance peak with a Lorentzian curve and integrating the area under the fitted curve with NMR-dedicated software (NMR1, Tripos Associates, Inc., St. Louis, MO).

2.4.1 NMR of Isolated Perfused Hearts

^{31}P and ^{13}C spectra were obtained from isolated hearts perfused within a broadband, 20 mm NMR probe equipped with a proton decoupling coil (Bruker Instruments). Before each experiment, the magnetic field homogeneity was optimized by shimming on proton signal from water to a linewidth of 20 to 30 Hz.

Dynamic ^{13}C spectra from intact hearts were acquired at 101 MHz with a 45° pulse angle, 2 second recycle time, and 80 ppm sweep width. Depending on the substrate, the spectra were collected with a temporal resolution of 1 to 2.5 minutes (24 to 64 free induction decays). Bilevel broadband decoupling at 0.5 W (1.8 seconds) and 7.0 W (17 μsec) was applied to eliminate carbon-proton coupling and induce Nuclear Overhauser Enhancement (NOE) without sample heating. The free induction decay was acquired with 8K data set. Changes in relative signal intensities due to Nuclear Overhauser Enhancement or relaxation effect were negligible under these pulsing conditions (69, 76). Natural abundance ^{13}C signal was digitally subtracted, and the raw signal was processed by exponential filtering with a line broadening of 20 Hz to enhance the signal-to-noise ratio before being converted into frequency domain by Fourier transformation. Peak assignments were referenced to the known resonance of the exogenous, ^{13}C enriched substrate (2-carbon of acetate at 24.1 ppm, 2-carbon of butyrate at 40.2 ppm) and the well-documented glutamate signals (4-carbon of glutamate at 34.4 ppm, 2-carbon of glutamate at 55.7 ppm, and 3-carbon of glutamate at 27.9 ppm) (1, 17).

^{31}P spectra were obtained at 161 MHz with a 45° pulse angle, 1.8 second recycle time, and 35 ppm sweep width with 64 scans. The free induction decay was acquired with 8K data set using quadrature phase detection. Raw ^{31}P signal was converted into frequency domain by Fourier transformation following the application of exponential filtering (20 Hz line broadening). The phosphocreatine (PCr) peak served as a reference at 0 ppm. Relative ATP level was assessed from the intensity of the β-phosphate peak at -16 ppm. The pH was calculated from the chemical shift of inorganic phosphate (P$_i$) with respect to PCr:

$$pH = 6.75 + \log(\frac{\sigma - 3.27}{5.69 - \sigma})$$

where σ is the chemical shift of P_i (14, 93, 108).

3.4.2 High resolution NMR of tissue extracts

High resolution ^1H and ^{13}C spectra of tissue extracts reconstituted in 0.5 ml D_2O were acquired with a 5 mm $^1H/^{13}C$ probe (Bruker Instruments). Prior to data acquisition, the magnetic field homogeneity was optimized by shimming on proton signal from the sample to a linewidth of 0.8 to 1.2 Hz.

^{13}C spectra were collected over 3000 or 6000 scans with broadband proton decoupling. The samples were maintained at 25°C through out data acquisition. Spectra were acquired using 45° excitation pulse and 1.8 second recycle time. 32K points were collected over a 200 ppm sweep width using quadrature phase detection. The free induction decay was zero filled to 64K to improve spectral resolution. The signal was then processed by 1 Hz exponential filtering followed by Fourier transformation. The multiplet structure of glutamate due to ^{13}C-^{13}C spin-spin coupling in the isotopomers was analyzed. The splitting due to the ^{13}C-^{13}C coupling is ~34 Hz between protonated carbons and ~52 Hz between protonated and carboxyl carbons of glutamate (20).

The relative concentrations of glutamate isotopomers are sensitive to the various pathways for carbon flow into the TCA cycle. Therefore, high resolution ^{13}C NMR spectra can be interpreted in quantitative physiological terms (74, 76). In the case of this study where all the ^{13}C label enters the TCA cycle through [2-^{13}C] acetyl-CoA, the analysis of glutamate resonances allowed the fraction of 2-carbon labeled acetyl-CoA entering the TCA cycle (F_c) and the ratio of anaplerotic flux to citrate synthase flux (y) to be calculated. Since all the carbons enter the cycle through anaplerotic flux are unlabeled, the equations relating F_c and y to the multiplet structures of glutamate signals can be simplified to

$$C2S = \frac{2(y+1)^2 - 2F_c(y+1) - F_c + F_c^2}{2(y+1)^2} \qquad (2.1)$$

$$C2D12 = \frac{F_{c0}F_c}{2(y+1)^2} \qquad (2.2)$$

$$C2D23 = \frac{F_c(2+2y-F_c)}{2(y+1)^2} \qquad (2.3)$$

$$C3S = \frac{F_{c0}(F_{c0} + y)}{y+1} \qquad (2.4)$$

$$C3T = \frac{F_c^2}{y+1} \qquad (2.5)$$

$$C4D34 = \frac{F_c}{2y+1} \qquad (2.6)$$

where

$F_{c0} = 1 - F_c$ = Fraction of unlabeled acetyl-CoA entering the TCA cycle;

$C2S$ = Area of singlet/C-2 resonance area;

$C2D12$ = Area of doublet due to C-1 coupling/C-2 resonance area;

$C2D23$ = Area of doublet due to C-3 coupling/C-2 resonance area;

$C3S$ = Area of singlet/C-3 resonance area;

$C3T$ = Area of triplet/C-3 resonance area;

$C4D34$ = Area of doublet due to C-3 coupling/C-4 resonance area.

The left sides of Equations (2.1) - (2.6) were obtained from *in vitro* ^{13}C NMR spectrum by peak integration. F_c and y were determined for each experiment by least-square fitting of the right sides of Equations (2.1) - (2.6) to the left sides. The fitting was performed using MATLAB (The MathWorks Inc., Natick, MA). The MATLAB program for the evaluation of F_c and y is included in Appendix B.

The amount of glutamate labeled at 4-carbon position was determined by referencing the signal intensity from glutamate C4 resonance peak in each ^{13}C spectra to the 2 mM glucose C1-α signal (24). Total ^{13}C labeled glutamate at 4-carbon position was then divided by total tissue concentration of glutamate from enzymatic assay to obtain the fractional enrichment of glutamate at the 4-carbon position.

For hearts perfused with [3-^{13}C] lactate, water suppressed ^{1}H spectra were also obtained to quantify the fraction of ^{13}C enriched alanine. The spectra were acquired using a 1331 pulse sequence (41, 42) with τ=390 μsec so that the maximum signal was centered between the resonances of methyl protons of alanine (1.48 ppm) and lactate (1.33 ppm). 96 free induction decays were acquired in 32K data set with 4.1 seconds recycle time and 10 ppm sweep width.

For both alanine and lactate, the protons bound to an unlabeled methyl carbon appear as a 7 Hz doublet due to the proton-proton coupling of the methyl proton to the vicinal proton. Those bound to a ^{13}C are split into two pairs of peaks that resonate on either side of the central doublet, with a J coupling constant of 128 Hz (63). Therefore, the fraction of ^{13}C labeled alanine can be calculated as the ratio of the area of the two side peaks to the combined area of the central and side peaks (24).

2.5 Statistical Analysis

All data are presented as mean ± standard deviation (Mean±SD). Comparison of intragroup data sets was performed with the Student's paired, two-tailed t test. Differences in mean values were considered statistically significant at a probability level of less that 5% ($p<0.05$).

Chapter 3

Kinetic Analysis of
Dynamic ^{13}C NMR Spectra

This chapter introduces the kinetic modeling technique developed for the analysis of dynamic ^{13}C enrichment of glutamate. A brief review of the existing methods in dynamic ^{13}C NMR spectroscopy will be followed by a detailed description of the model, which is distinct from other previous studies. The optimization technique used in kinetic analysis is also discussed. Practical considerations are addressed at the end of this chapter.

3.1   Current Analytical Techniques of Dynamic ^{13}C NMR Spectra

^{13}C NMR spectra, whether obtained sequentially from the intact heart or from tissue extracts, contain various sorts of information that require mathematical treatment for a comprehensive evaluation. Several previous studies have employed modeling schemes to explore TCA cycle flux and its regulation (17, 19, 34, 81, 82, 101, 131). These methods are based largely on previously described patterns of ^{14}C incorporation in metabolites which were determined by traditional, destructive biochemical methods (47, 49, 91, 98, 121, 129). An important early work, made by Chance *et al.*, applied a kinetic model to the analysis of ^{13}C labeling within glutamate as detected in *in vitro* spectra of tissue extracts at different time points (17). The modeling of ^{13}C kinetic data from rat heart perfused with [2-^{13}C] acetate and [3-^{13}C] pyruvate lead to the estimates of the TCA cycle flux and the aspartate and alanine aminotransferase reaction rates. The model, however, requires the simultaneous solution of nearly 200 differential equations and is cumbersome to use since it uses a single compartment to represent each individual ^{13}C isotopomer. In addition, the results generated by that model were not rigorously compared with other measures of TCA cycle flux over a range of values, such as might be induced by varied physiological contractile conditions. This model was recently expanded to include both glycolysis and malate-aspartate shuttle, leading to an even more complicated model with 340 differential equations (19).

Recognizing the limitations of such complicated model with large numbers of equations to solve, Lewandowski used an empirical time constant of glutamate 2-carbon/4-carbon (C2/C4) curve as an index of the TCA cycle flux and demonstrated that under widely varying workloads, the myocardium displayed unchanging fractional enrichments and glutamate pool sizes, and yet very different time constant for C2/C4 curves (66).

Similarly, Weiss *et al.* have used an empirical flux parameter K_T as and index of the TCA cycle flux (131). K_T is defined as

$$K_T = \frac{\sum {}^{13}C \text{ NMR - detected TCA metabolites } (\mu moles \, / \, g)}{F_c \times \text{glutamate } \Delta t_{50} \text{ (min)}}$$

where glutamate Δt_{50} is the time difference for the glutamate 4- and 2-carbons to reach half of their steady-state enrichment levels. And the ${}^{13}C$ NMR-detected TCA metabolites include glutamate, aspartate, and citrate. Such an approach is based on the assumption that the TCA cycle flux is inversely proportional to the time difference between ${}^{13}C$ appearance in the 4- and 2-carbon positions of glutamate (glutamate Δt_{50}). However, this hypothesis needs to be further validated with various substrates that can potentially perturb the TCA cycle without significant changes in oxygen consumption and workload. Furthermore, although K_T has the unit of flux parameter, it is not necessarily equal to the TCA cycle flux.

Robitaille *et al.* have proposed post-steady state analysis as an complementary method to the pre-steady state method (101). The advantages of using post-steady state analysis is that a closed form solution of the rate of label washout from the 4-carbon of glutamate can be obtained. However, the model is based on the assumption that the flux through α-ketoglutarate dehydrogenase is much slower than the interconversion rate between α-ketoglutarate and glutamate. This assumption yet needs to be further tested.

Mason *et al.* have developed a kinetic model for the analysis of glucose metabolism in cerebral energy production (81, 82). ${}^1H$-observed/${}^{13}C$-edited NMR spectroscopy technique was used in data acquisition to improve the sensitivity of NMR measurements in brain *in vivo* (102, 103). However, by using a 3-step procedure in data fitting, the use of V_{gt}, i.e. the rate of isotopic flow into glutamate, made the intrinsic assumption without further

validation that the exchange rate between α-ketoglutarate and glutamate was fast.

The effort of developing new analytical techniques in this work was not to improve any of the current existing models, but rather to identify potential rate-limiting factors in ^{13}C labeling of glutamate. As ^{13}C spectra contain various sorts of information, a comprehensive evaluation requires mathematical treatment. Therefore, a significant portion of this work comprised of the development of kinetic analysis method for the evaluation of dynamic ^{13}C NMR spectra. This method is presented in this chapter.

3.2 Compartment Model of the TCA Cycle

To establish the compartment model for kinetic analysis of the TCA cycle, it is necessary to first examine the mechanism by which ^{13}C label is incorporated into the intermediary metabolite pools and detected by ^{13}C NMR (Figure 3.1).

Over the course of perfusion with ^{13}C-enriched substrate, incorporation of label into the glutamate pool was detected by ^{13}C NMR. The appearance of resonance peaks that correspond to ^{13}C enrichment at specific carbon positions within the glutamate pool have been described in detail by others (17, 45, 76). Detection of ^{13}C NMR signal from glutamate is based on the relatively high concentration of intracellular glutamate that is in constant exchange with the TCA cycle intermediates via transamination reaction with α-ketoglutarate. Initial incorporation of label into the glutamate pool, from the condensation of unlabeled oxaloacetate with [2-^{13}C] acetyl-CoA, occurs at the 4-carbon position. The recycling of label through the TCA cycle places ^{13}C at either the 2- or 3-carbon of glutamate. The labeling at the 2- and 3-carbon of glutamate is of equal probability due to the symmetry of succinate molecule. This labeling scheme is shown in Figure 3.1. Although some investigators have reported asymmetric labeling of malate in various mammalian tissues perfused with ^{13}C labeled propionate (113), this phenomenon has not been observed in NMR experiments involving functioning tissues oxidizing substrates that enter the TCA cycle via acetyl-CoA (66, 131).
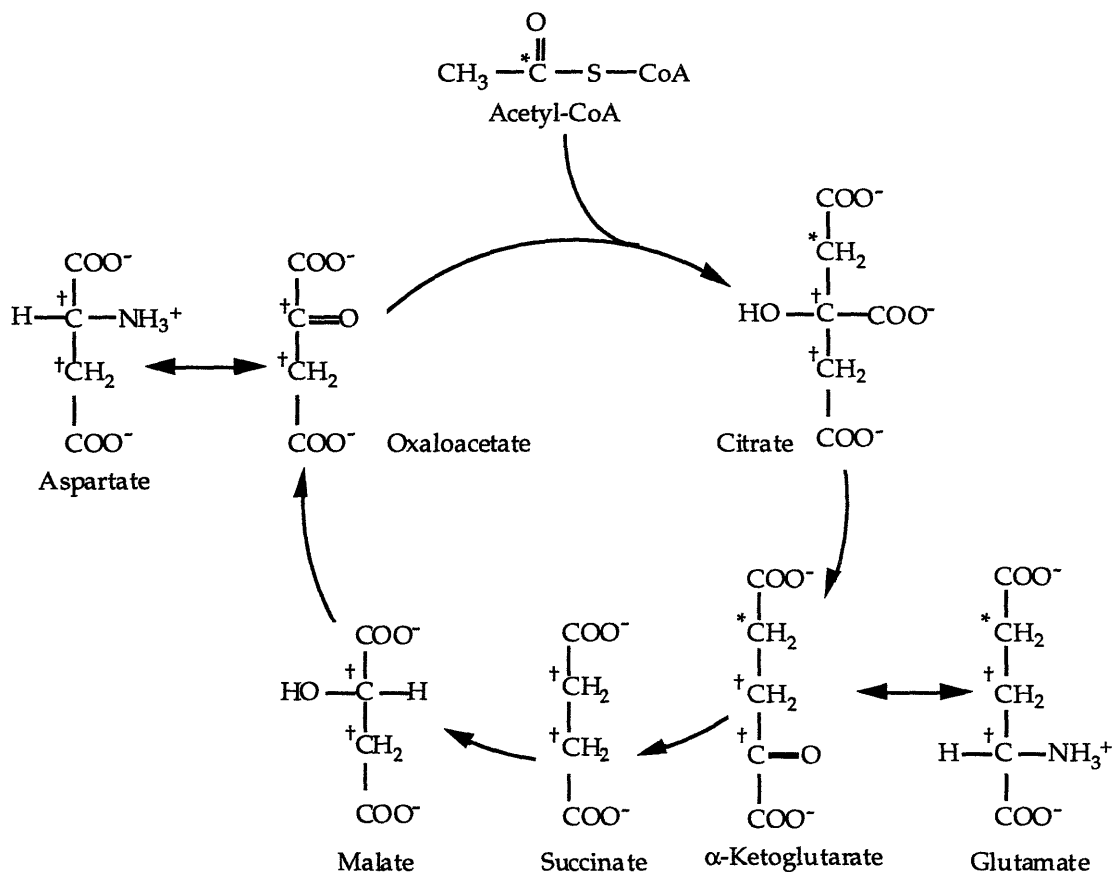
O
‖
CH₃ —*C —S —CoA
Acetyl-CoA

Figure 3.1 Labeling scheme employed in dynamic ^{13}C NMR spectroscopy. Exogenous substrate enters the TCA cycle via [2-^{13}C] acetyl-CoA. Initial sites of ^{13}C labeling (*) are at the 4-carbon position of citrate, α-ketoglutarate, and glutamate. Recycling of ^{13}C within the TCA cycle results in the labeling of 2- and 3-carbons (†) with equal probability.

The kinetic model for the presteady-state isotope turnover within key metabolite pools is derived from the simplified metabolic compartment model that includes major rate-limiting tricarboxylate pools such as citrate, α-ketoglutarate, malate, and oxaloacetate, as well as the major contributing amino acid pools, i.e. glutamate and aspartate (Figure 3.2). This simplification was justified by comparing the simulated results with that of a more comprehensive model that also includes succinate and fumarate pool (139). The model will be used to address ^{13}C labeling within key metabolite pools. Specifically, the presteady-state incorporation of ^{13}C at 4- and 2-carbon positions of glutamate and the fractional enrichment of ^{13}C within several key metabolite pools will be analyzed using the model. Analysis is carried out at steady state metabolic flux and with constant intermediate pool sizes. Because of the symmetry in 2- and 3-carbon labeling, the model only

considers the labeling of 2-carbon while regarding the labeling of 3-carbon as the same to that of 2-carbon. Citrate, α-ketoglutarate, and glutamate pools are further divided into 2 subcompartments to represent ^{13}C labeling at the 2- and 4-carbon positions of each intermediate.
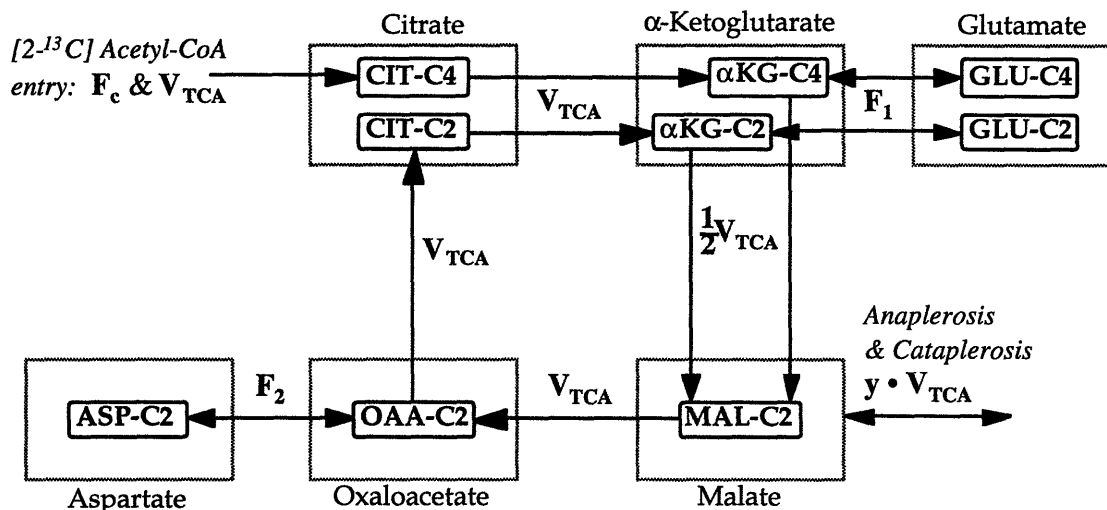

Figure 3.2 Compartment model of the TCA cycle. Large boxes represent metabolite pools of or related to the TCA cycle. Small boxes represent real mathematical compartments of the model. Labeling of 3-carbon is the same as 2-carbon and is therefore omitted. Mixing of label occurs after the α-ketoglutarate compartment. Anaplerosis and cataplerosis occur at malate pool. Metabolite pools are, CIT: citrate; αKG: α-ketoglutarate; GLU: glutamate; MAL: malate; OAA: oxaloacetate; ASP: aspartate. Flux parameters are, V_{TCA}: TCA cycle flux; F_1: interconversion rate between α-ketoglutarate and glutamate; F_2: interconversion rate between aspartate and oxaloacetate. C4 and C2 refer to the 4- and 2- carbon positions.

Effects of substrate utilization and anaplerosis are also accounted for by incorporating data measured from high resolution ^{13}C NMR as parameters in the model. Incorporation of unlabeled intermediate through anaplerosis was considered to enter the TCA cycle at malate while efflux of carbon mass (cataplerosis) occurred through malic enzyme (52, 95, 104).

3.3 Mathematical Description of the Model

Analysis of metabolic activity was based on the observations of presteady state ^{13}C NMR spectra of glutamate reflecting the dynamic labeling pattern described above. Kinetic equations describing presteady state labeling of ^{13}C within key metabolic compartments will be presented in detail in this section.

Let the steady state TCA cycle flux be V_{TCA}, the interconversion rate between α-ketoglutarate and glutamate, oxaloacetate and aspartate be F_1 and

F_2 respectively. By the principle of mass conservation, the time rate of change in ^{13}C label in a compartment equals the difference of the amount of ^{13}C label entering the compartment and the amount of ^{13}C label leaving the same compartment. While the amount of ^{13}C label leaving the compartment is the total flux leaving that compartment multiplied by the enrichment level of that compartment, the amount of ^{13}C label entering the compartment is the flux entering that compartment multiplied by the enrichment level from the upstream compartment. Therefore, the concentration history of the metabolites can be characterized by a group of differential equations incorporating both the TCA cycle flux and the interconversion rates between metabolite pools.

- Citrate pool

$$\frac{d}{dt}[CIT - C4] = V_{TCA} \cdot F_c - V_{TCA} \cdot \frac{[CIT - C4]}{[CIT]} \tag{3.1}$$

$$\frac{d}{dt}[CIT - C2] = V_{TCA} \cdot \frac{[OAA - C2]}{[OAA]} - V_{TCA} \cdot \frac{[CIT - C2]}{[CIT]} \tag{3.2}$$

- α-Ketoglutarate pool

$$\frac{d}{dt}[\alpha KG - C4] = V_{TCA} \cdot \frac{[CIT - C4]}{[CIT]} - (V_{TCA} + F_1) \cdot \frac{[\alpha KG - C4]}{[\alpha KG]} + F_1 \cdot \frac{[GLU - C4]}{[GLU]} \tag{3.3}$$

$$\frac{d}{dt}[\alpha KG - C2] = V_{TCA} \cdot \frac{[CIT - C2]}{[CIT]} - (V_{TCA} + F_1) \cdot \frac{[\alpha KG - C2]}{[\alpha KG]} + F_1 \cdot \frac{[GLU - C2]}{[GLU]} \tag{3.4}$$

- Glutamate pool

$$\frac{d}{dt}[GLU - C4] = F_1 \cdot \frac{[\alpha KG - C4]}{[\alpha KG]} - F_1 \cdot \frac{[GLU - C4]}{[GLU]} \tag{3.5}$$

$$\frac{d}{dt}[GLU - C2] = F_1 \cdot \frac{[\alpha KG - C2]}{[\alpha KG]} - F_1 \cdot \frac{[GLU - C2]}{[GLU]} \tag{3.6}$$

- Malate pool

$$\frac{d}{dt}[MAL - C2] = \frac{1}{2} V_{TCA} \cdot (\frac{[\alpha KG - C4]}{[\alpha KG]} + \frac{[\alpha KG - C2]}{[\alpha KG]}) - (1 + y) \cdot V_{TCA} \cdot \frac{[MAL - C2]}{[MAL]} \tag{3.7}$$

The 1/2 introduced in this equation takes into account that there is an equal mixing of the label at the 2- and 3-carbons of malate. The y term

represents unlabeled intermediate entering the TCA cycle through anaplerotic flux while labeled TCA cycle intermediate leaves the cycle through cataplerotic flux. The anaplerotic flux and cataplerotic flux are equal in order to maintain constant TCA cycle intermediate pool sizes.

- Oxaloacetate pool

$$\frac{d}{dt}[OAA - C2] = V_{TCA} \cdot \frac{[MAL - C2]}{[MAL]} - (V_{TCA} + F_2) \cdot \frac{[OAA - C2]}{[OAA]} + F_2 \cdot \frac{[ASP - C2]}{[ASP]} \qquad (3.8)$$

- Aspartate pool

$$\frac{d}{dt}[ASP - C2] = F_2 \cdot \frac{[OAA - C2]}{[OAA]} - F_2 \cdot \frac{[ASP - C2]}{[ASP]} \qquad (3.9)$$

Since the total concentration of citrate, i.e. $[CIT]$, is a constant, we can rewrite Equation (3.1) as

$$[CIT] \cdot \frac{d}{dt} \frac{[CIT - C4]}{[CIT]} = V_{TCA} \cdot F_c - V_{TCA} \cdot \frac{[CIT - C4]}{[CIT]}$$

Define the dimensionless quantity $CIT4$ as the fraction of citrate that is ^{13}C labeled at the 4-carbon position, i.e.

$$CIT4 = \frac{[CIT - C4]}{[CIT]}$$

Therefore, Equation (3.1) can be written as

$$\frac{d}{dt} CIT4 = \frac{V_{TCA}}{[CIT]} \cdot (F_c - CIT4)$$

In the same way, we can also define the fractional enrichment variables for other compartment and rewrite the equations in terms of the corresponding fractional enrichment levels. Therefore, the pre-steady state labeling of ^{13}C for each compartment can be described by the following equations

$$\frac{d}{dt} CIT4 = \frac{V_{TCA}}{[CIT]} \cdot (F_c - CIT4) \qquad (3.10)$$

$$\frac{d}{dt} \alpha KG4 = \frac{V_{TCA}}{[\alpha KG]} \cdot CIT4 - \frac{V_{TCA} + F_1}{[\alpha KG]} \cdot \alpha KG4 + \frac{F_1}{[\alpha KG]} \cdot GLU4 \qquad (3.11)$$

$$\frac{d}{dt}GLU4 = \frac{F_1}{[GLU]} \cdot (\alpha KG4 - GLU4) \tag{3.12}$$

$$\frac{d}{dt}CIT2 = \frac{V_{TCA}}{[CIT]} \cdot (OAA2 - CIT2) \tag{3.13}$$

$$\frac{d}{dt}\alpha KG2 = \frac{V_{TCA}}{[\alpha KG]} \cdot CIT2 - \frac{V_{TCA} + F_1}{[\alpha KG]} \cdot \alpha KG2 + \frac{F_1}{[\alpha KG]} \cdot GLU2 \tag{3.14}$$

$$\frac{d}{dt}GLU2 = \frac{F_1}{[GLU]} \cdot (\alpha KG2 - GLU2) \tag{3.15}$$

$$\frac{d}{dt}MAL2 = \frac{V_{TCA}}{[MAL]} \cdot [\frac{1}{2} \cdot \alpha KG2 + \frac{1}{2} \cdot \alpha KG4 - (1+y) \cdot MAL2] \tag{3.16}$$

$$\frac{d}{dt}OAA2 = \frac{V_{TCA}}{[OAA]} \cdot MAL2 - \frac{V_{TCA} + F_2}{[OAA]} \cdot OAA2 + \frac{F_2}{[OAA]} \cdot ASP2 \tag{3.17}$$

$$\frac{d}{dt}ASP2 = \frac{F_2}{[ASP]} \cdot (OAA2 - ASP2) \tag{3.18}$$

Therefore, we have nine linear differential equations (Equations 3.10-3.18) to describe the pre-steady state labeling of ^{13}C at the 4- and 2-carbon positions of each metabolite pool in the TCA cycle. These equations characterize the TCA cycle kinetics by three flux parameters (i.e. V_{TCA}, F_1, and F_2), fraction of ^{13}C acetyl-CoA labeled at 2-carbon (F_c), relative anaplerotic flux (y), and the corresponding metabolite concentrations. If we use a single 9×1 vector $\mathbf{q}$ to represent the fractional enrichment of each compartment as a function of time, i.e.

$$\mathbf{q} = \begin{bmatrix} CIT4 \\ \alpha KG4 \\ GLU4 \\ CIT2 \\ \alpha KG2 \\ GLU2 \\ MAL2 \\ OAA2 \\ ASP2 \end{bmatrix} = \begin{bmatrix} [CIT-C4]/[CIT] \\ [\alpha KG-C4]/[\alpha KG] \\ [GLU-C4]/[GLU] \\ [CIT-C2]/[CIT] \\ [\alpha KG-C2]/[\alpha KG] \\ [GLU-C2]/[GLU] \\ [MAL-C2]/[MAL] \\ [OAA-C2]/[OAA] \\ [ASP-C2]/[ASP] \end{bmatrix}$$

The model can then be described in matrix form as

$$\frac{d}{dt}\mathbf{q} = \mathbf{M}_{TCA} \cdot \mathbf{q} + \mathbf{U}_{Acetyl-CoA} \qquad (3.19)$$

where $\mathbf{M}_{TCA}$ is a 9×9 matrix characteristic of the TCA cycle, its elements are dependent on the TCA cycle flux (V_{TCA}), the interconversion rates between the TCA cycle intermediates and glutamate or aspartate (F_1 and F_2), the level of anaplerosis (y), and the total concentrations of each metabolite. The input vector, $\mathbf{U}_{Acetyl-CoA}$, is governed by the fraction of ^{13}C enriched acetyl-CoA entering the TCA cycle through citrate synthase (F_c). The only non-zero element in $\mathbf{U}_{Acetyl-CoA}$ is the one corresponding to the labeling of the 4-carbon position of citrate since all ^{13}C label of acetyl-CoA at 2-carbon enters the TCA cycle through citrate synthase and results in labeling at the 4-carbon position of citrate. Therefore, the evolution of $\mathbf{q}$ upon switching to the ^{13}C labeled substrate can be viewed as a linear system in response to a stepwise stimulation.

3.4 Methods of Kinetic Analysis

Upon switching to the ^{13}C labeled substrate, the initial fractional enrichment levels of all metabolite pools are 1.1% since the natural abundance of ^{13}C is 1.1%. The fractional enrichment of glutamate at 4- and 2-carbon positions over time course can be obtained from *in vivo* NMR spectroscopy, corresponding to the detectable signals in the $\mathbf{q}$ vector. By combining the mathematical analysis with NMR observation of the isotope concentration history of glutamate pool, TCA cycle flux (V_{TCA}) and interconversion rates between TCA cycle intermediates and amino acid pools (F_1 and F_2) can be determined by least-square fitting of the kinetic model to ^{13}C enrichment data from NMR spectra. The basic optimization techniques employed in this project are introduced in this section. Further details can be found in references (15, 31).

Most algorithms for nonlinear least-square estimation used either of two approaches. On the one hand, the model may be expanded as a Taylor series in Gauss-Newton method and corrections to the parameters are calculated at each iteration on the assumption of local linearity. However, because of the divergence of successive iterates, this method can have serious convergence problems with ill-conditioned functions. On the other hand, various modifications of the steepest descent method have been used, yet these

methods usually have agonizingly slow convergence after the first few iterations (27). The Levenberg-Marquardt method uses a search direction which is a cross between the Gauss-Newton direction and the steepest descent and is therefore a stable and reliable method (64, 78). In this study, we have employed the Levenberg-Marquardt method in data fitting.

Let us first rewrite the problem in more standard form. The mathematical model that describes the labeling kinetics of each individual compartment can be written as

$$\frac{d}{dt}\mathbf{q}(t,\mathbf{p}) = \mathbf{M}_{\text{TCA}}(\mathbf{p}) \cdot \mathbf{q}(t,\mathbf{p}) + \mathbf{U}_{\text{Acetyl-CoA}}(\mathbf{p}) \qquad (3.20)$$

where $\mathbf{p} = \begin{bmatrix} V_{TCA} & F_1 & F_2 \end{bmatrix}$ is the parameter vector to be determined in least-square optimization. Therefore, $\mathbf{q}(t,\mathbf{p})$ clearly indicates that the enrichment kinetics is a function of both time and flux parameters. The output, $s(t,\mathbf{p})$, of this linear system, or the NMR detectable glutamate enrichment at 4- and 2-carbons, is therefore also a function of time and flux parameters. It can be expressed as

$$\begin{aligned}
\mathbf{s}(t,\mathbf{p}) &= \begin{bmatrix} GLU4(t) \\ GLU2(t) \end{bmatrix} \\
&= \begin{bmatrix} 0 & 0 & 1 & 0 & 0 & 0 & 0 & 0 & 0 \\ 0 & 0 & 0 & 0 & 0 & 1 & 0 & 0 & 0 \end{bmatrix} \cdot \mathbf{q}(t,\mathbf{p}) \\
&= \mathbf{C} \cdot \mathbf{q}(t,\mathbf{p})
\end{aligned}$$

Let $\mathbf{d}(t,\mathbf{p})$ be the actual NMR measurement of glutamate enrichment over time. The cost function to be optimized is then of the form

$$f(\mathbf{p}) = \mathbf{e}^T \mathbf{W} \mathbf{e}$$

with $\mathbf{e} = \mathbf{d}(t,\mathbf{p}) - \mathbf{s}(t,\mathbf{p})$ be the error between experimental measurement and fitted data. $\mathbf{W}$ here is a symmetric weighting matrix. In this particular problem, we have taken the inverse of the standard deviation of each data point as the weighting matrix. Define the Hessian matrix $\mathbf{H}(\mathbf{p}) \equiv \nabla^2 f(\mathbf{p})$, which is the symmetric matrix of second derivatives of $f(\mathbf{p})$, we can now make a quadratic approximation of $f(\mathbf{p})$ at a certain search point $\mathbf{p}^k$

$$f(\mathbf{p}) \approx f(\mathbf{p}^k) + \nabla^T f(\mathbf{p}^k)\Delta\mathbf{p}^k + \tfrac{1}{2}(\Delta\mathbf{p}^k)^T \mathbf{H}(\mathbf{p}^k)\Delta\mathbf{p}^k$$

where $\Delta \mathbf{p}^k = \mathbf{p} - \mathbf{p}^k$. The minimum of f($\mathbf{p}$) in the direction of $\mathbf{p}^k$ is obtained by differentiating the quadratic approximation of f($\mathbf{p}$) with respect to each of the components of $\mathbf{p}$ and equating the resulting expressions to zero to give

$$\nabla f(\mathbf{p}) \approx \nabla f(\mathbf{p}^k) + \mathbf{H}(\mathbf{p}^k)\Delta \mathbf{p}^k = 0$$

Hence, the next search point $\mathbf{p}^{k+1}$ is

$$\mathbf{p}^{k+1} - \mathbf{p}^k = \Delta \mathbf{p}^k = -[\mathbf{H}(\mathbf{p}^k)]^{-1} \cdot \nabla f(\mathbf{p}^k)$$

$\mathbf{p}^{k+1}$ can also be evaluated without performing a matrix inversion, but instead by solving the following set of linear equations for $\Delta \mathbf{p}^k$,

$$\mathbf{H}(\mathbf{p}^k)\Delta \mathbf{p}^k = -\nabla f(\mathbf{p}^k)$$

a procedure that often leads to less round-off error than calculating $\mathbf{p}^{k+1}$ via an inversion of a matrix.

This method is called Gauss-Newton's method. It makes use of the second-order approximation of f($\mathbf{p}$) at $\mathbf{p}^k$. Thus, it is possible to take into account the curvature of f($\mathbf{p}$) at $\mathbf{p}^k$ and identify better search directions. It is therefore the fastest method of minimization when it succeeds. But one big disadvantage of Gauss-Newton's method is that it may proceed to a saddle point if $\mathbf{H}(\mathbf{p})$ is not positive definite. To overcome this problem, Levenberg (64) and Marquardt (78) have suggested that the Hessian matrix of f($\mathbf{p}$) be modified on each stage of search as needed to ensure that the modified Hessian matrix, $\tilde{\mathbf{H}}(\mathbf{p})$, is positive definite and well-conditioned. The procedure adds elements to the diagonal elements of $\mathbf{H}(\mathbf{p})$

$$\tilde{\mathbf{H}}(\mathbf{p}) = \mathbf{H}(\mathbf{p}) + \lambda \mathbf{I}$$

where λ is a positive constant large enough to make $\tilde{\mathbf{H}}(\mathbf{p})$ positive definite when $\mathbf{H}(\mathbf{p})$ is not. Therefore, the next search point is evaluated by solving linear equations

$$[\mathbf{H}(\mathbf{p}^k) + \lambda^k \mathbf{I}]\Delta \mathbf{p}^k = -\nabla f(\mathbf{p}^k)$$

where the scalar λ^k controls both the direction and step length of the search for the minimum. When λ^k is zero, the direction is identical to that of Gauss-Newton's method. As λ^k tends to infinity, the search tends towards a steepest

descent direction. The Levenberg-Marquardt method therefore uses a search direction which is a interpolator between the Gauss-Newton direction and the steepest descent, favoring steepest descent when far from convergence and the Taylor series solution near the minimum of $f(\mathbf{p})$.

The implementation of the Levenberg-Marquardt method needs the evaluations of partial derivatives with respect to the parameters to be optimized. In a nonlinear system with coupled differential equations, this can only be done iteratively. From Equation (3.20) we have

$$\frac{\partial}{\partial \mathbf{p}}(\frac{d}{dt}\mathbf{q}(t,\mathbf{p})) = \mathbf{M}_{TCA}(\mathbf{p}) \cdot \frac{\partial \mathbf{q}(t,\mathbf{p})}{\partial \mathbf{p}} + \frac{\partial \mathbf{M}_{TCA}(\mathbf{p})}{\partial \mathbf{p}} \cdot \mathbf{q}(t,\mathbf{p}) + \frac{\partial \mathbf{U}_{Acetyl-CoA}(\mathbf{p})}{\partial \mathbf{p}}$$

or

$$\frac{d}{dt}\frac{\partial \mathbf{q}(t,\mathbf{p})}{\partial \mathbf{p}} = \mathbf{M}_{TCA}(\mathbf{p}) \cdot \frac{\partial \mathbf{q}(t,\mathbf{p})}{\partial \mathbf{p}} + \frac{\partial \mathbf{M}_{TCA}(\mathbf{p})}{\partial \mathbf{p}} \cdot \mathbf{q}(t,\mathbf{p}) + \frac{\partial \mathbf{U}_{Acetyl-CoA}(\mathbf{p})}{\partial \mathbf{p}} \qquad (3.21)$$

At the first iteration, for the initial set of parameter estimates $\mathbf{p}^0$, Equations (3.20) and (3.21) can be solved in series,

$$\frac{d}{dt}\begin{bmatrix} \mathbf{q}(t,\mathbf{p}) \\ \dfrac{\partial \mathbf{q}(t,\mathbf{p})}{\partial \mathbf{p}} \end{bmatrix} = \begin{bmatrix} \mathbf{M}_{TCA}(\mathbf{p}) & 0 \\ \dfrac{\partial \mathbf{M}_{TCA}(\mathbf{p})}{\partial \mathbf{p}} & \mathbf{M}_{TCA}(\mathbf{p}) \end{bmatrix} \cdot \begin{bmatrix} \mathbf{q}(t,\mathbf{p}) \\ \dfrac{\partial \mathbf{q}(t,\mathbf{p})}{\partial \mathbf{p}} \end{bmatrix} + \begin{bmatrix} \mathbf{U}_{Acetyl-CoA}(\mathbf{p}) \\ \dfrac{\partial \mathbf{U}_{Acetyl-CoA}(\mathbf{p})}{\partial \mathbf{p}} \end{bmatrix}$$

Thus giving $\mathbf{q}(t,\mathbf{p})$ and $\dfrac{\partial \mathbf{q}(t,\mathbf{p})}{\partial \mathbf{p}}$, this then allows the new estimates $\mathbf{p}^1$ to be computed. This procedure is repeated at each incremental estimation of the parameter vector until the best fit is achieved.

3.5 Experimental Constraints for Data Fitting

Since maximal ATP generation by glycolysis is only 5-10% of the total ATP production in aerobic hearts, the rate of myocardial oxygen consumption is proportional to flux in the citric acid cycle (135). TCA cycle flux can, therefore, be calculated from the rate of oxygen consumption (MVO$_2$) with the knowledge of the substrate that is fueling respiration (51, 98, 137). Taking acetate and butyrate, which were used in this study, as an example, for the oxidation of 1 mole of acetate, 3 moles of NADH and 1 mole of FADH$_2$ are generated in the TCA cycle, which results in the consumption of 2 moles of

oxygen in electron transport chain. Hence, the turnover of the TCA cycle is one half of the oxygen consumption rate. In the case of butyrate oxidation, since additional NADH and $FADH_2$ are generated in β-oxidation, the ratio of TCA flux to MVO_2 is 1:2.5 (Figure 3.3). Therefore, oxygen consumption provided experimental constraints of the TCA cycle flux for optimization in kinetic analysis. While the optimal value for TCA cycle flux was obtained from least-square fitting of the model to dynamic ^{13}C NMR observation, an additional penalty term that reflects the difference between fitted TCA cycle flux and the TCA cycle flux calculated from oxygen consumption was added to the cost function,

$$f(\mathbf{p}) = \mathbf{e}^T \mathbf{W} \mathbf{e} + \left(\frac{V_{TCA} - V_{MVO_2}}{\sigma_{MVO_2}} \right)^2$$

where V_{MVO_2} is the TCA cycle flux estimated from the oxygen consumption rate, and σ_{MVO_2} is the error associated with the measurement of oxygen consumption. This allowed the computer to search in a range of estimated TCA cycle flux from oxygen consumption while taking into consideration the measurement error and the oxidation of other fuels.
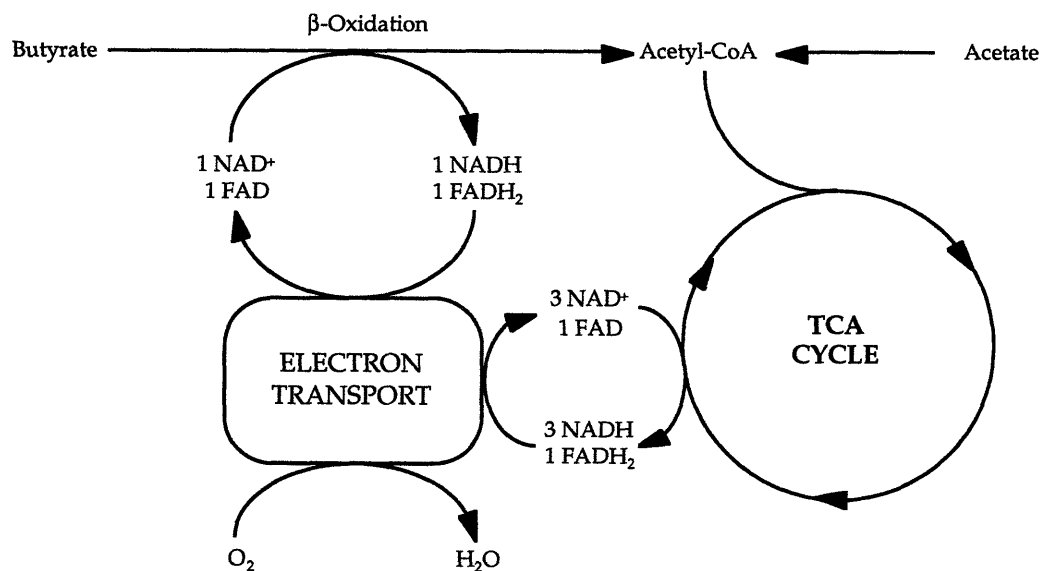
Figure 3.3 Metabolic diagram of acetate and butyrate oxidation. Acetate has direct entry into the TCA cycle via acetyl-CoA. Butyrate, as a four-carbon molecule, undergoes β-oxidation to be cleaved into two acetyl-CoA molecules before entering the TCA cycle. β-Oxidation generates additional reducing equivalents that require oxygen to be reoxidized. Therefore, at the same oxygen consumption rate, TCA cycle flux from butyrate oxidation is slower comparing to acetate oxidation, yet the energy yield is the same.

To minimize the number of unknowns in data fitting, acetyl-CoA enrichment (F_c), and relative anaplerotic flux (y) were determined from high-resolution NMR spectrum of tissue extracts. Glutamate, aspartate, citrate, and α-ketoglutarate concentrations were measured by enzymatic assays. Other metabolite concentrations whose values are less critical to the enrichment kinetics of glutamate were taken from literature on heart perfused under similar substrate conditions: malate, 0.60 μmoles/g dry weight; oxaloacetate, 0.04 (98, 123). TCA cycle flux (V_{TCA}) and interconversion rates between TCA cycle intermediates and amino acid pools (F_1 and F_2) were determined by nonlinear least-square fitting of the model to ^{13}C enrichment data from NMR spectra using the Levenberg-Marquardt method, with the goodness of the fit evaluated by the correlation coefficient (6).

Two transamination reactions are involved in the exchange of ^{13}C label between the TCA cycle intermediates and glutamate, one is catalyzed by alanine aminotransferase (ATA), the other by glutamate-oxaloacetate transaminase (AAT):

$$\alpha\text{-Ketoglutarate + alanine} \xleftarrow{\quad ATA \quad} \text{glutamate + pyruvate}$$

$$\alpha\text{-Ketoglutarate + aspartate} \xleftarrow{\quad GOT \quad} \text{glutamate + oxaloacetate}$$
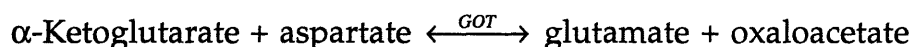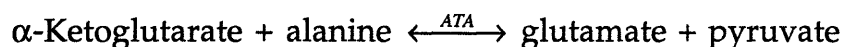
As acetate and butyrate were the major carbon source for oxidative metabolism in all the experiments, alanine and pyruvate concentrations were low and alanine aminotransferase activity is minimal. Therefore, the interconversion rates between α-ketoglutarate and glutamate, and between oxaloacetate and aspartate were set equal, i.e. $F_1 = F_2$. The optimization was performed using MATLAB (The MathWorks Inc., Natick, MA). The MATLAB programs for data fitting are included in Appendix C.

3.6 Sensitivity Analysis

Measurements of the TCA cycle intermediates that are at very low concentrations, α-ketoglutarate, malate, and oxaloacetate, are subject to great statistical fluctuations. To test the robustness of the model to such measurement errors, the effect of possible variations or errors in these pool sizes was evaluated by sensitivity analysis. Using parameters obtained from studies presented in Chapter 4, simulations were performed by perturbing

each pool size, and changes in ^{13}C turnover in glutamate pool were compared (Figures 3.4-3.6).

A simultaneous 200% change in pool sizes of α-ketoglutarate, malate, and oxaloacetate introduces very little change in glutamate labeling kinetics (Figure 3.4), indicating that even the most dramatic changes in these three intermediates have very little impact on the dynamics of glutamate ^{13}C enrichment. Figure 3.5 shows that a 90% change in either citrate or aspartate level, which is far beyond the experimental error range, also has little effect on glutamate enrichment curves. Glutamate, however, is by far the most sensitive pool (Figure 3.6). A 20% increase or decrease in its pool size introduces significant changes in its labeling curves. When the measurement is within 5%, this change becomes less important.
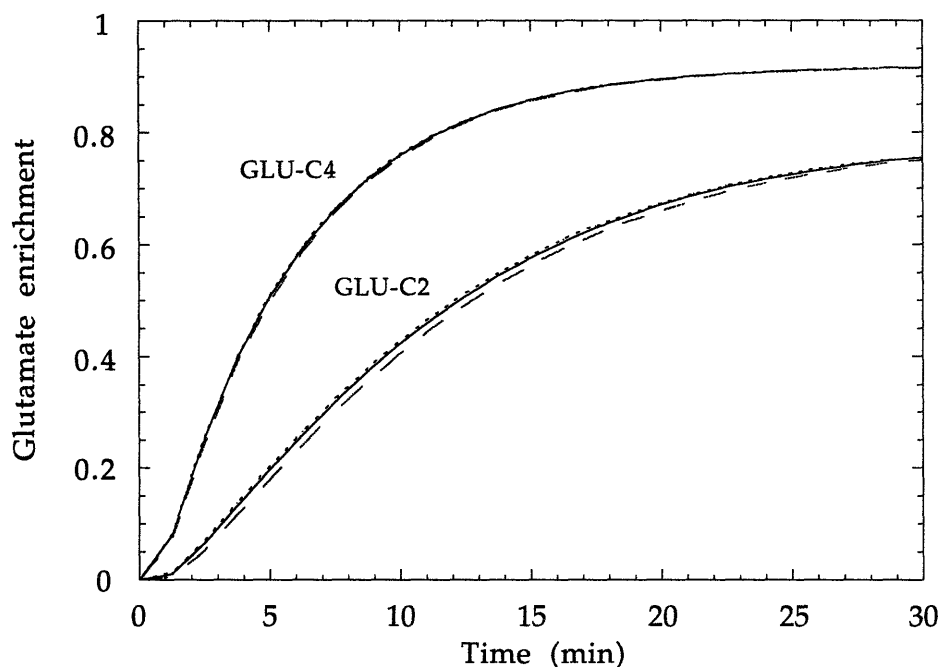
Figure 3.4 Sensitivity analysis. Simulated time course of glutamate enrichment with a simultaneous threefold increase (dashed lines) or decrease (dotted lines) in pool sizes of α-ketoglutarate, malate, and oxaloacetate shows little difference from that of measured pool sizes (solid lines). The minor impact of TCA intermediates on glutamate enrichment demonstrates the robustness of estimated parameters when measurements of TCA cycle intermediates are subject to large statistical fluctuations.
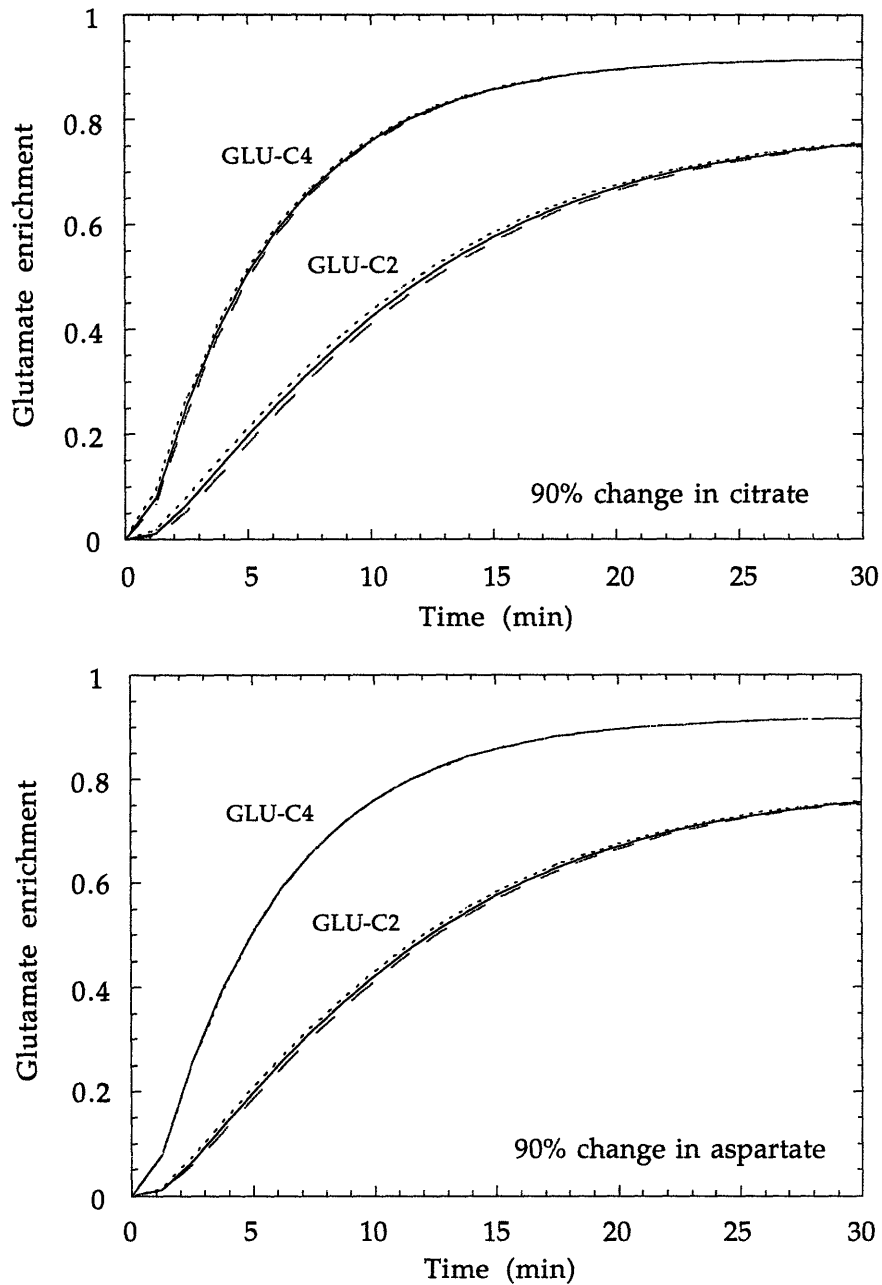
Figure 3.5 Sensitivity analysis. Simulated time course of glutamate enrichment with 90% increase (dashed lines) or decrease (dotted lines) in citrate (upper) or aspartate (lower) concentrations shows little difference from that of measured pool sizes (solid lines). This indicates that experimental measurement errors in citrate and aspartate can be tolerated in kinetic analysis.

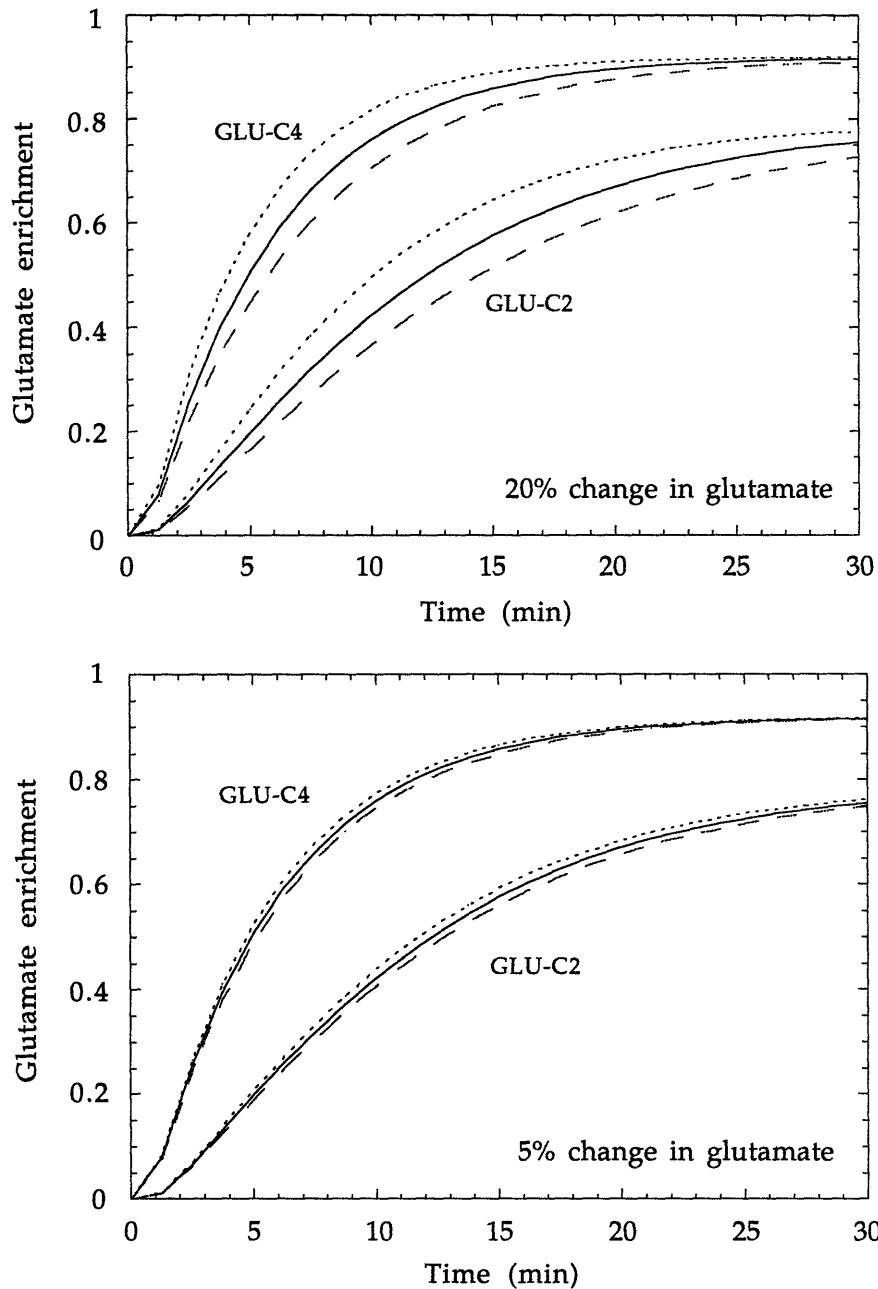**Figure 3.6 Sensitivity analysis.** Simulated time course of glutamate enrichment with 20% (upper) or 5% (lower) increase (dashed lines) or decrease (dotted lines) in glutamate concentration as compared to measured pool size (solid lines). The results demonstrate that changes in glutamate pool size can significantly affect the glutamate enrichment kinetics. Therefore, experimental measurement error in glutamate should be within 5%.

In summary, pre-steady state enrichment of glutamate is insensitive to large changes in α-ketoglutarate, malate, and oxaloacetate pool sizes at physiological levels. Measurement errors in citrate and aspartate can be tolerated, and the accuracy for glutamate measurement has to be within 5%. Similar results from sensitivity analysis have also been reported by other investigators (19, 131).

3.7 Practical Considerations

In this model, ^{13}C label entering the TCA cycle from acetyl-CoA pool is treated as a step function, with the underlying assumption that acetyl-CoA is instantly enriched to the level of F_c upon the delivery of ^{13}C-enriched substrate. Since the initial ^{13}C enrichment level of acetyl-CoA is also 1.1%, i.e. the natural abundant level of ^{13}C, whether or not this assumption is valid needs to be examined.

The enrichment of acetyl-CoA with ^{13}C upon the delivery of ^{13}C-enriched substrate can be depicted by the compartment model shown in Figure 3.7, with fluxes entering and leaving the compartment be the same as the TCA cycle flux at steady state. However, the flux of ^{13}C label entering the compartment is only $V_{TCA} \cdot F_c$ since other endogenous substrate is also oxidized via the TCA cycle. Therefore, the labeling kinetics for acetyl-CoA pool can be described by the following equation:

$$\frac{d}{dt}[^{13}C - AC] = V_{TCA} \cdot F_c - V_{TCA} \cdot \frac{[^{13}C - AC]}{[AC]}$$

where $[^{13}C - AC]$ is the concentration of ^{13}C-enriched acetyl-CoA, and $[AC]$ is the concentration of the total acetyl-CoA. Let AC^* be the ratio of ^{13}C-enriched acetyl-CoA to total acetyl-CoA, i.e.

$$AC^* = \frac{[^{13}C - AC]}{[AC]}$$

then

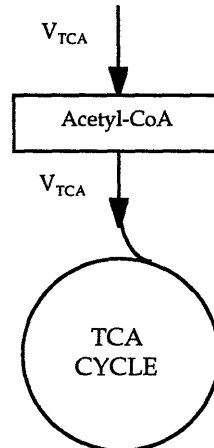$$\frac{d}{dt}AC^* = \frac{V_{TCA}}{[AC]} \cdot (F_c - AC^*)$$

Figure 3.7 Compartment model for acetyl-CoA enrichment.

To simplify the problem, assume the natural abundance level of ^{13}C is negligible, or the initial enrichment of acetyl-CoA is zero, i.e. $AC^*(0) \approx 0$. The labeling kinetics of acetyl-CoA then follows a simple monoexponential equation,

$$AC^*(t) = F_c \cdot [1 - \exp(-\frac{t}{[AC]/V_{TCA}})]$$

Therefore, the time course of acetyl-CoA enrichment occurs as an exponential function of time, with the time constant being the ratio of acetyl-CoA concentration in total to the flux through the TCA cycle. Since the physiological concentration of acetyl-CoA is approximately 0.2 μmoles/g dry weight only (96), the time constant for the enrichment of acetyl-CoA is very small. Using the TCA cycle flux determined from experiments in Chapter 4 (10.52 ~ 1.66 μmoles/min/g dry weight), the time constant for acetyl-CoA enrichment ranged from 0.02 to 0.12 minutes. Therefore, the enrichment level of acetyl-CoA 10 seconds after delivery of labeled substrate is already 75% of the steady-state value, by 30 seconds it is 98%. Thus, the assumption of instant equilibration of acetyl-CoA is a reasonable approximation.

The current model is derived from a simplified compartment model of the TCA cycle by eliminating several non rate-limiting pools. To justify this simplification, simulation results of the reduced model was compared with that of a more comprehensive model that also includes succinate and fumarate pools along with equations to describe both 2- and 3-carbon labeling (8 compartments, 19 differential equations) (139). These two models showed no difference in characterizing ^{13}C labeling kinetics of glutamate. A closer examination of the fractional enrichment of succinate, malate, and fumarate as a function of time shows that the downstream compartment follows the labeling pattern of the previous compartment very closely. This similarity in labeling dynamics of the TCA cycle intermediates is perhaps due to a relatively large TCA cycle flux as compared to the concentrations of the TCA cycle intermediates which are usually on the order of less than 1 μmole/g dry tissue weight.

Chapter 4

Changes in ^{13}C Turnover in Glutamate due to TCA Cycle Flux

This study was aimed at developing dynamic methods of ^{13}C NMR detection and techniques of kinetic data analysis to quantify rate-limiting events within intact hearts. Specific aims of this study were:

1) to establish the kinetic modeling method in the analysis of dynamic ^{13}C NMR spectra;

2) to test the capacity of the model by introducing various perturbations to the metabolic system;

3) to identify rate-limiting steps in isotope enrichment of glutamate by kinetic analysis method.

Experiments were designed to monitor ^{13}C enrichment rates within the glutamate pool of isolated hearts. Dynamic ^{13}C NMR spectroscopy was used to assess the influences of physiological demand and metabolic flux on the turnover of ^{13}C label in the intact heart. Studies were aimed at testing the relative contributions of the TCA cycle flux and the interconversion rate between α-ketoglutarate and glutamate to the presteady-state evolution of ^{13}C label within the NMR detectable glutamate pool. Isotope kinetics was evaluated with the manipulation of the TCA cycle flux secondary to either activity through β-oxidation (acetate versus butyrate) or altered metabolic demand (mechanical work versus basal metabolic state). Comparison of glutamate-oxaloacetate transaminase rate to isotope exchange rate allowed potential rate-limiting steps in glutamate enrichment to be identified.

4.1 Using Substrate and Workload to Change the Metabolic State of the System

Two short chain fatty acids, acetate (CH_3-COO^-) and butyrate (CH_3-CH_2-CH_2-COO^-), were chosen as the substrate in this study since fatty acids are the preferred substrate for myocardium. Although both acetate and butyrate are short chain fatty acids, their entry into the TCA cycle takes a different pathways and are, therefore, regulated differently. Acetate, having only two carbon atoms, is transported directly into the mitochondria and is thereby

converted to acetyl-CoA by mitochondrial acetate synthetase. It is readily oxidized by the perfused heart and causes an elevation of acetyl-CoA levels (86).

$$CH_3 - COO^- + CoASH \xrightarrow[\text{acetate synthetase}]{\text{ATP} \quad \text{AMP} + PP_i} CH_3 - \overset{\overset{\displaystyle O}{\|}}{C} - S - CoA$$
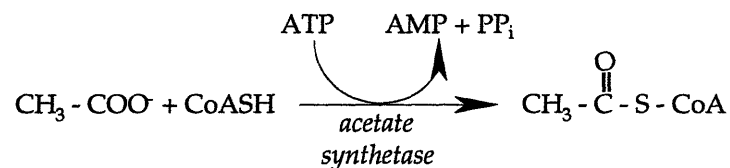
On the other hand, butyrate, as a four-carbon fatty acid, undergoes one turn of β-oxidation to be cleaved into two acetyl-CoA molecules before it is oxidized by the TCA cycle (Figure 1.3). Since β-oxidation is inhibited by high mitochondrial redox state, the increase in acetyl-CoA is less significant then acetate oxidation. Furthermore, β-oxidation of butyrate also generates additional reducing equivalents that are energy yielding and require oxygen to be reoxidized. Thus, at the same workload, β-oxidation also generates energy required by the myocardium, and less energy is derived from the TCA cycle. As a consequence, the TCA cycle flux from butyrate oxidation is slow compared to acetate oxidation when oxygen consumption rate is the same. In this way, butyrate induces changes in the TCA cycle activity without changing the respiratory rate and contractile performance of the myocardium. Therefore, while ^{13}C-enriched acetate has direct entry and rapid turnover of label in the TCA cycle, ^{13}C-enriched butyrate offers regulated entry of label into the TCA cycle through β-oxidation.

It is necessary to point out that neither acetate nor butyrate are physiological substrates for the *in vivo* hearts. However, these two substrate present the simplest scenario for studies that aim at the characterization of rate-limiting steps in isotope kinetics, while more physiological substrates, such as long chain fatty acids, would introduce new rate-limiting steps in the incorporation of label into the glutamate pool, i.e. activation and transport of long chain fatty acids into the mitochondria (11). Therefore, the choice of acetate and butyrate as the sole exogenous substrate offers a simple, well-controlled model that serves the purposes of this study well.

The energy requirement of the heart is thought to consist of a basal component utilized in maintaining the viability of myocardial tissue, while contraction is associated with further oxygen consumption and ATP

generation in proportion to work performed (85). Previous investigations have determined that the basal metabolism of the heart comprises 10 to 20% of the total myocardial oxygen consumption and ranges from 5 to 10 μmoles/min g dry weight (8, 134). The heart is capable of responding to a wide range of load demands by an increase of metabolic activity, without significant changes in the myocardial contents of adenine nucleotides, creatine phosphate, and the TCA cycle intermediates. Previous studies with the isolated perfused heart have established an approximately linear correlation between cardiac work and oxygen consumption (8, 66, 85). Hence, changes in workload can introduce another perturbation to the metabolic system by changing the metabolic activity of the heart.

In this study, metabolic activity of heart at normal workload was compared to heart at basal metabolic state. Basal metabolism was achieved by supplying the heart with an excess amount of potassium (potassium arrest). High extracellular concentration of potassium decreases the cellular resting membrane potentials so that myocyte contractions are no longer generated. Once contraction is abolished, energy is used mainly for maintenance of the cell ionic milieu (e.g. the Na^+-K^+ ATPase) and macromolecular synthesis (7).

There were four experimental groups in this study. They were comprised of hearts perfused with 1) 2.5 mM acetate (n=7); 2) 2.5 mM butyrate (n=7); 3) 2.5 mM acetate + 20 mM KCl (n=5); and 4) 2.5 mM butyrate + 20 mM KCl (n=5). Additional experiments were done with hearts perfused with [2, 4-^{13}C] butyrate at normal workload to eliminate the partial labeling of acetyl-CoA from β-oxidation (n=4). At the start of each protocol, heart was perfused with either unlabeled acetate or butyrate for 10 minutes to reach metabolic equilibrium according to the experimental protocol described in Chapter 2. The substrate supply was then switched to the corresponding ^{13}C-labeled substrate: either [2-^{13}C] sodium acetate or [2-^{13}C] sodium butyrate (Isotec Inc., Miamisburg, OH), with or without KCl. Sequential ^{13}C spectra were then acquired every 1.25 (acetate, 32 free induction decays) or 2.5 (butyrate, 64 free induction decays) minutes until steady-state enrichment was reached.

4.2 Experimental Results

4.2.1 Contractile Function and Oxygen Consumption

Mechanical performance and oxygen consumption are tabulated in Table 4.1. Contractile function, assessed by rate-pressure-product (RPP), was similar for hearts at normal workload, and was maintained throughout the experiment as shown in Figure 4.1. Since acetate and butyrate have similar P:O ratio (2.75 for acetate and 2.8 for butyrate), oxygen consumption rate was also similar. The oxygen consumption (μmoles/min/g dry weight) to rate-pressure-product ratio (10^3 mmHg/min) was 1.27 in acetate group and 1.18 in butyrate group, similar to that reported by other investigators in isolated rat heart (8).

Table 4.1 Contractile function and oxygen consumption data.

	HR (beats/min)	LVDP (mmHg)	RPP (mmHg/min)	MVO_2 (μmoles/min/g dw)
Acetate	161±49	101±14	16,000±4,300	20.30±5.49
Butyrate	159±43	109±25	17,300±6,000	20.45±4.59
Acetate+KCl	–	–	–	7.45±1.39*
Butyrate+KCl	–	–	–	6.88±2.98*

HR, heart rate. LVDP, left ventricular developed pressure. RPP, rate-pressure-product. MVO_2, oxygen consumption. RPP is used as an index of contractile performance. All data are presented as Mean±SD. (* $p<0.05$ as compared to heart at normal workload.)

Hearts arrested with KCl generated no mechanical work. As expected, their oxygen consumption was significantly lower, only 34~37% of that of hearts at normal workload. These results are consistent with both previous findings (66) and data from canine and rat hearts reported by other investigators (8, 62). Thus, the protocol afforded analysis of ^{13}C kinetics at normal and basal metabolic rates in both the absence and presence of significant effects on the TCA cycle flux from additional NADH and $FADH_2$ generation by β-oxidation.
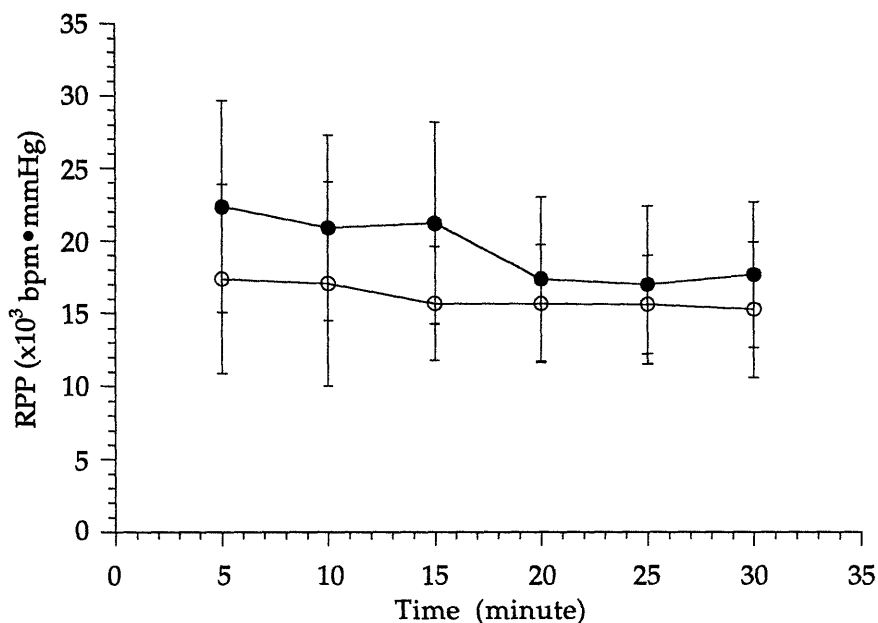
Figure 4.1 Functional stability over time. Contractile performance was maintained throughout the experiment in both groups. Open circle: acetate perfused heart; closed circle: butyrate perfused heart.

4.2.2 Energetic State of Phosphate Metabolism

Representative ^{31}P spectra from heart at both normal workload and potassium arrest are shown in Figure 4.2. Consistent with previous findings (66), hearts at basal metabolic state showed no difference in high energy phosphate metabolism over the course of perfusion. PCr to ATP ratios ranged from 1.84 to 2.49 and were similar among the four experimental groups. These data are also similar to those reported previously with pyruvate or lactate perfused hearts under the same NMR acquisition parameters (68, 72). Therefore, phosphorylation potentials were similar in all four experimental groups.
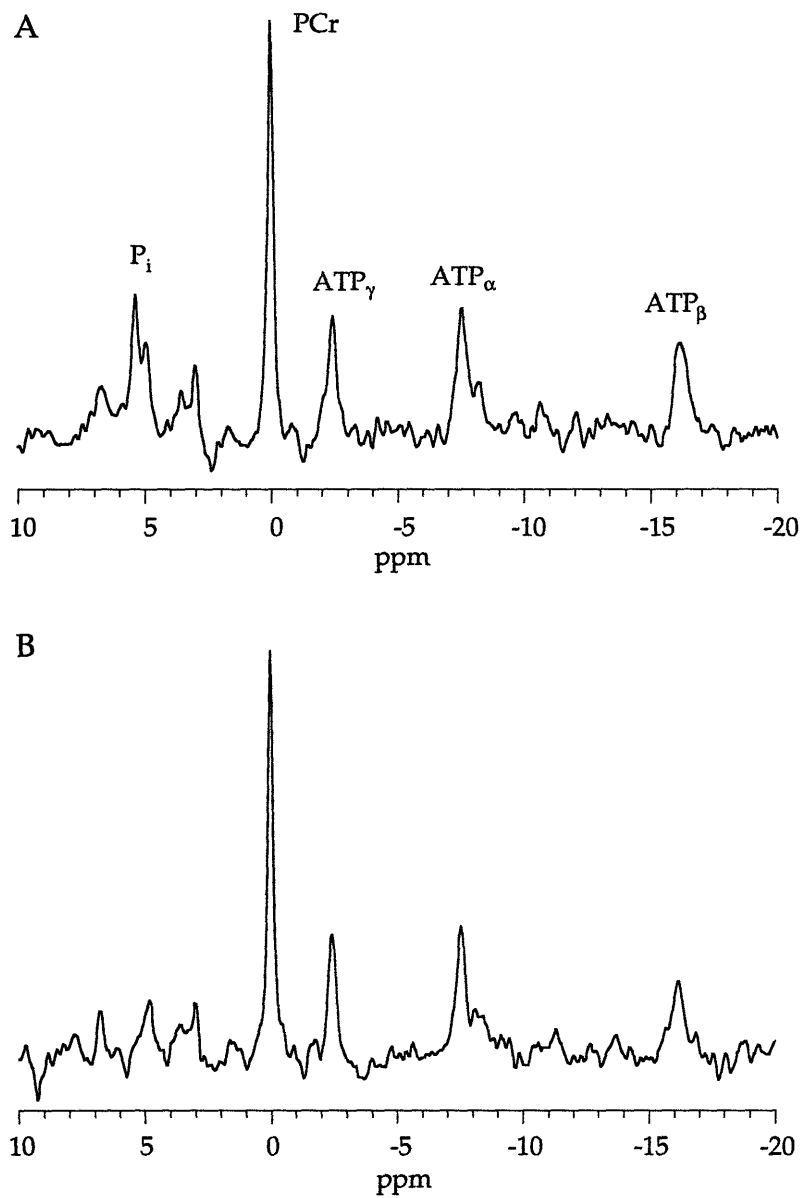
Figure 4.2 Representative ^{31}P spectra from heart perfused with acetate. Labeled peaks are inorganic phosphate (Pi), phosphocreatine (PCr), and the three phosphates of ATP (ATP$_\alpha$, ATP$_\beta$, and ATP$_\gamma$). (A) at normal workload; (B) at potassium arrest.

4.2.3 Metabolite Contents

Steady-state metabolite contents are tabulated in Table 4.2. Values are in agreement with those measured by other investigators with similar experimental conditions (98, 123). At normal workload, heart perfused with acetate has a higher level of citrate than heart perfused with butyrate

(p=0.012). This increase in citrate level can be explained by the so-called "unspanning" (98, 99) of the TCA cycle at high acetyl-CoA level with acetate perfusion, which causes the rate of citrate and isocitrate synthesis to exceed the flux through the rest of the TCA cycle (10, 97). The accumulation of citrate induces a shift in the glutamate-oxaloacetate transamination (10). Therefore, the aspartate level in acetate perfused heart appears to be lower than butyrate perfused heart (p=0.001), and correspondingly, the glutamate level with acetate perfusion is slightly higher (p=0.047). This shift in metabolite contents was not observed in heart at potassium arrest, probably due to the strong inhibition of the cycle when ATP and NADH levels were high with low energy demand.

Table 4.2 Steady state metabolite contents.

	Glutamate	α-Ketoglutarate	Citrate	Aspartate
Acetate	27.73±3.82	0.50±0.35	1.35±0.68	1.56±0.80
Butyrate	25.12±4.78*	0.59±0.31	0.84±0.34*	2.60±1.01*
Acetate+KCl	22.64±6.16	0.74±0.09	1.10±0.30	1.14±0.24
Butyrate+KCl	21.05±7.36	0.91±0.41	1.05±0.52	0.95±0.40

Metabolite contents are determined by enzymatic assays. All data are presented in Mean±SD and are given as μmoles/g dry tissue weight. (* p<0.05 as compared to acetate perfusion)

4.2.4 ^{13}C NMR of Tissue Extracts

Proton decoupled ^{13}C spectra of tissue extracts from hearts at both normal workload and basal metabolic state are shown in Figure 4.3 and Figure 4.4. Quantitatively, the multiplet components of spectra from potassium arrested hearts were similar to that of hearts oxidizing the same substrate at normal workload. [2-^{13}C] Butyrate induced a lower level of doublet signal from glutamate 4-carbon resonance because only 50% [2-^{12}C] acetyl-CoA, at most, entered the TCA cycle after butyrate was cleaved to produce two acetyl-CoA molecules by β-oxidation.

A

GLU-C2   GLU-C4   GLU-C3

```
  56.2   55.8   55.4   55      34.8   34.4   34      28.4   28   27.6   27.2
                                        ppm
```

B

GLU-C2   GLU-C4   GLU-C3

```
  56.2   55.8   55.4   55      34.8   34.4   34      28.4   28   27.6   27.2
                                        ppm
```
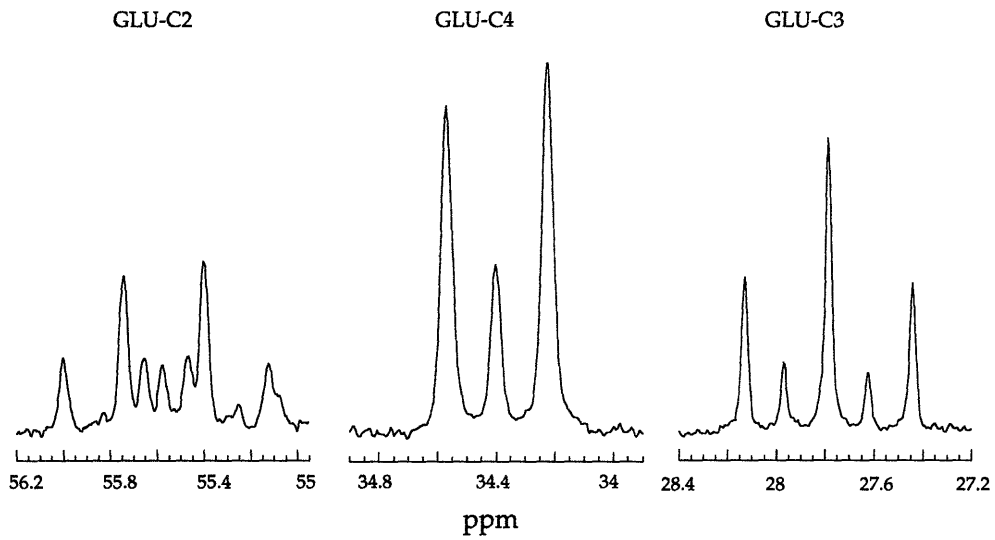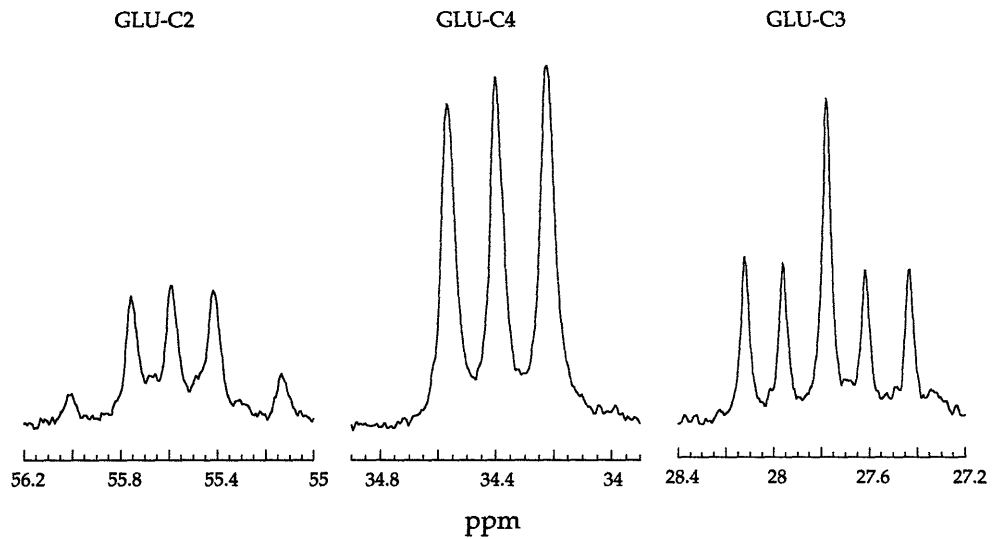
Figure 4.3 Glutamate resonances from high resolution ^{13}C NMR spectra of tissue extracts of [2-^{13}C] acetate perfused hearts. (A) At normal workload; (B) With potassium arrest.

A
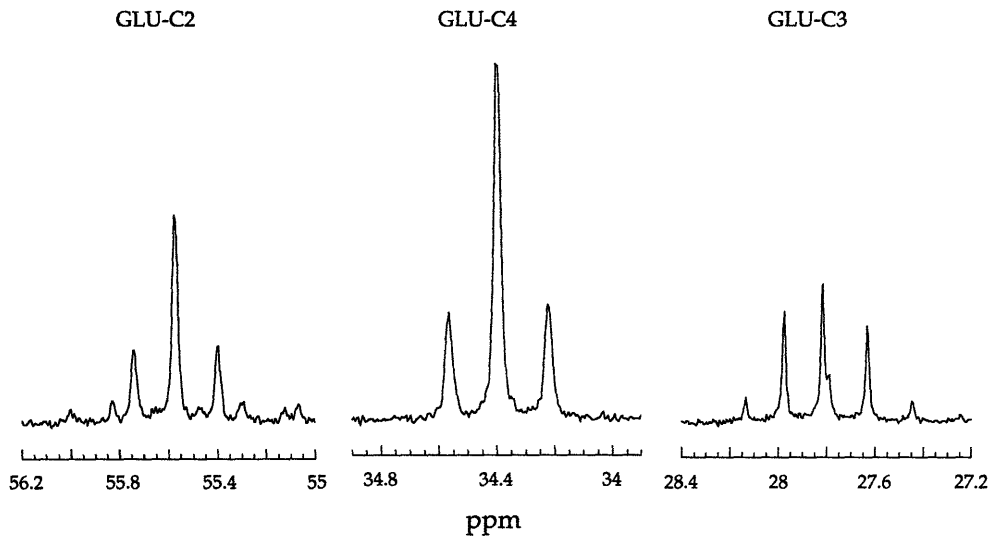
B
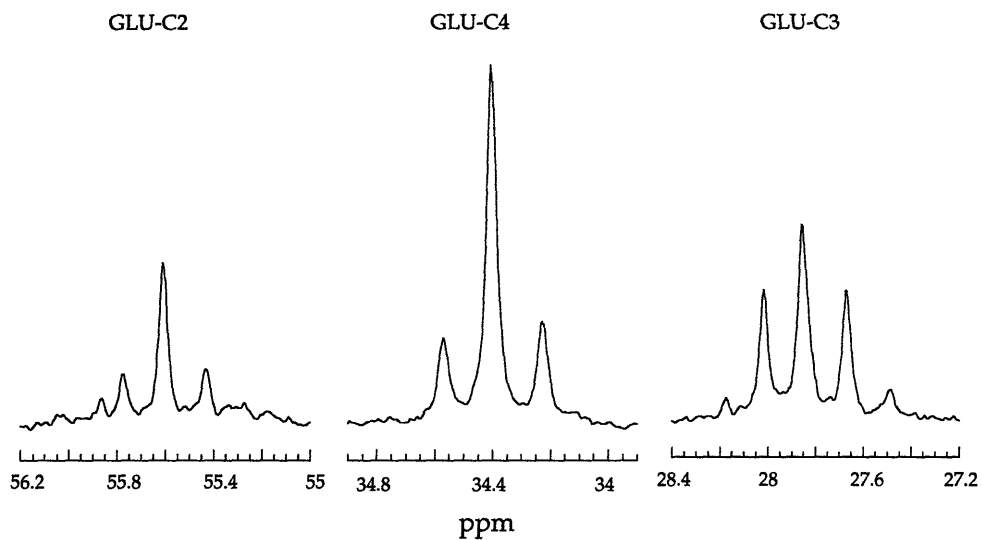
Figure 4.4 Glutamate resonances from high resolution ^{13}C NMR spectra of tissue extracts of [2-^{13}C] butyrate perfused hearts. (A) At normal workload; (B) With potassium arrest.

The fraction of ^{13}C enriched acetyl-CoA entering the TCA cycle (F_c) and the ratio of anaplerotic flux to citrate synthase activity (y) calculated from high resolution ^{13}C NMR spectra are presented in Table 4.3. The calculated F_c and y values showed no statistically significant difference with the same

perfusate supply. As expected, F_c values with hearts oxidizing [2-^{13}C] butyrate at both normal workload and with potassium arrest were less than 50%, only half of those with hearts oxidizing [2-^{13}C] acetate due to the enrichment difference discussed above.

Table 4.3 Fc and y values from high resolution NMR spectra.

	Fc	y
Acetate	91.6±5.9	8.2±4.1
Butyrate	46.2±4.1	14.7±8.7
Acetate+KCl	91.9±1.5	11.4±5.3
Butyrate+KCl	46.8±4.2	22.1±11.8

Fc, fraction of ^{13}C-enriched acetyl-CoA entering the TCA cycle. y, ratio of anaplerosis to citrate synthase activity. Values of Fc and y were determined from high-resolution NMR spectra of tissue extracts. Data are presented in Mean±SD.

4.3   Kinetic Analysis of Dynamic ^{13}C NMR Data

Figure 4.5 and 4.6 show representative, sequential ^{13}C NMR spectra of intact hearts from each experimental group. The label first appeared in the 4-carbon position of glutamate and subsequently in the 2- and 3-carbon positions as described in Chapter 3. Since acetate is readily converted to acetyl-CoA while butyrate undergoes regulated β-oxidation, resonance signal from butyrate is much higher than that from acetate. Not surprisingly, label appeared much slower in hearts at basal metabolic state (Figure 4.6) as compared to hearts at normal workload (Figure 4.5) due to reduced metabolic rate. However, the incorporation of label into the glutamate pool with [2-^{13}C] butyrate was also significantly delayed in reaching steady-state as compared to hearts oxidizing [2-^{13}C] acetate. This delay is evident in Figure 4.7 and 4.8 which show the time course of ^{13}C enrichment of glutamate at 2- and 4-carbons from all acquired spectra along with the results from least-square fitting.
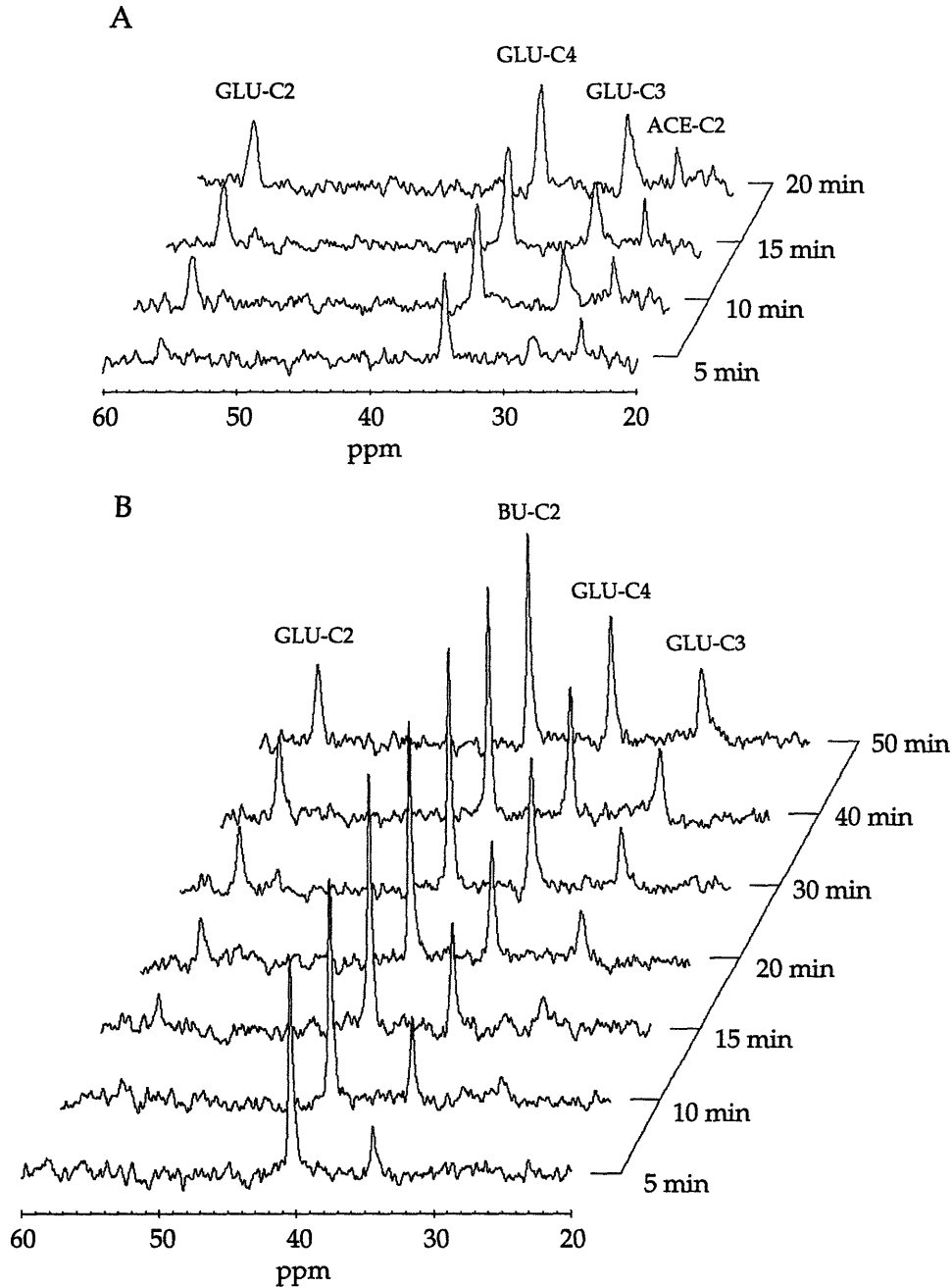
Figure 4.5 Dynamic ^{13}C spectra of isolated rabbit hearts at normal workload. Spectra were acquired during a period of 1.25 (A) or 2.5 (B) minute. Labeled substrates were 2.5 mM [2-^{13}C] acetate (A) and 2.5 mM [2-^{13}C] butyrate (B). Heart oxidizing acetate reached steady state in 30 minutes, while heart oxidizing butyrate reached steady state in 40 minutes. Identified resonance peaks are: GLU-C2, 2-carbon of glutamate; GLU-C4, 4-carbon of glutamate; GLU-C3, 3-carbon of glutamate; ACE-C2, 2-carbon of acetate; BU-C2, 2-carbon of butyrate.
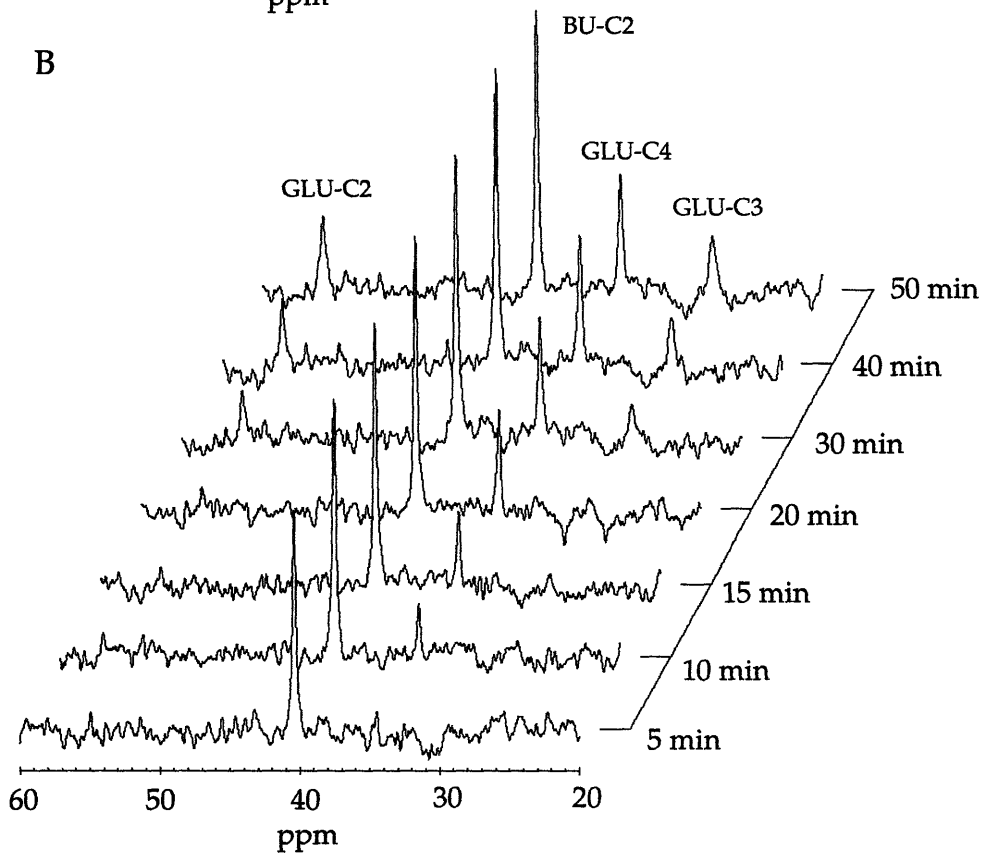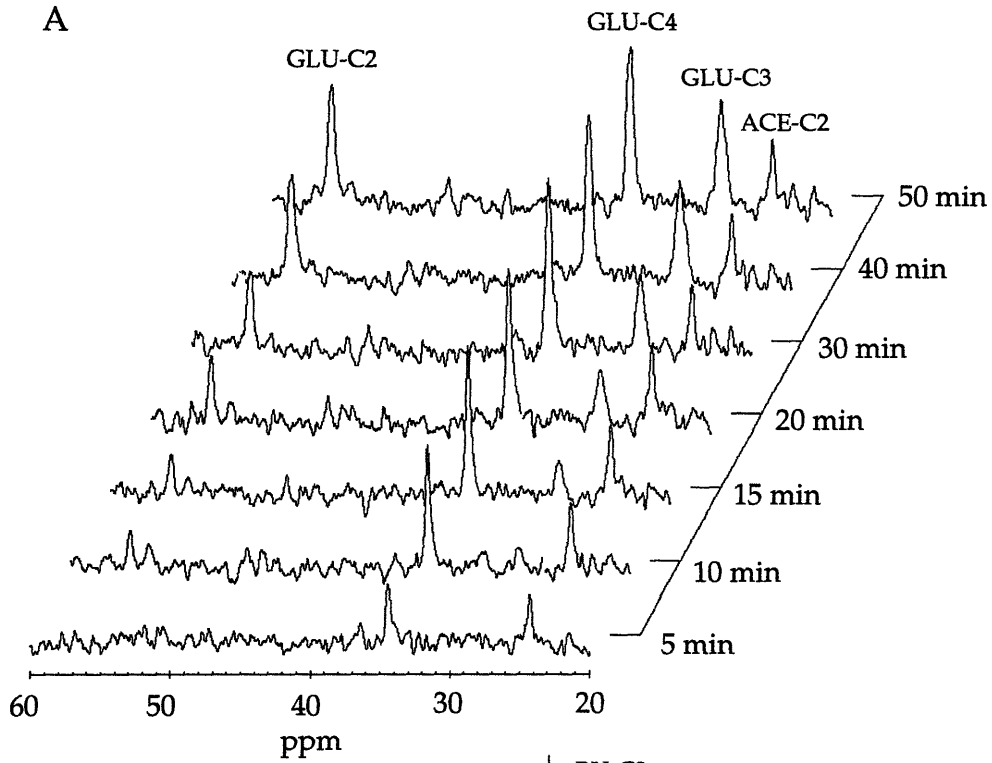
Figure 4.6 Dynamic ^{13}C spectra of isolated rabbit heart at potassium arrest. All spectra are acquired within 2.5 minutes. Labeled substrates were 2.5 mM [2-^{13}C] acetate (A) and 2.5 mM [2-^{13}C] butyrate (B).

The delayed approach to steady state with hearts oxidizing butyrate was quantified by the time constants of the labeling curves from a single exponential fit: in the acetate group, 7 min for the 4-carbon of glutamate (C4), 17 min for the 2-carbon (C2); in the butyrate group, 10 min for C4, and 32 min for C2. In potassium arrested hearts, the time constants were: with acetate, 14 min for C4, 46 min for C2; with butyrate, 21 min for C4, and 97 min for C2. However, these time constants can not be used as a direct index of the TCA cycle flux since the exchange of label between α-ketoglutarate and glutamate can also affect the labeling kinetics of glutamate.

Results from nonlinear least-square fitting of the kinetic model to glutamate labeling are shown in Figure 4.7 and 4.8. In all four groups, a good agreement of the model to the experimental data was evident. TCA cycle flux (V_{TCA}) and interconversion rate between α-ketoglutarate and glutamate (F_1) determined from data fitting are presented in Table 4.4 with the standard deviation calculated from the Jacobian matrix of the model. Potassium arrested hearts showed significantly reduced TCA cycle flux, only 21~27% of that of hearts at normal workload. On the other hand, hearts oxidizing butyrate also have reduced TCA cycle activity as compared with hearts oxidizing acetate, despite similar oxygen consumption and workload. The result is due to the β-oxidation of butyrate as additional reducing equivalents are generated to meet the energy requirement of the myocardium at a correspondingly lower TCA cycle flux. The interconversion rate between α-ketoglutarate and glutamate was also slower in hearts perfused with butyrate. In combination, the reduced TCA cycle flux and the slower interconversion rate accounted for a general delay in the observed ^{13}C enrichment curve from hearts oxidizing butyrate.

Table 4.4 Flux parameters determined from kinetic analysis.

	TCA flux	Interconversion rate	r^2
Acetate	10.52±0.35	10.67±1.01	0.98
Butyrate	8.00±0.23	4.35±0.30	0.99
Acetate+KCl	2.87±0.13	6.52±1.11	0.99
Butyrate+KCl	1.66±0.11	4.08±0.92	0.99

Data are presented in Mean±SD and are given as μmoles/min/g dry tissue weight. Correlation coefficient r^2 indicates the goodness of fitting.
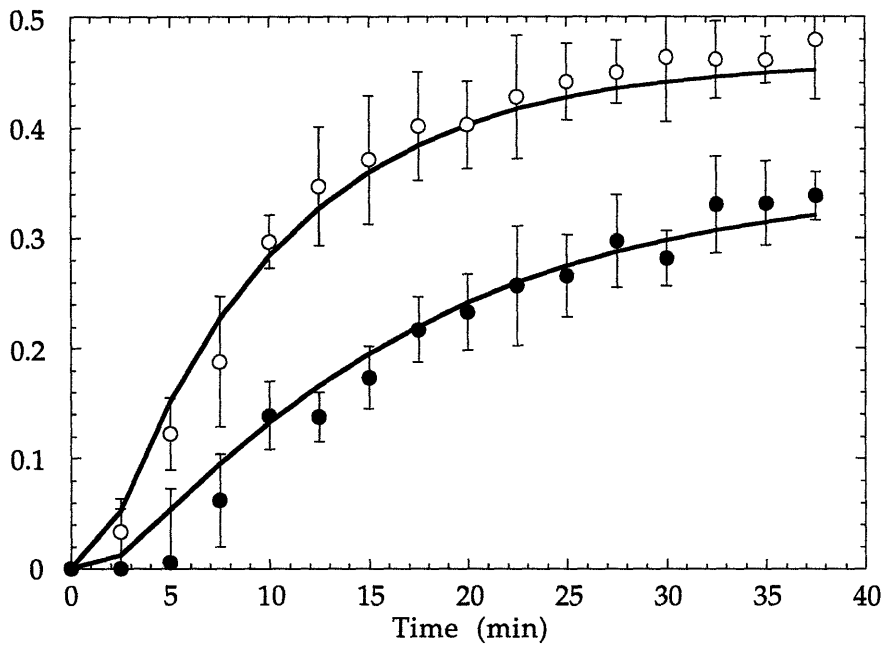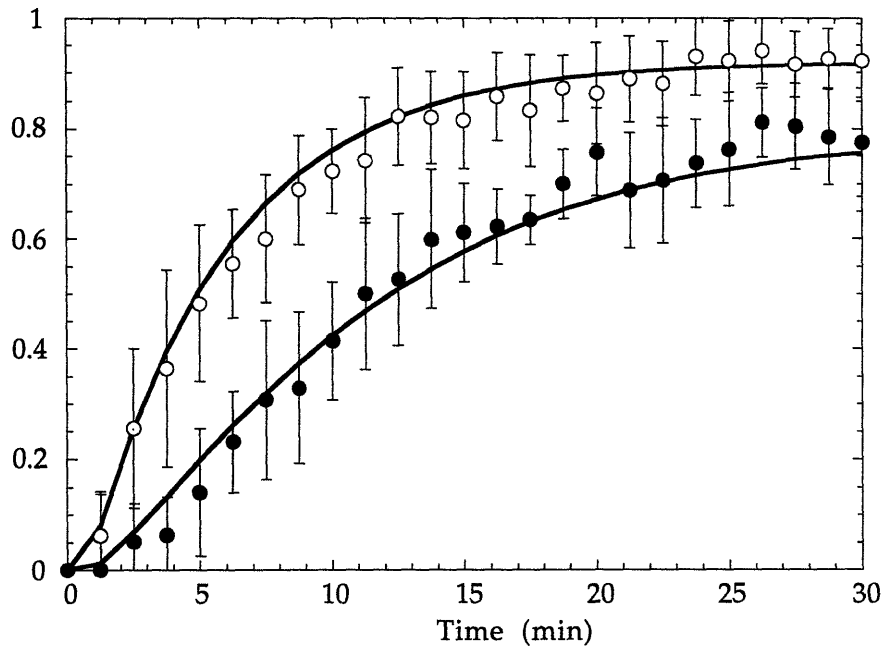
Figure 4.7 Time course of glutamate ^{13}C enrichment from NMR measurement and kinetic analysis. Hearts were supplied with either 2.5 mM [2-^{13}C] acetate (upper) or 2.5 mM [2-^{13}C] butyrate (lower). Signal intensities from dynamic ^{13}C NMR spectra are normalized to steady-state enrichment levels of the 4-carbon of glutamate. NMR data are shown in open and closed circles. Open circles, ^{13}C enrichment level of glutamate at 4-carbon position; closed circles, ^{13}C enrichment level of glutamate at 2-carbon position. Solid lines are fitted enrichment curves from kinetic analysis.
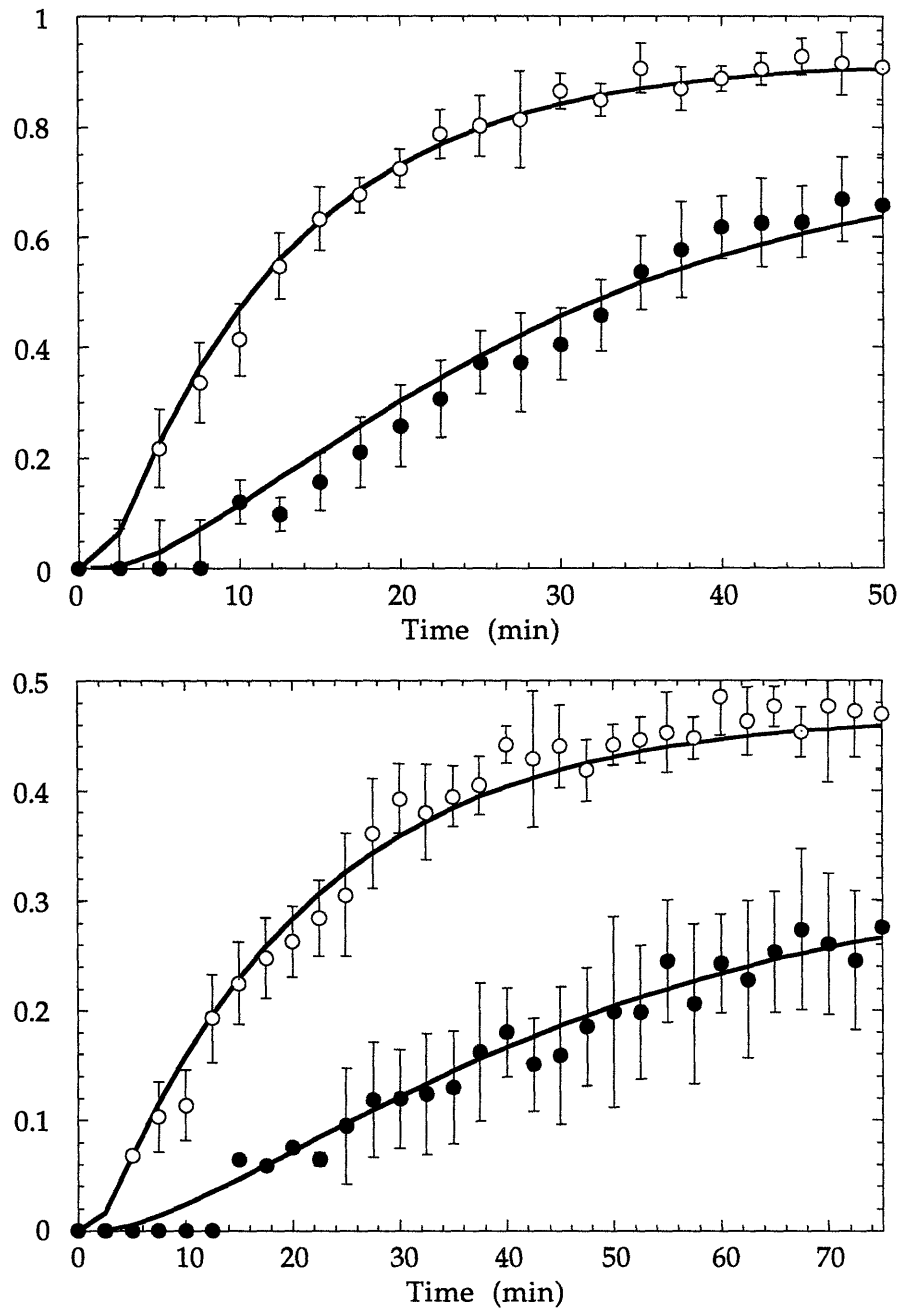
Figure 4.8 Time course of glutamate ^{13}C enrichment from NMR measurement and kinetic analysis. Hearts were at potassium arrest and were supplied with either 2.5 mM [2-^{13}C] acetate (upper) or 2.5 mM [2-^{13}C] butyrate (lower). Figure legends are the same as Figure 4.7.

4.4 Effects of Fractional Enrichment on ^{13}C Turnover in Glutamate

When the heart was supplied with [2-^{13}C] butyrate, only 50% of the acetyl-CoA generated from the β-oxidation of butyrate was ^{13}C enriched at 2-carbon. To test whether this partial enrichment of acetyl-CoA imposed an impact on the enrichment kinetics of glutamate, another set of experiments (n=4) was performed to supply the hearts with [2, 4-^{13}C] butyrate so that both acetyl-CoA molecules generated from β-oxidation were labeled at 2-carbon. ^{13}C spectra from tissue extracts showed elevated doublet signal in the glutamate 4-carbon resonance (Figure 4.9), resembling that of a heart perfused with [2-^{13}C] acetate (Figure 4.3). As expected, acetyl-CoA enrichment increased to 92.0±1.4%, comparable to that of hearts oxidizing acetate (91.6±5.9%). Yet anaplerosis was similar to hearts perfused with [2-^{13}C] butyrate: y=13.4±0.2%. Despite this high acetyl-CoA enrichment level, the dynamics of glutamate enrichment showed little difference from hearts oxidizing [2-^{13}C] butyrate (Figure 4.10). Using the same flux parameters obtained from curve fitting to data from the [2-^{13}C] butyrate group, the simulated enrichment curves were in good agreement with the experimental data (Figure 4.10). Therefore, the observed delay in glutamate labeling from hearts perfused with butyrate was induced by differences in metabolic activity rather than the dilution of label.
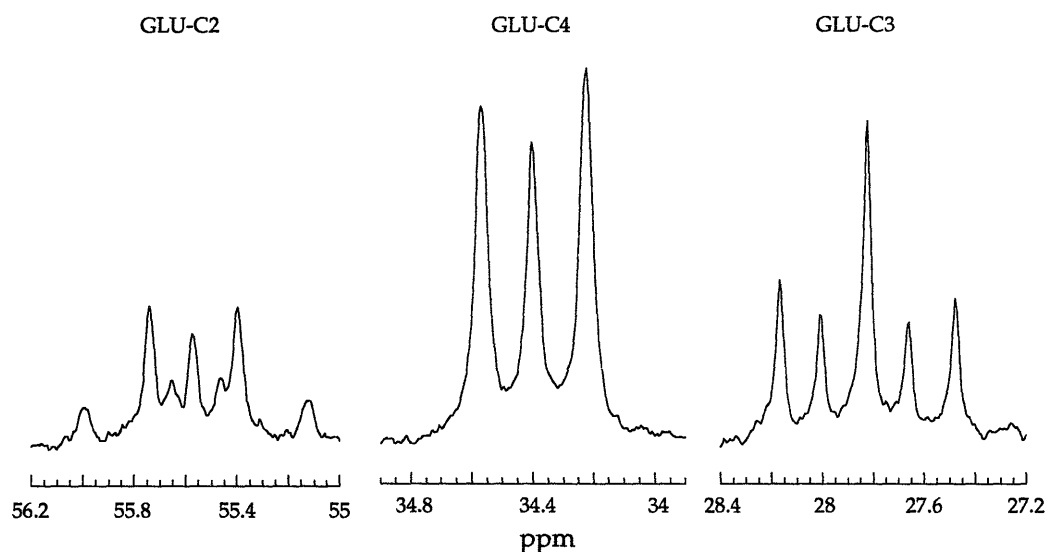
Figure 4.9 Glutamate resonances from high resolution ^{13}C NMR spectra of tissue extract of [2, 4-^{13}C] butyrate perfused heart. The multiplet structures resemble that of [2-^{13}C] acetate perfused heart.
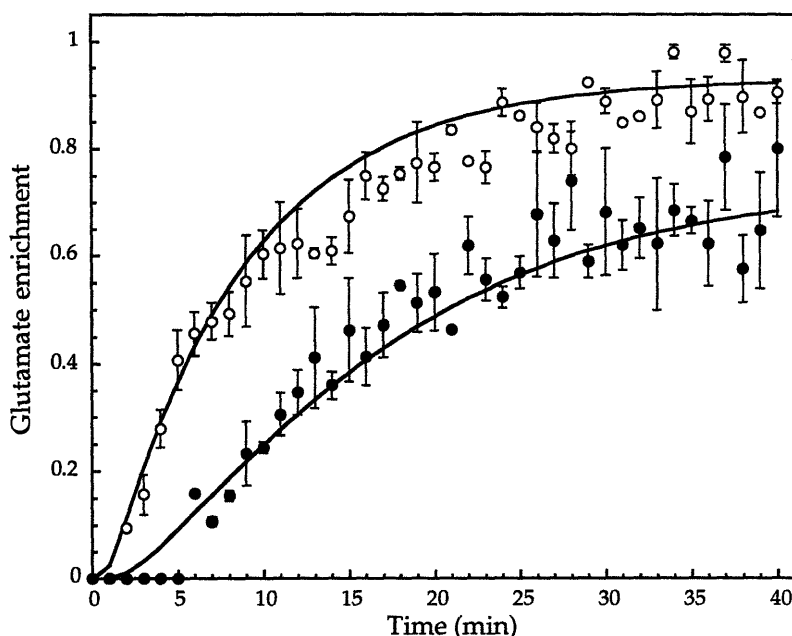
Figure 4.10 Glutamate ^{13}C enrichment from heart oxidizing [2, 4-^{13}C] butyrate. Open and closed circles are NMR measured ^{13}C enrichment levels of 2- and 4-carbons of glutamate from hearts perfused with [2, 4-^{13}C] butyrate (n=4). Solid lines are the simulated enrichment curves by using the same flux parameters obtained from kinetic analysis of [2-^{13}C] butyrate data presented in Table 4.4. The good agreement between simulated curves and experimental data is demonstrated.

4.5 Simulation of Glutamate Enrichment Using Transaminase Flux as the Exchange Flux between TCA Cycle Intermediates and Glutamate

The actual chemical exchange of ^{13}C label between α-ketoglutarate and glutamate from the TCA cycle occurs through a transamination reaction that also involves oxaloacetate and aspartate, and the enzyme catalyzes the reaction is therefore called glutamate-oxaloacetate transaminase (GOT), or aspartate aminotransferase (AAT). Two isoforms of GOT exist, mitochondrial and cytosolic. Although the catalytic mechanism of GOT has been extensively explored and fully elucidated (79, 84, 119), the reaction rate of GOT for rabbit heart has not been characterized.

In collaboration with Dr. LaNoue at the Hershey Medical Center of Pennsylvania State University, kinetic parameters of both cytosolic and mitochondrial GOT were measured in an effort to characterize the transaminase rate in *in vivo* heart. The measured K_m and V_{max} values of

GOT were presented in a published manuscript (140). Briefly, for the cytosolic GOT, V_{max} is 1.62 μmoles/min/mg total heart protein, and K_m for aspartate and α-ketoglutarate are 2.72 mM and 0.12 mM respectively. Based on these measured values and metabolite contents (Table 4.2) flux through GOT (F_{GOT}) can be calculated according to ping-pong reaction kinetics (127), i.e.

$$F_{GOT} = \frac{V_{max}}{1 + \dfrac{K_m^{ASP}}{[ASP]} + \dfrac{K_m^{\alpha KG}}{[\alpha KG]}}$$

Presented in Table 4.5 are the calculated *in vivo* GOT fluxes in all four experimental groups. In the calculation, heart protein to tissue weight ratio was taken as 683 mg total heart protein/g dry tissue weight and the volume to tissue weight ratio was 2 ml/g dry tissue weight (44). Since the transaminase reaction occurs mainly in the cytosol, kinetic parameters from cytosolic GOT were used in the calculation. α-Ketoglutarate and aspartate contents expressed in mM are also shown in Table 4.5 for comparison to their corresponding K_m values. It shows that α-ketoglutarate contents in all four groups are above its K_m of GOT, while aspartate contents are below. Therefore, aspartate concentration is the dominant factor in transamination rate. Hence, F_{GOT} was highest in the butyrate group due to a high aspartate concentration.

Table 4.5 Flux through glutamate-oxaloacetate transaminase.

	[ASP] (mM)	[αKG] (mM)	F_{GOT}	F_{GOT}/V_{TCA}	F_{GOT}/F_1
Acetate	0.78	0.25	223	21	21
Butyrate	1.30	0.30	316	40	73
Acetate+KCl	0.57	0.37	181	63	28
Butyrate+KCl	0.48	0.46	159	96	39

F_{GOT}: flux through glutamate-oxaloacetate transaminase (GOT) in μmoles/min/g dry tissue weight; V_{TCA}: flux through the TCA cycle; F_1: interconversion rate between α-ketoglutarate and glutamate. Both V_{TCA} and F_1 were determined from kinetic analysis.

Also shown in Table 4.5 are the ratios of F_{GOT}/V_{TCA} and F_{GOT}/F_1. The data demonstrate that the flux through GOT is indeed much faster than the flux through the TCA cycle. However, contrary to previous assumptions, the interconversion rate between α-ketoglutarate and glutamate (F_1) determined from least-square fitting of the model is at least 20 times slower than flux

through GOT (F_{GOT}) in all four groups and is on the order of the TCA cycle flux. These data suggest that another rate-limiting step exists in the labeling of glutamate.
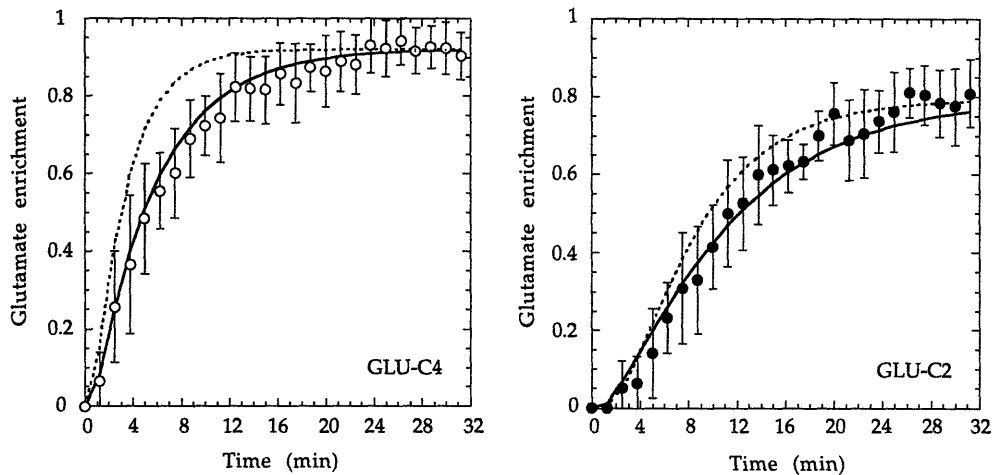
Figure 4.11 Difference between transaminase rate and interconversion rate. Using flux through glutamate-oxaloacetate transaminase (GOT) calculated from measured V_{max} and K_m of GOT as the exchange rate between α-ketoglutarate and glutamate, the simulated time course of glutamate ^{13}C enrichment (dotted lines) shows very poor agreement with the experimental data (circles, acetate group). Open circles: measured ^{13}C enrichment level of glutamate at 4-carbon; closed circles: measured ^{13}C enrichment level of glutamate at 2-carbon. Solid lines: simulated time course of glutamate ^{13}C enrichment using flux parameters determined from least-square fitting (acetate group).

Data fitting was also performed in the absence of the constraint provided by measured oxygen consumption. Removing this constraint caused a 9% deviation in TCA cycle flux and a 14% deviation in interconversion rate from the values obtained using the constraint. However, the interconversion rate remained on the order of the TCA cycle flux and was also significantly slower than the calculated GOT flux. A fixed TCA cycle flux, calculated from the lower limit of oxygen consumption, was also used so that only the interconversion rate was determined from data fitting, yielding increased interconversion rate for each group. However, these interconversion rates remained an order of magnitude lower than the GOT flux. If F_{GOT} alone was used to represent the isotope exchange rate, then simulated enrichment curves showed poor agreement with experimental data. The results of this test are shown in Figure 4.11. Therefore, flux through GOT is not the rate-

limiting step in the exchange between α-ketoglutarate and glutamate. This slow exchange rate might be a result of metabolite transport due to metabolite compartmentation, as the TCA cycle enzymes are intramitochondrial while a significant fraction of glutamate is cytosolic.

4.6 Discussion

In this study, changes in oxidative metabolism were studied at different workload demands and metabolic rates using ^{13}C NMR spectroscopy. The influence of these differences on the turnover of the ^{13}C label within the NMR-detectable glutamate pool were systematically examined. Dynamic ^{13}C spectra, reflecting the evolution of enrichment in the glutamate pool, were acquired with 1.25 or 2.5 minute temporal resolution from intact, functioning hearts. Oxygen consumption and mechanical performance in response to distinctly different physiological demands and metabolic regulation were constantly monitored during the acquisition of NMR spectra. Data acquired in this mode were analyzed with a kinetic model to determine metabolic fluxes and rate-limiting steps. The model was tested for its sensitivity to metabolite contents, respiratory rate, and transaminase activity from four experimental groups. Measured physiological constraints provided the experimental range of data fitting. The model integrates data from enzymatic assays, high resolution ^{13}C NMR data from tissue extracts, and dynamic changes in ^{13}C NMR spectra from intact hearts to evaluate metabolic regulation in functioning organs. From this study, both TCA cycle flux and the interconversion rate between metabolite pools were determined from the evolution of ^{13}C NMR signals from intact hearts for comparison to experimentally measured enzyme kinetics.

The current simplified model is a modification of that developed by Chance *et al.* (17). By considering the total labeling of carbons at 2-, 3-, and 4-carbons instead of individual isotopomer, it was possible to take the advantage of the symmetry in isotope labeling at the 2- and 3-carbon positions of the metabolic intermediates to reduce the number of equations necessary to represent the entire model. Consequently, only nine differential equations were needed in representing the kinetics of isotope turnover within the glutamate pool. Sensitivity analysis was also performed to test the robustness of the model to changes in TCA cycle intermediates. By incorporating data

from the analysis of high resolution ^{13}C spectra of heart extracts, anaplerosis and substrate utilization were also accounted for in kinetic analysis, leaving only two parameters to be fitted from the model. Therefore, this model has the advantage of being simple in its formality and yet including as much biological information as possible with a minimal number of adjustable unknowns.

Oxidative metabolism in response to various workload has been previously investigated using ^{13}C NMR spectroscopy and delayed incorporation of ^{13}C label into the glutamate pool for hearts at lower workload or basal metabolic state was reported (66, 131). In this study, in addition to changed workload condition, substrates with different metabolic pathway (β-oxidation versus no β-oxidation) were used to investigate the effect of metabolic control on the kinetics of glutamate enrichment. Hearts oxidizing butyrate showed similar contractile performance as hearts oxidizing acetate. The oxygen consumption rate was also similar. When partial labeling of acetyl-CoA from [2-^{13}C] butyrate oxidation was accounted for, the utilization of exogenous substrate for both substrates was also similar. Despite all these similarities, the time course of ^{13}C enrichment in glutamate pool for hearts oxidizing butyrate showed a significantly delayed approach to steady-state in both normal and KCl arrested hearts. When [2, 4-^{13}C] butyrate was used as the substrate, the fraction of ^{13}C enriched acetyl-CoA reached the same level as hearts oxidizing [2-^{13}C] acetate, yet kinetics of glutamate enrichment remained unchanged. Kinetic analysis show that this delay is largely due to a slower TCA cycle flux, which is consistent with the metabolic regulation of butyrate oxidation as additional reducing equivalents are generated in β-oxidation to reduce the demand of energy production from the TCA cycle.

Substrate utilization and relative flux of anaplerosis were also determined from high resolution NMR spectra of tissue extracts. While substrate utilization was found to be the same for both short chain fatty acids regardless of working conditions, the ratio of anaplerosis to citrate synthase activity (y) increased slightly at basal metabolic state (Table 4.3). However, care must be taken in interpreting y values, which is an index of relative contribution of anaplerosis to TCA cycle activity. Although y increased slightly with potassium arrested hearts, the calculated anaplerotic flux ($y \times V_{TCA}$) was, on the

other hand, lower than that of hearts at normal working conditions: 0.86 µmoles/min/g dry tissue weight with acetate only; 0.33 with acetate plus KCl; 1.18 with butyrate only; 0.37 with butyrate plus KCl. Therefore, while hearts at the same workload condition have similar anaplerotic flux, hearts at basal metabolic state have a relatively lower anaplerotic flux due to lower energy requirement.

An important consideration of earlier applications of ^{13}C dynamics is the omission of potential rate-limiting steps beyond that of TCA cycle flux alone (17, 34, 81, 82). While a potential effect of the transaminase rate on glutamate labeling was experimentally demonstrated by Weiss *et al* using a transaminase inhibitor (133), the physical compartmentation of the glutamate and TCA cycle intermediates must also be considered. This is important, because the GOT enzyme is not allosterically regulated and that the reaction rate is governed by the specific activity of the enzyme in the myocardium and the concentrations of the reactants in the tissue. Indeed, the characterization of the glutamate-oxaloacetate transaminase kinetics shows that the reaction rate of the transaminase is at least 20 times faster than the TCA cycle turnover (Table 4.5). However, kinetic analysis of glutamate labeling of intact hearts has suggested a significantly slower exchange rate between α-ketoglutarate and glutamate. It is on the order of TCA cycle flux in all four experimental groups. Since most of the tissue glutamate is located in the cytosol while the TCA cycle enzymes are located in mitochondria, there is membrane transport involved in addition to chemical exchange. Therefore, the findings of this study suggest that the slower exchange rate found in intact hearts is due to the transport of α-ketoglutarate across the mitochondrial membrane.

If the exchange of label between α-ketoglutarate and glutamate is rate-limiting, then the rate of isotope enrichment of glutamate will not precisely reflect isotope incorporation rates into the TCA cycle intermediates. Figure 4.12A shows the simulated time course of ^{13}C enrichment for both glutamate and α-ketoglutarate by using flux parameters determined from the acetate group. It is obvious that pre-steady state enrichment of glutamate has a significant delay as compared to the enrichment of α-ketoglutarate. Although only the group of hearts oxidizing acetate at normal workload is shown here, the other three groups showed similar delay in glutamate enrichment. Furthermore, since α-ketoglutarate is in constant chemical exchange with

glutamate, its labeling kinetics is ultimately determined by both TCA cycle flux and the exchange rate between α-ketoglutarate and glutamate. Therefore, even the enrichment of α-ketoglutarate cannot be simply regarded as an index of the TCA cycle. As can be seen from Figure 4.12B, the time course of α-ketoglutarate enrichment is very different from that of citrate, in which enrichment is solely determined by the TCA cycle flux.
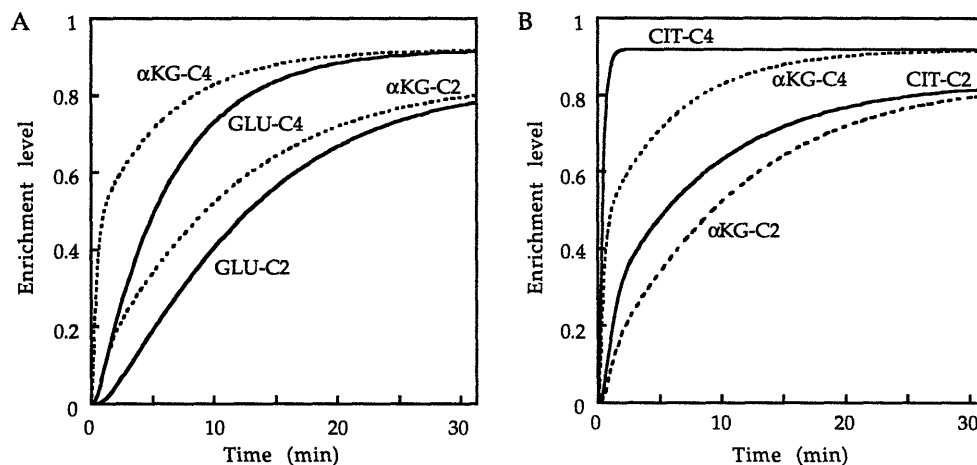
Figure 4.12 Simulated time course of ^{13}C enrichment of citrate, α-ketoglutarate and glutamate. Flux parameters are determined from least-square fitting of the kinetic model to NMR data in hearts oxidizing [2-^{13}C] acetate at normal workload. Differences in the enrichment kinetics between α-ketoglutarate (dotted lines) and glutamate (solid lines) (A), and between citrate (solid lines) and α-ketoglutarate (dotted lines) (B) are demonstrated here.

Metabolite contents in the whole cell have been used as the pool sizes in the kinetic model, making the tacit assumption that the gradients of these metabolites across the mitochondrial membrane are not large. Distribution of metabolites between the mitochondria and cytosol has been measured in perfused livers (118) using techniques difficult to apply to myocytes. These direct measurements have in fact never been made on heart tissue. However, conclusions can be drawn about the size of these metabolite gradients from studies of isolated mitochondria where the mitochondria have been rapidly separated from media for analysis (60), or where the NMR signal of metabolites inside the mitochondria can be distinguished from NMR signals of the external metabolites (43, 80). From these studies, the mitochondrial gradient of TCA cycle intermediates and glutamate and

aspartate can be considered to be lower in heart than in liver. In liver, a proton-linked glutamate transporter permits the formation of a glutamate gradient that is proportional to pH gradient across the mitochondrial membrane. The activity of this transporter is very low in heart, to the extent that glutamate influx into the mitochondria is determined by exchange of glutamate for aspartate. In liver, a transporter exchanges dicarboxylic acids for phosphate across a phosphate gradient that is supported by pH gradient (43, 80). However, the activity of the phosphate/dicarboxylate transporter in heart is very low and TCA cycle intermediates cross the mitochondrial membrane only via exchange with each other. Therefore, the assumption that the total intermediate pool sizes can be used as estimates of cytosolic fractions is valid.

Cytosolic glutamate fraction can be calculated from data obtained with isolated mitochondria. Transport of glutamate into heart mitochondria occurs almost exclusively via the glutamate/aspartate exchange transporter (59, 125). Thus, the total of glutamate plus aspartate content in mitochondria is constant at approximately 12 nmoles/mg mitochondrial protein (55), or 3.0 μmoles/g dry heart weight since the total mitochondrial protein to tissue weight is 250 mg/g dry weight (44, 135). This is the maximal concentration for mitochondrial glutamate, whereas total glutamate content ranged from 21 to 28 μmoles/g dry heart weight. Thus, a very large fraction of the glutamate pool (86-89%) is located in the cytosol. Therefore, ^{13}C NMR detection of isotope exchange between α-ketoglutarate and glutamate relies on the efflux of α-ketoglutarate from the mitochondria to the cytosol, which is accompanied by malate influx through an electroneutral malate/α-ketoglutarate antiport carrier in the malate-aspartate shuttle system (58, 59, 105).

Since glutamate and aspartate can both be distributed between the cytosol and the mitochondria, the interconversion rate between α-ketoglutarate and glutamate is really a lumped factor that involves both transaminase flux and transport rate. In the calculation of transaminase flux, due to the small mitochondrial space compared to cytosolic space and consistency of the mitochondrial glutamate plus aspartate pool, the majority of the metabolites are located in the cytosol. Data from isolated mitochondria suggest that mitochondrial content of glutamate and aspartate is approximately 12 nmoles/mg mitochondrial protein (55), aspartate alone is 1 nmole/mg

mitochondrial protein (56), and α-ketoglutarate is 0.4 nmoles/mg mitochondrial protein (60). This implies that 84% of the aspartate and 80% of the α-ketoglutarate are located in the cytosol. If correction is made according to these values, the calculated transaminase flux in the acetate group would be 192 μmoles/min/g dry tissue weight. However, this correction introduced no change to the simulated enrichment curves in Figure 4.11 (dotted lines), and therefore, still can not account for the significantly slower interconversion rate determined from kinetic analysis.

The interaction of the malate-aspartate shuttle with the TCA cycle provides a likely mechanism for the communication and coordination between mitochondrial and cytosolic metabolism (61). The relatively slow interconversion rate that was observed in the current set of experiments could be due to the influence of the malate-aspartate shuttle which transports several intermediates involved in the exchange of label. The process may be further influenced by shifts in the balance of these intermediates in response to changes in intracellular redox state (68). This study represents the first experimental evidence that this process is another rate-limiting step in determining the enrichment rate of glutamate. Thus, dynamic observations of intact tissues with ^{13}C NMR spectroscopy offer the opportunity to explore metabolic regulation at the level of both TCA cycle flux and the communication between intra- and extramitochondrial compartments.

In summary, sequential ^{13}C NMR spectra were obtained from intact hearts at either normal workload or basal metabolic state during perfusion with ^{13}C-enriched acetate or butyrate. A kinetic model was developed for the analysis of ^{13}C enrichment data to evaluate the regulations in oxidative metabolism and to identify rate-limiting steps in glutamate enrichment. From this analysis, the interconversion rate between glutamate and α-ketoglutarate was found to be slow relative to the transaminase rate from measured enzyme kinetics. Thus, the exchange of the glutamate pool with TCA cycle intermediates is influenced by rate-limiting processes beyond mere chemical exchange across enzymatic reactions. The implication of these results is that ^{13}C NMR is sensitive not only to TCA cycle activity but also to transport processes for isotope exchange across the mitochondrial membrane. This finding may provide ^{13}C NMR as a valuable new tool to monitor subcellular process, which previously could only be studied in isolated mitochondria.

Chapter 5

Subcellular Transport and the Effects of Cytosolic Redox State on Dynamic ^{13}C NMR Spectra

Studies presented in this chapter were aimed at exploring the potential of using dynamic ^{13}C NMR spectroscopy to observe metabolic communications between subcellular compartments. Experiments were designed to induce high cytosolic oxidation-reduction (redox) state by supplying the heart with exogenous lactate (141). Glutamate enrichment kinetics were found to be sensitive to changes in malate-aspartate shuttle activity.

5.1 Malate-Aspartate Shuttle Activity and Metabolite Transport at High Cytosolic Redox State

The carrier that mediates the transport of α-ketoglutarate across the mitochondrial membrane is part of the redox dependent malate-aspartate shuttle. In this shuttle, cytosolic oxaloacetate is reduced to malate which enters the mitochondria where it is reoxidized to oxaloacetate with release of NADH for reoxidation in the electron transport chain. Efflux of oxaloacetate from the mitochondria is kinetically limited, so that oxaloacetate is preferentially transaminated with glutamate to yield aspartate and α-ketoglutarate. α-Ketoglutarate leaves the mitochondria by a carrier mediated exchange with malate, while aspartate efflux is coupled with glutamate influx to complete the cycle. The latter exchange, being electrogenic, is energy consuming and induces unidirectionality to the malate-aspartate cycle since aspartate entry into mitochondria is very slow against the membrane potential (56, 58, 59).

If the transport of α-ketoglutarate is a rate-limiting process in ^{13}C NMR observation of glutamate labeling, than such observation might be sensitive to the changes in transport rate. In this study, the potential of using dynamic ^{13}C NMR spectroscopy to observe such process has been explore. Since malate-aspartate shuttle serves to transfer cytosolic reducing equivalents into the mitochondria, it is expected that an elevated cytosolic redox state would stimulate this shuttle and increase the transport rate of α-ketoglutarate.

In this study, ^{13}C turnover within the glutamate pool of intact, functioning rabbit hearts oxidizing ^{13}C-enriched substrates was observed with ^{13}C NMR spectroscopy at different cytosolic redox states induced by exogenous lactate. Isolated rabbit hearts were perfused with ^{13}C-enriched butyrate. The addition of lactate to the perfusion medium induced a relative increase in cytosolic redox state (NADH/NAD$^+$) for comparison of ^{13}C kinetics from hearts at high (2.5 mM lactate, n=5) versus low redox state (no lactate, n=5) (63, 109). Manipulation of cytosolic redox state during ^{13}C enrichment of the intramyocardial glutamate pool allowed us to determine whether such NMR observation of intact, functioning organs are sensitive to redox-dependent transport activity via the malate-aspartate shuttle.

The presence of lactate in the perfusate served the purpose to enhance the cytosolic redox state of the myocardium. Lactate in cytoplasm is convert to pyruvate in a reaction catalyzed by lactate dehydrogenase (LDH). In the meantime, NAD$^+$ is reduced to NADH.

$$Lactate + NAD^+ \xleftarrow{\ LDH\ } Pyruvate + NADH + H^+$$
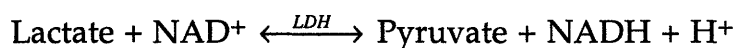
As the redox state in cytoplasm is elevated, an increase in the malate-aspartate shuttle activity is expected.

Pyruvate converted from lactate can either enter the TCA cycle through pyruvate dehydrogenase (PDH) or be transaminated to alanine via alanine aminotransferase (ATA). PDH is a multi-enzyme complex that catalyzes the decarboxylation of pyruvate:

$$Pyruvate + CoA + NAD^+ \xrightarrow{\ PDH\ } acetyl\text{-}CoA + CO_2 + NADH + H^+$$
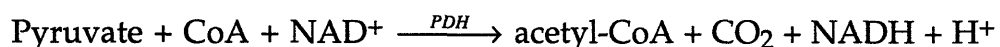
The acetyl-CoA generated in the above reaction can be further oxidized in the TCA cycle. The PDH complex exists in active (de-phosphorylated) and inactive (phosphorylated) forms, the interconversion of which is catalyzed by a phosphatase and an ATP-dependent kinase respectively (128). Fatty acid decrease the percent of PDH in the active form (28, 39). Therefore, the activity of pyruvate dehydrogenase is strongly inhibited. Hence, pyruvate will be mainly transaminated to alanine by exchanging an amino group with glutamate:

$$Pyruvate + glutamate \xleftarrow{\ ATA\ } alanine + \alpha\text{-ketoglutarate}$$
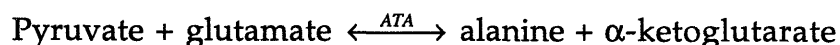
Under these experimental conditions, the alanine transaminase will slightly increase the total transaminase flux, and the net enzymatic interconversion between α-ketoglutarate and glutamate then becomes even less of a rate-limiting factor for ^{13}C enrichment of glutamate as compared to net interconversion rate.

5.2 *In vitro* Results

Table 5.1 Results from *in vitro* analysis. All data are presented in Mean±SD.

	Butyrate	Butyrate+Lactate
Glutamate (μmoles/g dry wt)	24.22±0.75	26.84±4.73
Aspartate (μmoles/g dry wt)	2.09±0.57	1.91±0.46
α-Ketoglutarate (μmoles/g dry wt)	0.32±0.04	0.29±0.06
Citrate (μmoles/g dry wt)	0.95±0.31	3.29±1.32*
[13]C-enriched acetyl-CoA, Fc (%)	47.7±4.1	48.0±2.2
Relative anaplerosis, y (%)	13.2±3.4	10.5±5.7

* $p < 0.05$ as compared to hearts perfused with butyrate only.

Steady state metabolite contents are shown in Table 5.1. Lactate induced an increase in citrate level by more than three-fold, from 0.95 μmoles/g dry weight to 3.29 (P=0.005). This shift in metabolite distribution is probably due to the interaction of the TCA cycle with the malate-aspartate shuttle in shuttling reducing equivalents from the cytosol into the mitochondria, as is depicted in Figure 5.1. As more malate enters the mitochondria to be oxidized to oxaloacetate, there is a transient increase of flux through citrate synthase accompanied by a transient decrease of flux through α-ketoglutarate dehydrogenase before a new steady state is established (106, 137). This imbalance of flux causes the citrate level to accumulate. A continuous reduction of oxaloacetate to malate in the cytosol also leads to a concomitant decrease in cytosolic aspartate level from 2.09 to 1.91 μmoles/g dry weight, as aspartate is deaminated to replenish the oxaloacetate pool. As a result, glutamate level increased slightly from 24.22 to 26.84 μmoles/g dry weight. Similar changes were also observed in rat heart when transition was made from substrate free perfusion to perfusion with glucose and insulin (137), and in guinea pig heart perfused with lactate only (112).

CYTOSOL   MITOCHONDRIA
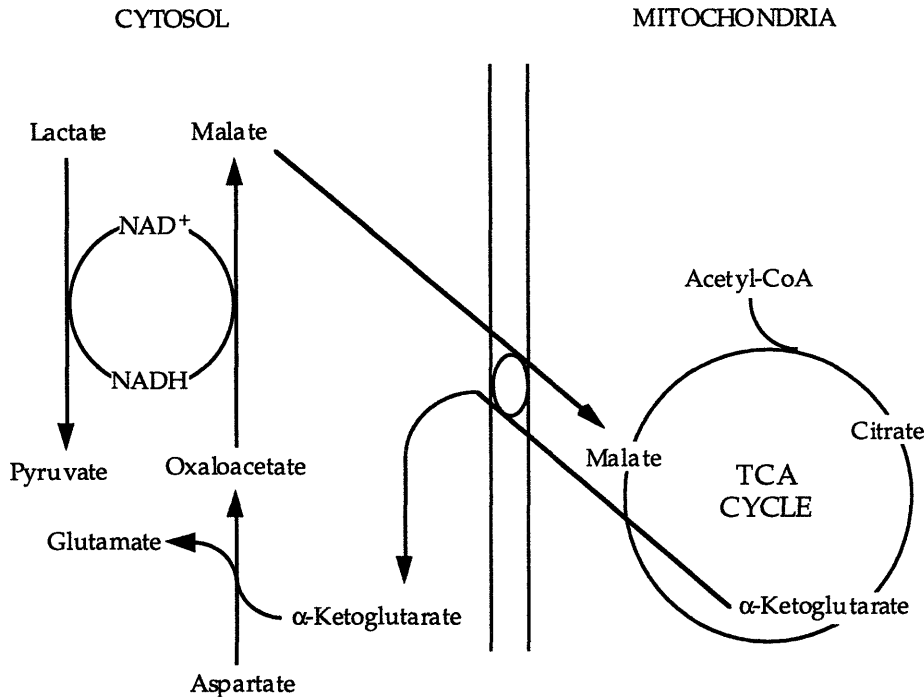
Figure 5.1 Interaction of malate-aspartate shuttle with the TCA cycle. Reoxidation of cytosolic NADH induces a continuous influx of malate into the mitochondria. Citrate accumulates due to the action of malate dehydrogenase and citrate synthase. Cytosolic aspartate level decreases as more aspartate is deaminated to replenish the oxaloacetate pool. Correspondingly, glutamate level increases slightly due to coupled transamination.

Fraction of ^{13}C-enriched acetyl-CoA (F_c) and relative anaplerosis (y) are also shown in Table 5.1. Both F_c and y values are similar in two groups. Again, the F_c values are less than 50% due to the fact that the single labeled [2-^{13}C] butyrate gives rise to one labeled and one unlabeled acetyl-CoA molecules. Taking into consideration this partial enrichment of acetyl-CoA, over 95% of the acetyl-CoA entering the TCA cycle was from butyrate in both groups, as was expected from the inhibition of pyruvate dehydrogenase by fatty acid oxidation (28). High resolution ^{13}C NMR spectra showed similar multiplet structure with and without the presence of lactate (Figure 5.2 and 4.4A). The similarity in these spectra demonstrate that the amount of butyrate oxidized by hearts with or without additional lactate was essentially the same. Therefore, hearts oxidizing ^{13}C-enriched butyrate did not utilize unlabeled exogenous lactate as a carbon source for oxidation.
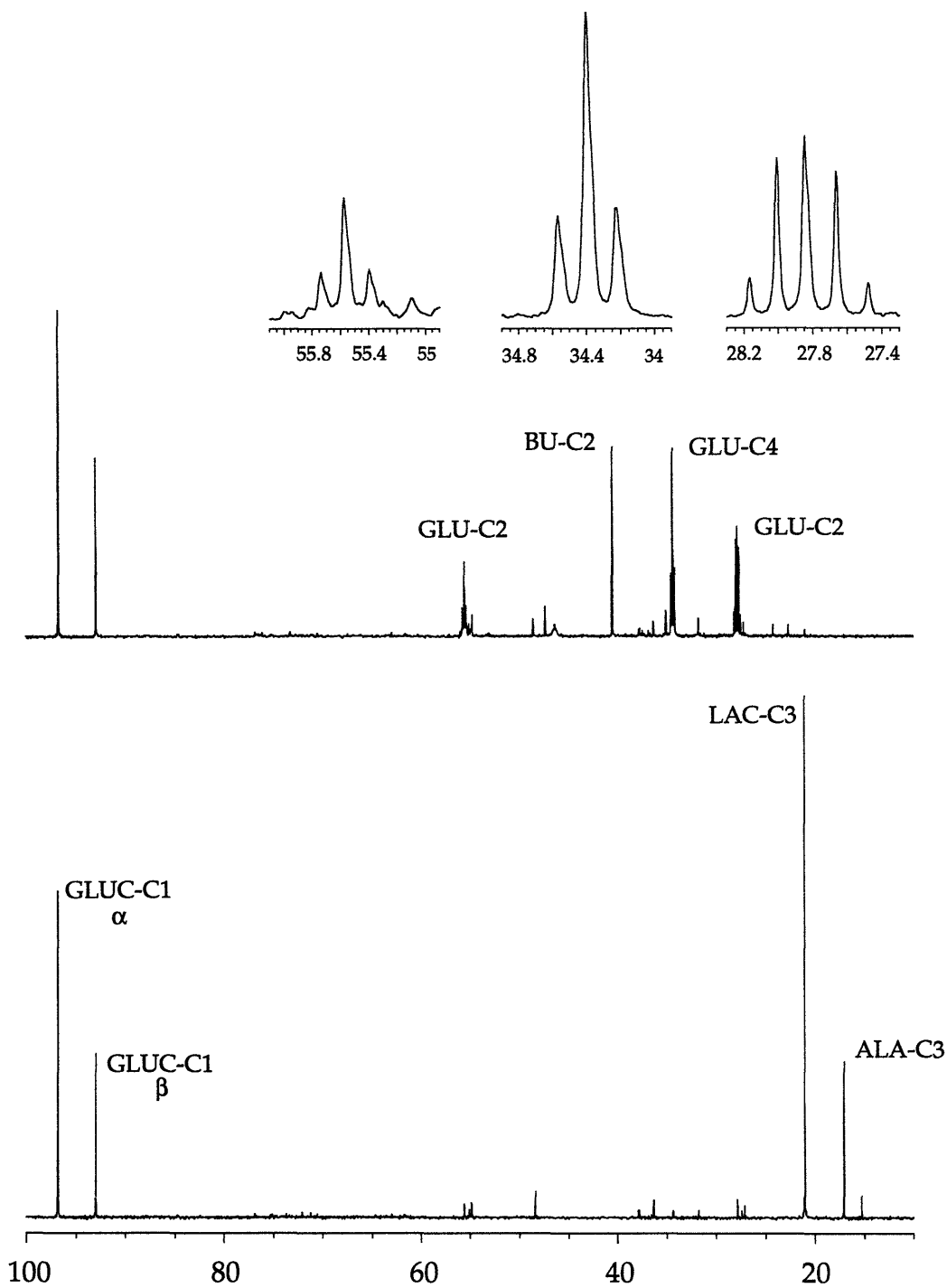
Figure 5.2 High resolution ^{13}C spectra of tissue extracts. (A) perfusion with [2-^{13}C] butyrate and unlabeled lactate; (B) perfusion with [3-^{13}C] lactate and unlabeled butyrate. The inset in (A) shows similar multiple structures to spectra from heart perfused with [3-^{13}C] butyrate only (Figure 4.4A), indicating similar acetyl-CoA enrichment and anaplerosis. The high intracellular level of labeled lactate and alanine in (B) indicates a high cytosolic redox potential due to the action of lactate dehydrogenase. Glucose signal serves as the concentration reference.

To further document the metabolic fate of the exogenous lactate, another set of hearts was supplied with 2.5 mM unlabeled butyrate plus 2.5 mM [3-^{13}C] lactate. Spectra of tissue extracts showed natural abundance level of ^{13}C enrichment in glutamate (Figure 5.2B), indicating that very little pyruvate was converted to acetyl-CoA to be oxidized in the TCA cycle. However, NADH production via conversion of lactate to pyruvate was indicated from the production of [3-^{13}C] alanine, as was clearly detected in both ^{13}C (Figure 5.2B) and ^{1}H (Figure 5.3) NMR spectra. Therefore, the effect of exogenous lactate was to increase cytosolic redox state (NADH/NAD$^+$) during the oxidation of [2-^{13}C] butyrate.
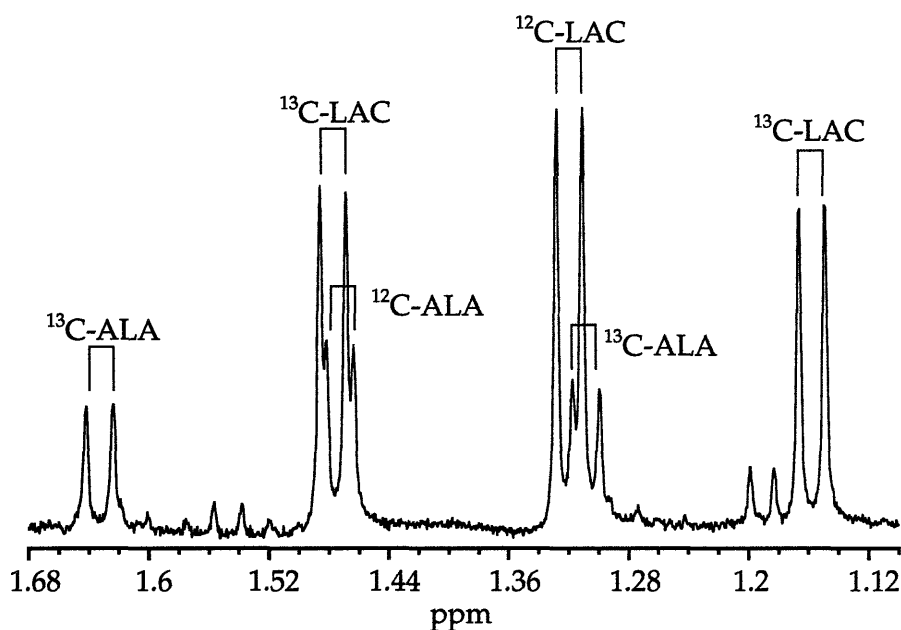
Figure 5.3 Proton spectrum of lactate and alanine. Tissue extract was from heart perfused with 2.5 mM [3-^{13}C] lactate and 2.5 mM unlabeled butyrate. Transfer of ^{13}C label from exogenous lactate to the 3-carbons of alanine is evident.

5.3 *In vivo* Results

Oxygen consumption rates (MVO$_2$) were similar between the two groups: 25.32±3.21 μmoles/min/g dry weight for hearts oxidizing butyrate only and 24.71±3.06 for hearts perfused with both butyrate and lactate. Mechanical performance was also similar. Hearts perfused solely with butyrate had an left ventricular developed pressure (LVDP) of 101±22 mmHg and heart rate

(HR) of 147±16 beats/min. LVDP and HR for hearts perfused with both butyrate and lactate were 113±20 mmHg and 151±23 beats/min respectively. Rate-pressure-products (RPP) were 14,700±3,100 mmHg/min for hearts oxidizing butyrate only and 17,000±4,300 for hearts perfused with both butyrate and lactate.
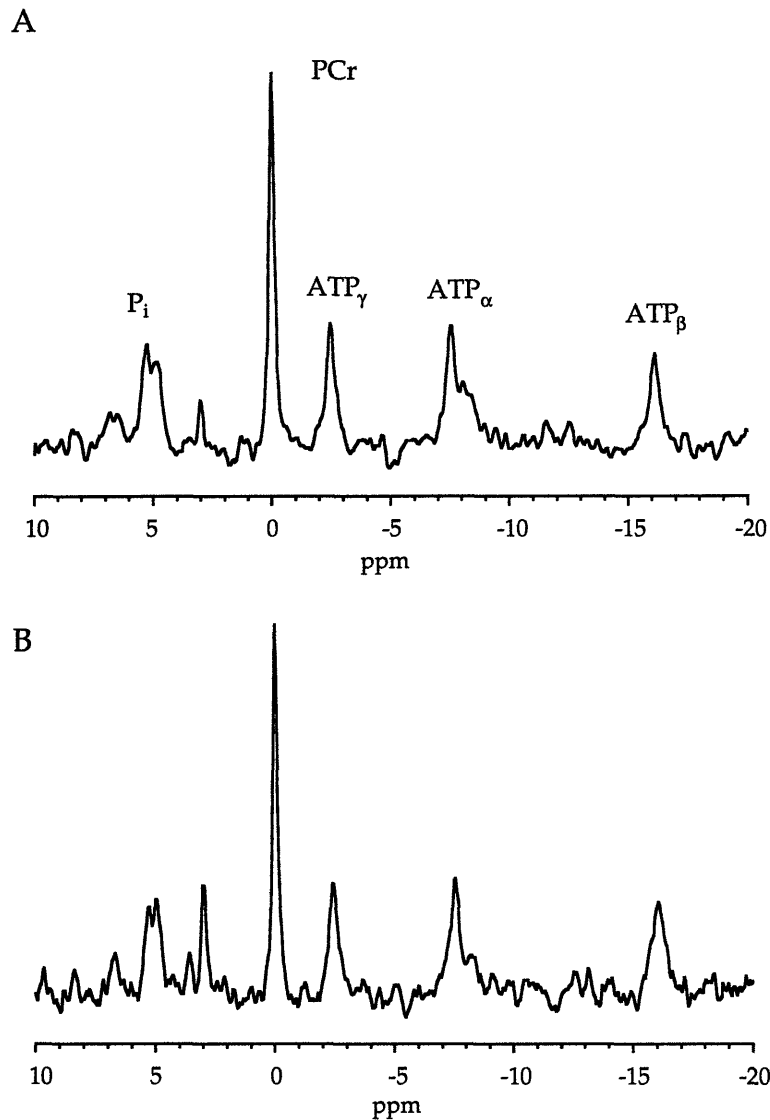
Figure 5.4 Representative ^{31}P spectra from isolated hearts. Hearts were perfused with either 2.5 mM [2-13C] butyrate only (A) or 2.5 mM [2-13C] butyrate plus 2.5 mM 12C lactate (B). Labeled peaks are inorganic phosphate (Pi), phosphocreatine (PCr), and the three phosphates of ATP (ATP$_\alpha$, ATP$_\beta$, and ATP$_\gamma$). There is no difference in high energy phosphate metabolism between the two groups. pH values were also similar as indicated by the chemical shift of Pi.

^{31}P spectra showed no difference in high energy phosphate metabolism between two groups over the course of perfusion (Figure 5.4). The phosphocreatine to ATP ratios (PCr/ATP) were similar at 2.27 ± 0.50 with butyrate only and 2.11 ± 0.23 with both butyrate and lactate. Consistent with previous findings with lactate perfused hearts (68), no significant changes were found in intracellular pH determined from the chemical shift of inorganic phosphate: 7.25 ± 0.20 for hearts perfused with butyrate only and 7.24 ± 0.17 for hearts perfused with butyrate plus lactate.
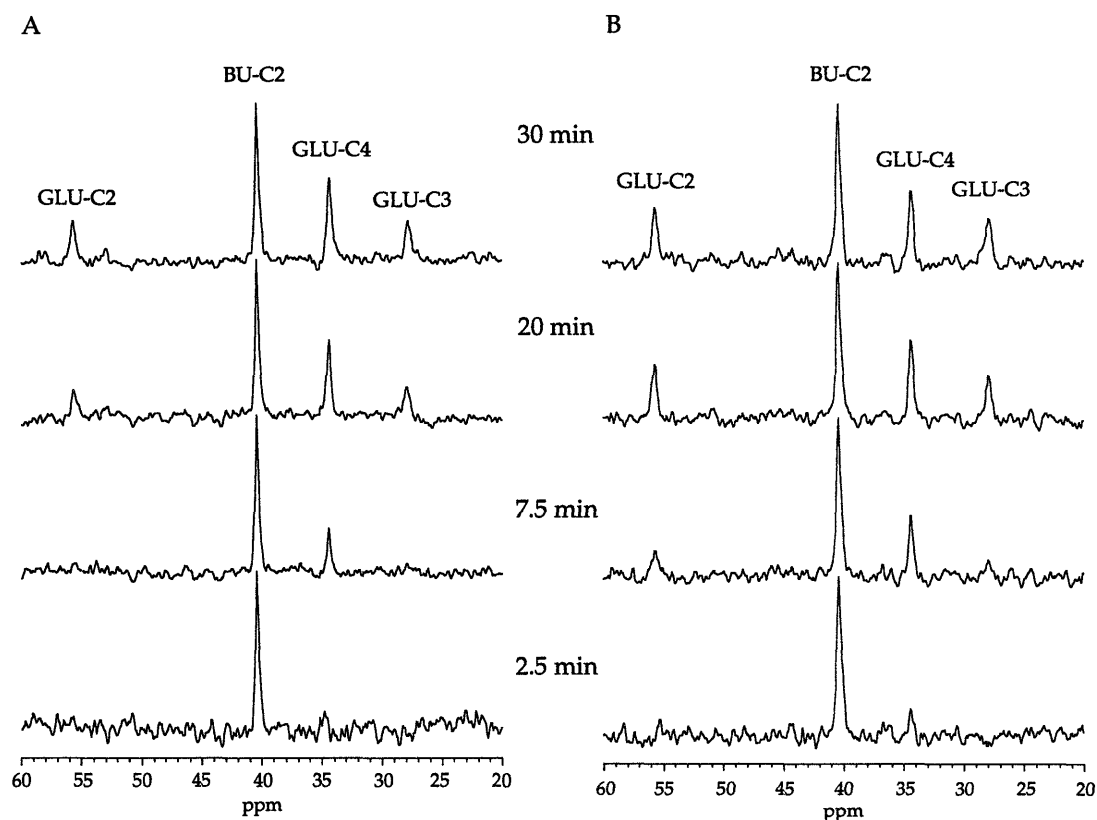
Figure 5.5 Effect of lactate on dynamic ^{13}C NMR spectra from isolated hearts. Each spectrum represents 64 scans over 2.5 minute interval at different time of perfusion. Peak assignments are: GLU-C2, 2-carbon of glutamate; GLU-C3, 3-carbon of glutamate; GLU-C4, 4-carbon of glutamate; BU-C2, 2-carbon of butyrate. (A) Spectra from heart perfused with 2.5 mM [2-^{13}C] butyrate only; (B) Spectra from heart perfused with 2.5 mM [2-^{13}C] butyrate and 2.5 mM unlabeled lactate. Note that heart perfused with both butyrate and lactate showed more rapid incorporation of ^{13}C into the 4- and 2-carbons of glutamate.

The evolution of the multiple ^{13}C enrichment sites in glutamate was monitored by sequential acquisition of ^{13}C NMR spectra from intact hearts. Representative changes in ^{13}C NMR spectra, reflecting the turnover of carbon

isotope within the glutamate pool, are shown in Fig 5.5. Spectra from heart perfused with both butyrate and lactate shows early incorporation of ^{13}C label into the glutamate pool at both 4- and 2-carbons as compared to that of heart perfused with butyrate only, clearly indicating that cytosolic redox state can also influence the enrichment rate of glutamate.

Enrichment curves for the 2- and 4-carbons of glutamate are shown in Figure 5.6, along with the results of the kinetic analysis by least-square fitting of the model (solid line) to the data shown in the figure. In both groups, the correlation coefficient between the NMR data and the fitted curves was greater than 0.98. The obvious difference in enrichment rates between the two groups, as shown in Figure 5.6, was not accounted for by oxygen consumption rates. Consistent with similar levels of mechanical work and respiratory rates, the TCA cycle flux was also very similar between two groups: 9.66±0.45 µmoles/min/g dry weight with butyrate alone and 10.17±0.29 with both butyrate and lactate. However, the interconversion rate between α-ketoglutarate and glutamate increased more than four-fold, from 3.11±0.21 to 14.33±1.97 µmoles/min/g dry weight. These data indicate increased metabolite transport rate across the mitochondrial membrane due to stimulated malate-aspartate shuttle activity in response to elevated cytosolic redox state.

As reducing equivalents generated in the cytosol are shuttled into mitochondria for electron transfer, an unknown portion of oxygen will be consumed in oxidizing cytosolic reducing equivalents. Qualitatively, at a constant rate of ATP generation, increased flux through malate-aspartate shuttle must be compensated by a decreased flux in the TCA cycle. Therefore, the use of oxygen consumption to calculate the TCA cycle flux becomes less reliable in this case. Data fitting was also performed without the constraint from measured oxygen consumption for the group with both butyrate and lactate. Both TCA cycle flux and interconversion rate showed no significant deviation from previous fitting with the constraint. The TCA cycle flux was slightly lower at 9.31±0.87 µmoles/min/g dry weight and the interconversion rate increased slightly to 18.60±5.32 µmoles/min/g dry weight. Again, this interconversion rate was more than four-fold higher than that from hearts perfused only with butyrate.
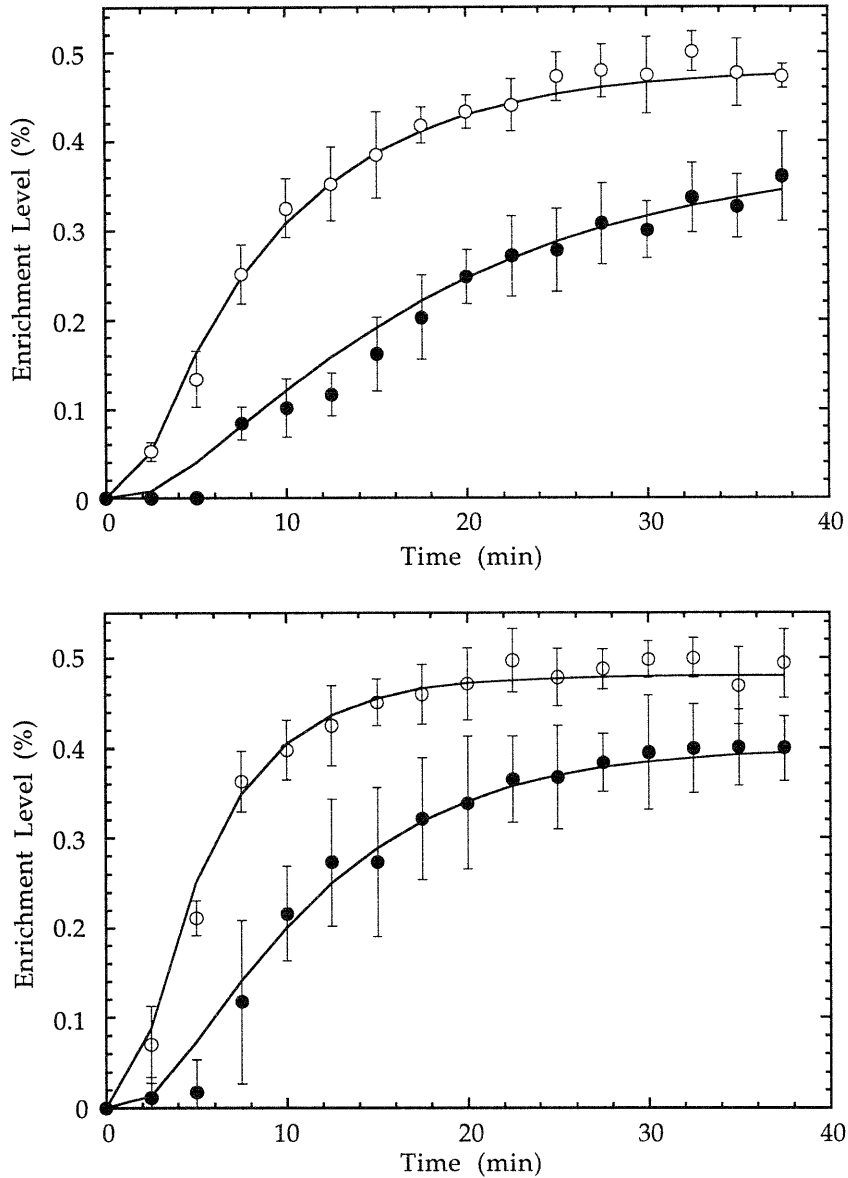
Figure 5.6 Time course of ^{13}C enrichment at different cytosolic redox states. Open circles: ^{13}C enrichment of glutamate at 4-carbon; closed circles: ^{13}C enrichment of glutamate at 2-carbon. Solid lines are the least-square fittings of the kinetic model to NMR data. Upper panel: perfusion with 2.5 mM [2-^{13}C] butyrate only (n=5); lower panel: perfusion with 2.5 mM [2-^{13}C] butyrate + 2.5 mM unlabeled lactate (n=5).

5.4 Discussion

Studies described in this chapter were designed primarily to investigate the interaction of malate-aspartate shuttle with the TCA cycle. The results of

this work show directly, for the first time, that the exchange rates of metabolic intermediates between subcellular compartments responds to physiological perturbations of cell metabolism in intact organs. The data also demonstrate that ^{13}C NMR is sensitive to both chemical exchange and, more importantly, to the transport of metabolites between subcellular compartments.

While the previous study has shown that the interconversion between α-ketoglutarate and glutamate involves metabolite transport between subcellular compartments and is another rate-limiting step in glutamate enrichment (140), this study further explored this particular component by introducing metabolic perturbations to change the transport rate. Several investigators have used transaminase inhibitors to study the effect of changed interconversion rate on glutamate enrichment kinetics (133, 142). However, the use of inhibitors to explore the rate-limiting components is inappropriate, as inhibition will cause any step in the kinetic process, even rapid processes, to become rate-limiting. The current protocol was designed to probe the physiological contributions of metabolite transport by stimulating, rather than inhibiting, this potential rate-determining step.

The stimulation of metabolite exchange across the mitochondrial membrane was achieved through the activation of the cytosolic redox-dependent malate-aspartate shuttle activity. This activation occurred via elevated cytosolic redox state from the addition of lactate (109). During perfusion with labeled lactate and unlabeled butyrate, NADH production through the conversion of lactate to pyruvate was indicated from the production of [3-^{13}C] alanine. The [3-^{13}C] alanine detected by ^{1}H and ^{13}C NMR documented the reverse flux across the lactate dehydrogenase reaction. The absence of lactate oxidation through the TCA cycle in the presence of butyrate is consistent with the inhibition of pyruvate dehydrogenase activity by fatty acid oxidation (28, 45, 130). Therefore, the major effect of exogenous lactate was to increase cytosolic redox state ($NADH/NAD^{+}$). In addition, the interaction of malate-aspartate shuttle with the TCA cycle induced a redistribution of metabolites among the TCA cycle intermediates and amino acid pools.

The influence of cytosolic redox state on the malate-aspartate shuttle activity was apparent in the observed ^{13}C enrichment of the glutamate pool

in intact, functioning heart. Least-square fitting of a simple compartment model to these NMR data shown that the increase in malate-aspartate shuttle activity induced a more than four-fold increase in the interconversion rate between α-ketoglutarate and glutamate. The transaminase activity responsible for the exchange of label between α-ketoglutarate and glutamate follows simple ping-pong reaction kinetics (33). As was shown in both ^{31}P spectra and previous experiments, the delivery of exogenous lactate to healthy, well-perfused myocardium does not exceed the pH buffering capacity of the cell and thus pH was not a source of variation in enzyme activity in this study (68). Therefore, without the allosteric regulation of the transaminase or changes in tissue pH, the observed acceleration in the interconversion of α-ketoglutarate and glutamate was achieved by driving the malate-aspartate shuttle at an elevated cytosolic redox potential with 2.5 mM exogenous lactate (105, 109).

In summary, this study explored the potential of ^{13}C NMR to determine the rates of metabolite exchange across the mitochondrial membrane in intact functioning hearts. The results show directly that the NMR observed ^{13}C turnover in glutamate reflects the adjustments in metabolic communication between subcellular compartments in response to metabolic state of the cell. These findings have important impact on future investigations of the regulation of metabolic activities between subcellular compartments of the cell in support of the physiological functions in intact tissues, which previously has only been studied in isolated mitochondria with an artificial cytosolic environment. More immediately, considerations of additional rate-limiting steps among the processes contributing to carbon isotope turnover within the tissue glutamate pool open a new opportunity for current applications of ^{13}C NMR spectroscopy in the study of metabolic flux.

Chapter 6

Conclusions and Future Perspectives

Several major conclusions can be drawn from this study. They will be presented and discussed in this chapter.

First, pre-steady state ^{13}C NMR analysis provides information uniquely related to metabolic turnover in support of physiological functions. It allows continual metabolic evaluation of functioning hearts in a nondestructive way and therefore, can enrich our understanding of the intracellular processes that occur in response to various metabolic demands of physiological function. Given the complexity of the information contained in ^{13}C NMR spectra, a comprehensive evaluation requires mathematical treatment. However, a comprehensive model needs not be a complicated one. The kinetic model developed from this work has only nine differential equations and is the simplest model obtained so far. Yet it is equivalent to other more complicated models when applied to the analysis of dynamic ^{13}C NMR spectra. Furthermore, sensitivity analysis indicates that the labeling kinetics of glutamate is insensitive to changes in metabolite contents of the TCA cycle intermediates. Therefore, inaccuracies in the measurements of these metabolites can be tolerated in kinetic analysis.

This simple model should also be readily applicable to *in vivo* conditions, provided that constraint parameters are available from appropriate *in vivo* monitoring and a priori knowledge of metabolite pool sizes. As indicated by the study with [2,4-^{13}C] butyrate, the fractional enrichment of acetyl-CoA has no influence on the kinetics of glutamate labeling. Hence, ^{13}C NMR analysis of tissue extracts can be avoided while relative anaplerosis can be calculated from the steady-state enrichment levels of both the 4- can 2-carbons of glutamate. Furthermore, since the labeling kinetics of glutamate is minimally influenced by the pool sizes of TCA cycle intermediates and aspartate, as was shown in sensitivity analysis, only glutamate concentration needs to be accurately determined. The current model assumes instant enrichment of acetyl-CoA pool, which is a valid approximation for isolated heart. However, since *in vivo* heart derives a significant amount of carbon source from endogenous triacyglycerides, this assumption may no longer be

valid. In this case, it is necessary to obtain the ^{13}C enrichment curve of the plasma. By incorporating the transport of substrate into the model, acetyl-CoA enrichment can be extrapolated.

Consistent with previous findings about the glutamate-oxaloacetate transaminase (GOT), the flux through GOT in intact heart is indeed very fast as compared to the TCA cycle activity. However, the interconversion rate between α-ketoglutarate and glutamate was found to be at least 20 times slower than the flux through GOT. Data from isolated mitochondria indicate that about 90% glutamate is cytosolic. Hence, this slow interconversion rate is best explained by the slow transport rate across the mitochondrial membrane. The slow interconversion rate between α-ketoglutarate and glutamate also suggests another rate-limiting step in glutamate enrichment of ^{13}C label. Thus, it is unlikely that glutamate enrichment is solely determined by the TCA cycle flux. Therefore, care must be taken in interpreting ^{13}C NMR spectra of glutamate as a direct index of the TCA cycle activity unless a comprehensive evaluation is given.

To test whether metabolite transport accounts for the discrepancy between the transaminase rate and the interconversion rate, the effect of stimulated malate-aspartate shuttle on ^{13}C NMR observation was examined. Elevated cytosolic redox state increased the rate of isotope turnover in glutamate. While the TCA cycle flux was not influenced by the perturbation, the interconversion rate between α-ketoglutarate and glutamate increased by more than four folds. Thus, the effect of driving metabolite transport across the mitochondrial membrane via the redox-dependent malate-aspartate shuttle was reflected in dynamic ^{13}C NMR data with an increased interconversion rate between the TCA cycle intermediates and glutamate. These results show for the first time that dynamic ^{13}C NMR is sensitive not just to chemical exchange, but also to metabolite transport across the mitochondrial membrane.

Compartmentation of metabolic processes in living cells represents an important regulatory mechanism in coordinating energy production to cell functions. Metabolic communication between subcellular compartments is achieved largely by selective permeability of membranes to different metabolites, or carrier mediated transport, which allows for efficient control

of reaction pathways. Through the adjustment of metabolite distribution between the mitochondria and cytosol, the metabolic demands of overall physiological function by the cell can be translated to the energetic machinery of the mitochondria. The malate-aspartate shuttle interacts directly with the TCA cycle through carrier mediated transport of α-ketoglutarate, malate, aspartate, and glutamate across the mitochondrial membrane. However, the interaction of the malate-aspartate shuttle with the TCA cycle has only been studied in isolated mitochondria with an artificial cytosolic environment. The findings in this study offer an exciting new prospect for studying the physiochemical regulation between the mitochondrial and cytosolic compartments in intact, functioning tissues.

One immediate application of the methodologies developed in this study is the investigation of metabolic activity in diseased heart, such as post-ischemic heart. It was found that reduced isotope turnover in the glutamate pool occurs in heart with mechanical dysfunction after brief reversal ischemia, a disease caused by coronary artery occlusion (45, 67, 71, 132). Another poorly understood phenomenon, inefficient oxygen utilization in reperfused heart ("oxygen paradox"), is also related to the metabolic events in post-ischemic myocardium (26). The relatively normal rate of oxygen consumption in post-ischemic heart suggests that the TCA cycle flux may be normal and that a different rate-determining process may have caused the observed reduction in isotope turnover in glutamate pool. Preliminary study indicates that while the TCA cycle flux and transaminase activity remain normal, the rate of metabolite exchange across the mitochondrial membrane of the intact heart is reduced during post-ischemic contractile dysfunction (73). Further investigation using ^{13}C spectroscopic methods developed from this study will allow the potential defects in the oxidative metabolism of post-ischemic hearts to be elucidated by offering a comprehensive evaluation of both the biochemical and physiological performances of the heart.

Metabolite contents in the whole cell have been used as the pool sizes in the kinetic model. Therefore, the interconversion rate in the model is really a lumped factor that involves both transaminase flux and transport rate. The model needs to be further developed to incorporate the malate-aspartate shuttle and to localize the kinetics to the individual transporters so that absolute flux through the malate-aspartate shuttle and related transporters

can be determined. Such a model will be similar to that developed by Chatham *et al.* (19) yet with fewer equations. In this case, careful quantitative study of the distribution of intermediary metabolites within the cell will be of great importance. Several methods have been developed which attempt to estimate the content of metabolites in cytoplasm and mitochondria (126). Yet these methods have not reached the state where the conclusions about metabolite distribution can be accepted with confidence. However, there is rough agreement among those methods about the gradients for citrate, α-ketoglutarate, and malate (126), and these data can therefore be incorporated into the expanded model with confidence. By combining data obtained from isolated mitochondria study on individual transporter, such development will allow further insight into the communication and regulation of metabolic processes in different subcellular compartments.

References

1.   Bailey, I. A., D. G. Gadian, P. M. Matthews, G. K. Radda, and P. J. Seeley. Studies of metabolism in the isolated, perfused rat heart using ^{13}C NMR. *FEBS Letters* 123: 315-318, 1981.

2.   Balaban, R. S. NMR spectroscopy of the heart, part I. *Concepts in Magn. Reson.* 1: 15-26, 1989.

3.   Balaban, R. S. Regulation of oxidative phosphorylation in the mammalian cell. *Am. J. Physiol.* 258: C377-C389, 1990.

4.   Balaban, R. S., H. L. Kantor, L. A. Katz, and R. W. Briggs. Relation between work and phosphate metabolites in the in vivo paced mammalian heart. *Science* 232: 1121-1123, 1986.

5.   Bergmeyer, H. U. *Methods of enzymatic analysis*. New York: Academic Press, 1974.

6.   Bevington, P. R. *Data reduction and error analysis for the physical sciences*. New York: McGraw-Hill, Inc., 1969.

7.   Bittl, J. A., and J. S. Ingwall. The energetics of myocardial stretch: creatine kinase flux and oxygen consumption in the noncontracting rat heart. *Circ. Res.* 58: 378-383, 1986.

8.   Bittl, J. A., and J. S. Ingwall. Reaction rates of creatine kinase and ATP synthesis in the isolated rat heart. *J. Biol. Chem.* 260: 3512-3517, 1985.

9.   Bottomley, P. A. Human in vivo NMR spectroscopy in diagnostic medicine: clinical tool or research probe? *Radiology* 170: 1-15, 1989.

10.   Bowman, R. H. Effects of diabetes, fatty acids, and ketone bodies on tricarboxylic acid cycle metabolism in the perfused rat heart. *J. Biol. Chem.* 241: 3041-3048, 1966.

11.   Bremer, J., and H. Osmundsen. Fatty acid oxidation and its regulation. In: *Fatty Acid Metaboliosm and Its Regulation*, edited by S. Numa. New York: Elsivier Science Publishers B.V., 1984, p. 113-154.

12.   Bremer, J., and A. B. Wojtczak. Factors controlling the rate of fatty acid β-oxidation in rat liver mitochondria. *Biochim. Biophys. Acta* 280: 515-530, 1972.

13.   Bressler, R. Physiological-chemical aspects of fatty acid oxidation. In: *Lipid Metabolism*, edited by S. J. Wakil. New York: Academic Press, 1970.

14.   Brooks, W. M., and R. J. Willis. Determination of intracellular pH in the Langendorff-perfused guinea-pig heart by ^{31}P nuclear magnetic resonance spectroscopy. *J. Mol. Cell. Cardiol.* 17: 747-752, 1985.

15.   Carson, E. R., C. Cobelli, and L. Finkelstein. *The mathematical modeling of metabolic and endocrine systems: model formulation, identification, and validation*: New York: John Wiley & Sons, 1983.

16.   Cerdan, S., and J. Seelig. NMR studies of metabolism. *Annu. Rev. Biophys. Biophys. Chem.* 19: 43-67, 1990.

17.   Chance, E. M., S. H. Seeholzer, K. Kobayashi, and J. R. Williamson. Mathematical analysis of isotope labeling in the citric acid cycle with applications to ^{13}C NMR studies in perfused rat hearts. *J. Biol. Chem.* 258: 13785-13794, 1983.

18.   Chatham, J. C., and J. R. Forder. A ^{13}C-NMR study of glucose oxidation in the intact functioning rat heart following diabetes-induced cardiomyopathy. *J. Mol. Cell Cardiol.* 25: 1203-1213, 1993.

19.   Chatham, J. C., J. R. Forder, J. D. Glickson, and E. M. Chance. Calculation of absolute metabolic flux and the elucidation of the pathway of glutamate labeling in perfused rat heart by ^{13}C NMR spectroscopy and nonlinear least squares analysis. *J. Biol. Chem.* 270: 7999-8008, 1995.

20.   Cohen, S. M. Simlutaneous ^{13}C and ^{31}P NMR studies of perfused rat liver. *J. Biol. Chem.* 258: 14294-14308, 1983.

21.   Cohen, S. M., P. Glynn, and R. G. Shulman. [13]C study of gluconeogenesis from labeled alanine in hepatocytes from euthyroid and hyperthyroid rats. *Proc. Natl. Acad. Sci. USA* 78: 60-64, 1981.

22.   Cohen, S. M., S. Ogawa, and R. G. Shulman. ^{13}C NMR studies of gluconeogenesis in rat liver cells: utilization of labeled glycerol by cells from euthyroid and hyperthyroid rats. *Proc. Natl. Acad. Sci. USA* 76: 1603-1607, 1979.

23.   Cohen, S. M., R. G. Shulman, and A. C. MaLaughlin. Effects of ethanol on alanine metabolism in perfused mouse liver studies by ^{13}C NMR. *Proc. Natl. Acad. Sci. USA* 76: 4808-4812, 1979.

24.   Damico, L. A., L. T. White, X. Yu, and E. D. Lewandowski. Chemical versus insotopic equilibrium and the metabolic fate of glycolytic end products in the heart. *J. Mol. Cell Cardiol.* in press, 1996.

25.   de Jong, J. W. Myocardial energy metabolism. Dordrecht, The Netherlands: Martinus Nijhoff Publishers, 1988.

26.   Dean, E. N., M. Shalafer, and J. M. Nicklas. The oxygen consumption paradox of "stunned myocardium" in dogs. *Basic Res. Cardiol.* 85: 120-131, 1990.

27.   Dennis Jr, J. E. Non-linear least squares and equations. In: *State of the Art in Numerical Analysis*, edited by D. Jacobs Academic Press, 1977.

28.   Dennis, S. C., A. Padma, M. S. DeBuysere, and M. S. Olson. Studies on the regulation of pyruvate dehydrogenase in the isolated perfused rat heart. *J. Biol. Chem.* 254: 1252-1258, 1979.

29.   Döring, H. J. The isolated perfused heart according to Langendorff technique - function - application. *Physiologie Bohemoslovaca* 39: 481-504, 1990.

30.   Eakin, R. T., L. O. Morgan, C. T. Gregg, and N. A. Matwiyoff. Carbon-13 nuclear magnetic resonance spectroscopy of living cells and their metabolism of a specifically labeled ^{13}C substrate. *FEBS Lett.* 28: 259-264, 1972.

31.   Edgar, T. F., and D. M. Himmelblau. *Optimization of chemical processes*. New York: McGraw-Hill, Inc., 1988.

32.   Fahien, L. A., and M. Strmecki. Studies of gluconeogenic mitochondrial enzymes. II. The conversion of α-ketoglutarate by bovine liver mitochondrial glutamate dehydrogenase and glutamate-oxaloacetate transaminase. *Arch. Biochem. Biophys.* 130: 456-467, 1969.

33.   Fahien, L. A., and M. Strmecki. Studies of gluconeogenic mitochondrial enzymes. III. The conversion of α-ketoglutarate to glutamate by bovine liver mitochondrial glutamate dehydrogenase and glutamate-oxaloacetate transaminase. *Arch. Biochem. Biophys.* 130: 468-477, 1969.

34.   Fitzpatrick, S. M., H. P. Hetherington, K. L. Behar, and R. G. Shulman. The flux from glucose to glutamate in the rat brain in vivo as determined by ^1H-observed, ^{13}C-edited NMR spectroscopy. *J. Cereb. Blood Flow Metab.* 10: 170-179, 1990.

35.   Fralix, T. A., and R. S. Balaban. NMR spectroscopy of the heart, part II. *Concepts in Magn. Reson.* 1: 93-108, 1989.

36.   Fritz, I. B. The metabolic consequences of the effects of carnitine on long-chain fatty acid oxidation. In: *Cellular Compartmentalization and Control of Fatty Acid Metabolism*, edited by F. C. Gran. Oslo: Universitetsforlaget, 1968.

37.   Gadian, D. G., G. K. Radda, R. E. Richards, and P. J. Seely. ^{31}P NMR in living tissue: the road from a promising to an important tool in biology. In:

Biological Applications of Magnetic Resonance, edited by R. G. Shulman. New York: Academic Press, 1979, p. 463-535.

38.   Greville, G. D. Intracellular compartmentation and the citric acid cycle. In: *Citric Acid Cycle: Control and Compartmentation*, edited by J. M. Lowenstein. New York: Marcel Dekker, 1969, p. 1-136.

39.   Hansford, R. G., and L. Cohen. Relative importance of pyruvate dehydrogenase interconversion and feed-back inhibition in the effect of fatty acids on pyruvate oxidation by rat heart mitochondria. *Arch. Biochem. Biophys.* 191: 65-81, 1978.

40.   Hitzig, B. M., J. W. Prichard, H. L. Kantor, W. R. Ellington, J. S. Ingwall, G. T. Burt, S. I. Helman, and J. Koutcher. NMR spectroscopy as an investigative technique in physiology. *FASEB J.* 1: 22-31, 1987.

41.   Hore, P. J. A new methods for water suppression in the proton NMR spectra of aqueous solution. *J. Magn. Reson.* 54: 539-542, 1983.

42.   Hore, P. J. Solvent Suppression in Fourier Transform Nuclear Magnetic Resonance. *J. Mag. Reson.* 55: 283-300, 1983.

43.   Hutson, S. M., G. D. Williams, D. A. Berkich, K. F. LaNoue, and R. W. Briggs. A ^{31}P NMR study of mitochondrial inorganic phosphate visibility: effects of Ca^{2+}, Mn^{2+}, and the pH gradient. *Biochemistry* 31: 1322-1330, 1992.

44.   Idell-Wenger, J. A., L. W. Grotyohann, and J. R. Neely. Coenzyme A and carnitine distribution in normal and ischemic hearts. *J. Biol. Chem.* 253: 4310-4318, 1978.

45.   Johnston, D. L., and E. D. Lewandowski. Fatty acid metabolism and contractile function in the reperfused myocardium: multinuclear NMR studies of isolated rabbit hearts. *Circ. Res.* 68: 714-725, 1991.

46.   Katz, A. M. *Physiology of the heart.* New York: Raven Press, 1992.

47.   Katz, J., and N. Grunnet. Estimation of metabolic pathway in steady state in vitro. Rates of tricaboxylic acid and pentose cycles. *Techniques in Metabolic Research* B208: 1-18, 1979.

48.   Katz, L. N., and H. Feinberg. The relation of cardiac effort to myocardial oxygen consumption and coronary flow. *Circ. Res.* 6: 656-669, 1958.

49.   Kelleher, J. A. Analysis of tricarboxylic acid cycle using [^{14}C] citrate specific activity ratios. *Am. J. Physiol.* 248: E252-E260, 1985.

50.   Knoop, F. *Beitr. Chem. Physiol. Pathol.* 6: 150-162, 1904.

51.   Kobayashi, K., and J. R. Neely. Control of maximum rates of glycolysis in rat cardiac muscle. *Circ Res* 44: 166-175, 1979.

52.   Kornberg, H. L. Anaplerotic sequences and their role in metabolism. In: *Essays in Biochemistry*, edited by P. N. Campbell and G. D. Greville. New York: Academic Press, 1966, p. 1-31.

53.   Krebs, H. A., and W. A. Johnson. The role of citric acid in intermediate metabolism in animal tissues. *Enzymologia* 4: 148-156, 1937.

54.   Langendorff, O. Untersuchugen am überlebenden säugethierherzen. *Pflügers Arch.* 61: 291-332, 1895.

55.   LaNoue, K., W. J. Nicklas, and J. R. Williamson. Control of citric acid cycle activity in rat heart mitochondria. *J Biol Chem* 245: 102-111, 1970.

56.   LaNoue, K. F., J. Bryla, and D. J. P. Bassett. Energy-driven aspartate efflux from heart and liver mitochondria. *J. Biol. Chem.* 249: 7514-7521, 1974.

57.   LaNoue, K. F., J. Bryla, and J. R. Williamson. Feedback interactions in the control of citric acid cycle activity in rat heart mitochondria. *J. Biol. Chem.* 247: 667-679, 1972.

58.   LaNoue, K. F., and A. C. Schoolwerth. Metabolite transport in mammalian mitochondria. In: *Bioenergetics*, edited by L. Ernster. The Netherlands: Elsevier Science Publishers, 1984.

59.   LaNoue, K. F., and A. C. Schoolwerth. Metabolite transport in mitochondria. *Annu. Rev. Biochem.* 48: 871-922, 1979.

60.   LaNoue, K. F., E. I. Walajtys, and J. R. Williamson. Regulation of glutamate metabolism and interactions with the citric acid cycle in rat heart mitochondria. *J. Biol. Chem.* 248: 7171-7183, 1973.

61.   LaNoue, K. F., and J. R. Williamson. Interrelationships between malate-aspartate shuttle and citric acid cycle in rat heart mitochondria. *Metabolism* 20: 119-140, 1971.

62.   Laster, S. B., L. C. Becker, G. Ambrosio, and W. E. Jacobus. Reduced aerobic metabolic efficiency in globally "stunned" myocardium. *J. Mol. Cell. Cardiol.* 21: 419-426, 1989.

63.   Laughlin, M. R., J. Taylor, A. S. Chesnick, M. DeGroot, and R. S. Balaban. Pyruvate and lactate metabolism in the in vivo dog heart. *Am. J. Physiol.* 264: H2068-H2079, 1993.

64.   Levenberg, K. A method for the solution of certain problems in least squares. *Quart. Appl. Math.* 2: 164-168, 1944.

65.   Lewandowski, E. D. Metabolic heterogenity of carbon substrate utilization in mammalian heart: NMR determination of mitochondrial versus cytosolic compartmentation. *Biochemistry* 31: 8916-8923, 1992.

66.   Lewandowski, E. D. Nuclear magnetic resonance evaluation of metabolic and respiratory support of work load in intact rabbit hearts. *Circ. Res.* 70: 576-582, 1992.

67.   Lewandowski, E. D., M. Chari, R. Roberts, and D. Johnston. NMR studies of β-oxidation and short chain fatty acid metabolism in supporting improved contractile recovery of reperfused myocardium. *Am. J. Physiol.* 261: H354-H363, 1991.

68.   Lewandowski, E. D., L. A. Damico, L. T. White, and X. Yu. Cardiac responses to induced lactate oxidation: NMR analysis of metabolic equilibria. *Am. J. Physiol.* 269: H160-H168, 1995.

69.   Lewandowski, E. D., and C. Hulbert. Dynamic changes in ^{13}C NMR spectra of intact hearts under conditions of varied metabolic enrichment. *Magn. Reson. Med.* 19: 186-190, 1991.

70.   Lewandowski, E. D., and J. S. Ingwall. The physiological chemistry of energy production in the heart. In: *Hurst's the Heart: Arteries and Veins* (8th ed.), edited by J. W. Hurst. New York: McGraw-Hill, Inc., 1994, p. 153-164.

71.   Lewandowski, E. D., and D. L. Johnston. Reduced substrate oxidation in postischemic myocardium; ^{13}C and ^{31}P NMR analyses. *Am. J. Physiol.* 258: H1357-H1365, 1990.

72.   Lewandowski, E. D., and L. T. White. Pyruvate dehydrogenase influences postischemic heart function. *Circulation* 91: 2071-2079, 1995.

73.   Lewandowski, E. D., X. Yu, L. T. White, and L. A. Damico. Postischemic hearts display reduced metabolite exchange between mitochondrial and cytosolic compartments. *Circulation* 92: I-387, 1995.

74.   Malloy, C. R., A. D. Sherry, and F. M. Jeffrey. Carbon flux through citric acid cycle pathways in perfused heart by ^{13}C NMR spectroscopy. *FEBS Lett.* 212: 58-62, 1987.

75.   Malloy, C. R., A. D. Sherry, and F. M. H. Jeffrey. Analysis of tricarboxylic acid cycle of the heart using ^{13}C isotope isomers. *Am. J. Physiol.* 259: H987-H995, 1990.

76.   Malloy, C. R., A. D. Sherry, and F. M. H. Jeffrey. Evaluation of carbon flux and substrate selection through alternate pathways involving the citric acid cycle of the heart by ^{13}C NMR spectroscopy. *J. Biol. Chem.* 263: 6964-6971, 1988.

77.   Malloy, C. R., J. R. Thompson, F. M. H. Jeffrey, and A. D. Sherry. Contrubution of exogenous substrates to acetyl coenzyme A: Measurement by ^{13}C NMR under non-steady-state conditions. *Biochemistry* 29: 6756-6761, 1990.

78.   Marquardt, D. An algorithm for least-squares estimation of nonlinear parameters. *S.I.A.M. J. Appl. Math.* 11: 431-441, 1963.

79.   Martinez-Carrion, M., and D. Tiemeier. Mitochondrial glutamate-aspartate transaminase. I. Structural comparison with the supernatant isozyme. *Biochemistry* 6: 1715-1722, 1967.

80.   Masiakos, P. T., G. D. Williams, D. A. Berkich, M. B. Smith, and K. F. LaNoue. ^{31}P NMR saturation-transfer study of the in situ kinetics of the mitochondrial adenine nucleotide translocase. *Biochemistry* 30: 8351-8357, 1991.

81.   Mason, G. F., R. Gruetter, D. L. Rothman, K. L. Behar, R. G. Shulman, and E. J. Novotny. Simultaneous determination of the rates of the TCA cycle, glucose utilization, a-ketoglutarate/glutamate exchange, and glutamine synthesis in human brain by NMR. *J. Cereb. Blood Flow Metab.* 15: 12-25, 1995.

82.   Mason, G. F., D. L. Rothman, K. L. Behar, and R. G. Shulman. NMR determination of the TCA cycle rate and α-ketoglutarate/glutamate exchange rate in rat brain. *J. Cereb. Blood Flow Metab.* 12: 434-447, 1992.

83.   Mela-Riker, L. M. Regulation of mitochondrial activity in cardia cells. *Ann. Rev. Physiol.* 47: 645-663, 1985.

84.   Michuda, C. M., and M. Martinez-Carrion. The isozymes of glutamate-aspartate transaminase: mechanism of inhibition by dicarboxylic acids. *J. Biol. Chem.* 245: 262-269, 1970.

85.   Neely, J. R., H. Liebermeister, E. J. Battersby, and H. E. Morgan. Effect of pressure development on oxygen consumption by isolated rat heart. *Am. J. Physiol.* 212: 804-814, 1967.

86.   Neely, J. R., and H. E. Morgan. Relationship between carbohydrate and lipid metabolism and the energy balance of heart muscle. *Ann. Rev. Physiol.* 36: 413-459, 1974.

87.   Neely, J. R., and M. J. Rovetto. Techniques for perfusing Isolated rat hearts. *Methods Enzymol.* 39: 43-63, 1975.

88.   Neely, J. R., K. M. Whitmer, and S. Mochizuki. Effects of mechanical activity and hormones on myocardial glucose and fatty acid transport. *Circ. Res.* 37: 733-741, 1975.

89.   Neely, J. R., K. M. Whitmer, and S. Mochizuki. Effects of mechanical activity and hormones on myocardial glucose and fatty acid utilization. *Circ. Res.* 38: 22-29, 1976.

90.   Neurohr, K. J., E. J. Barrett, and R. G. Shulman. In vivo carbon-13 nuclear magnetic resonance studies of heart metabolism. *Proc. Natl. Acad. Sci. USA* 80: 1603-1607, 1983.

91.   Nuutinen, E. M., K. J. Peuhkurinen, E. P. Pietilainen, J. K. Hiltunen, and I. E. Hassinen. Elimination and replenishment of tricarboxylic acid-cycle intermediates in myocardium. *Biochem. J.* 194: 867-875, 1981.

92.   Opie, L. H. *The heart. Physiology and metabolism.* New York: Raven Press, 1991.

93.   Osbakken, M. Can cardiovascular disease be effectively evaluated with NMR spectroscopy? In: *NMR Techniques in the Study of Cardiovascular Structure and Function*, edited by M. Osbakken and J. Haselgrove. New YOrk: Futura Publishing Company, Inc., 1988, p. 207-237.

94.   Osbakken, M., and J. Haselgrove. NMR techniques in the study of cardiovascular structure and function. New York: Futura Publishing Company, Inc., 1988.

95.   Peuhkurinen, K. J. Regulation of the tricarboxylic acid cycle pool size in heart muscle. *J. Mol. Cell. Cardiol.* 16: 487-495, 1984.

96.   Peuhkurinen, K. J., E. M. Nuutinen, E. P. Pietilainen, J. K. Hiltunen, and I. E. Hassinen. Role of pyruvate carboxylation in the energy-linked regulation of pool sizes of tricarboxylic acid-cycle intermediates in the myocardium. *Biochem J* 208: 577-581, 1982.

97.   Randle, P. J. Interaction of metabolism and the physiological role of insulin. *Rec. Progr. Horm. Res.* 22: 1-44, 1966.

98.   Randle, P. J., P. J. England, and R. M. Denton. Control of the tricarboxylate cycle and its interactions with glycolysis during acetate utilization in rat heart. *Biochem J* 117: 677-695, 1970.

99.   Randle, P. J., and P. K. Tubbs. Carbohydrate and fatty acid metabolism. In: *Handbook of Physiology*. Bethesda, Maryland: American Physiology Society, 1979, p. 805-844.

100.   Robitaille, P.-M. L., D. P. Rath, A. M. Abduljalil, J. M. O'Donnell, Z. Jiang, H. Zhang, and R. L. Hamlin. Dynamic 13C NMR analysis of oxidative metabolism in the in vivo canine myocardium. *J. Biol. Chem.* 268: 26296-26301, 1993.

101.   Robitaille, P.-M. L., D. P. Rath, T. E. Skinner, and A. M. Abduljalil. Transaminase reaction rates, transport activities and TCA cycle analysis by post-steady state ^{13}C NMR. *Magn Reson Med* 30: 262-266, 1993.

102.   Rothman, D. L., K. L. Behar, H. P. Hetherington, J. A. den Hollander, M. R. Bendall, P. O. A. C., and R. G. Shulman. ^{1}H-observed/^{13}C-decoupled spectroscopic measurement of lactate and glutamate in the rat brain in vivo. *Proc. Natl. Acad. Sci. USA* 82: 1633-1637, 1985.

103.   Rothman, D. L., E. J. Novotny, G. I. Shulman, A. M. Howseman, O. A. C. Petroff, G. Mason, T. Nixon, C. C. Hanstock, J. W. Prichard, and R. G. Shulman. ^{1}H-^{13}C NMR measurements of 4-^{13}C glutamate turnover in human brain. *Proc. Natl. Acad. Sci. USA* 89: 9603-9606, 1992.

104.   Russell, R. R., and H. Taegtmeyer. Changes in citric acid cycle flux and anaplerosis antedate the functional decline in isolated rat hearts utilizing acetoacetate. *J. Clin. Invest.* 87: 384-390, 1991.

105.   Safer, B. The metabolic significance of the malate-aspartate cycle in heart. *Circ. Res.* 37: 527-533, 1975.

106.   Safer, B., and J. R. Williamson. Mitochondrial-cytosolic interactions in perfused rat heart; role of coupled transamination in repletion of citric acid cycle intermediates. *J. Biol. Chem.* 248: 2570-2579, 1973.

107.   Sagawa, K., L. Maughan, H. Suga, and K. Sunagawa. *Cardiac Contraction and the Pressure-Volume Relationship*. New York/Oxford: Oxford University Press, 1988.

108.   Salhany, J. M., G. M. Pieper, and S. Wu. ^{31}P nuclear magnetic resonance measurement of cardiac pH in perfused guinea-pig hearts. *J. Mol. Cell. Cardiol.* 11: 601-610, 1979.

109.   Scholz, T. D., M. R. Laughlin, R. S. Balaban, V. V. Kupriyanov, and F. W. Heineman. Effect of substrate on mitochondrial NADH, cytosolic redox state, and phosphorylated compounds in isolated hearts. *Am. J. Physiol.* 268: H82-H91, 1995.

110.   Sherry, A. D., C. Malloy, P. Zhao, and J. R. Thompson. Alterations in substrate utilization in the reperfused myocardium: A direct analysis by ^{13}C NMR. *Biochemistry* 31: 4833-4837, 1992.

111.   Sherry, A. D., C. R. Malloy, R. E. Roby, A. Rajagopal, and F. M. Jeffrey. Propionate metabilism in the rat heart by ^{13}C NMR spectroscopy. *Biochem. J.* 254: 593-598, 1988.

112.   Sherry, A. D., R. L. Nunnally, and R. M. Peshock. Metabolic studies of pyruvate- and lactate-perfused guinea pig hearts by ^{13}C NMR: determination of substrate preference by glutamate isotopomer distribution. *J. Biol. Chem.* 260: 9272-9279, 1985.

113.   Sherry, A. D., B. Sumegi, B. Miller, G. L. Cottam, S. Gavva, J. G. Jones, and C. R. Malloy. Orientation-conserved transfer of symetric Krebs cycle intermediates in mammalian tissue. *Biochemistry* 33: 6268-6275, 1994.

114.   Sherry, A. D., P. Zhao, A. Wiethoff, and C. R. Malloy. ^{13}C isotopomer analyses in intact tissue using {^{13}C} homonuclear decoupling. *Magn. Reson. Med.* 31: 374-379, 1994.

115.   Shipp, J. C. S., L. H. Opie, and D. Challoner. Fatty acid and glucose metabolism in the perfused heart. *Nature* 189: 1018-1019, 1961.

116.   Sillerud, L. O., and R. G. Shulman. Structure and metabolism of mammalian liver glycogen monitored by carbon-13 nuclear magnetic resonance. *Biochemistry* 22: 1087-1094, 1983.

117.   Slues, F. E., M. Ranson, and C. Liebecq. Mechanism of the exchanges catalysed by the oxoglutarate translocator of rat-heart mitochondria: kinetics of the exchange reactions between 2-oxoglutarate, malate and malonate. *Eur. J. Biochem.* 25: 207-217, 1972.

118.   Soboll, S., R. Elbers, R. Scholz, and H.-W. Heldt. Subcellular distribution of di- and tricarboxylates and pH gradients in perfused rat liver. *Hoppe-Seyler's Z. Physiol. Chem.* 361: 69-76, 1980.

119.   Stankewicz, M. J., S. Cheng, and M. Martinez-Carrion. Mitochondrial glutamate aspartate transaminase. Differential action of thiol reagents with the supernatant enzyme. *Biochemistry* 10: 2877-2884, 1971.

120.   Stern, J. R., A. Del Campillo, and I. Raw. Enzymes of fatty acid metabolism. I. General introduction; crystalline crotonase. *J. Biol. Chem.* 218: 971-983, 1956.

121.   Strisower, E. H., G. D. Kohler, and I. L. Chaikoff. Incorporation of acetate carbon into glucose by liver slices from normal and alloxan-diabetic rats. *J. Biol. Chem.* 198: 115-126, 1952.

122.   Taegtmeyer, H. Energy metabolism of the heart: from basic concepts to clinical applications. *Curr. Prob. Cardiol.* 19: 59-113, 1994.

123.   Taegtmeyer, H. On the inability of ketone bodies to serve as the only energy providing substrate for rat heart at physiological work load. *Basic Res. Cardiol.* 78: 435-450, 1983.

124.   Taegtmeyer, H. Six blind men explore an elephant: aspects of fuel metabolism and the control of tricarboxylic acid cycle activity in heart muscle. *Basic. Res. Cardiol.* 79: 322-336, 1984.

125.   Tischler, M. J., Pachence, J. R. Williamson, and K. F. LaNoue. Mechanism of glutamate-aspartate translocation across the mitochondrial membrane. *Arch. Biochem. Biophys.* 173: 448-461, 1976.

126.   Veech, R. L. Regulation of coenzyme potential by near equilibrium reactions. In: *Microenviroments and Metabolic Compartmentation,* edited by P. A. Srere and R. W. Estabrook. New York/San Francisco/London: Academic Press, 1978, p. 17-64.

127.   Voet, D., and J. G. Voet. *Biochemistry.* New York: John Wiley & Sons, Inc., 1990.

128.   Weiland, O. H. THe mammalian pyruvated dehydrogenase complex: structure and function. *Rev. Physiol. Biochem. Pharmacol.* 96: 125-170, 1983.

129.   Weinman, E. O., E. H. Strisower, and I. L. Chaikoff. Conversion of fatty acids to carbohydrate: Application of isotopes to this problem and role of the Krebs cycle as a synthetic pathway. *Physiol. Rev.* 37: 252-272, 1957.

130.   Weiss, R. G., V. P. Chacko, and G. Gerstenblith. Fatty acid regulation of glucose metabolism in the intact beating rat heart assessed by carbon-13 NMR spectroscopy: the critical role of pyruvate dehydrogenase. *J. Mol. Cell. Cardiol.* 21: 469-478, 1989.

131.   Weiss, R. G., S. T. Gloth, R. Kalil-Filho, V. P. Chacko, M. D. Stern, and G. Gerstenblith. Indexing tricarboxylic acid cycle flux in intact hearts by carbon-13 nuclear magnetic resonance. *Circ. Res.* 70: 392-408, 1992.

132.   Weiss, R. G., R. Kalil-Filho, A. Herskowitz, V. P. Chacko, M. Litt, M. D. Stern, and G. Gerstenblith. Tricarboxylic acid cycle activity in postischemic rat hearts. *Circulation* 87: 270-282, 1993.

133.   Weiss, R. G., M. D. Stern, C. P. d. Albuquerque, K. Vandegaer, V. P. Chacko, and G. Gerstenblith. Consequences of altered aspartate aminotransferase activity on ^{13}C-glutamate labeling by the tricarboxylic acid cycle in intact rat hearts. *Biochim. Biophys. Acta* 1243: 543-548, 1995.

134.   Whalen, W. J. Some factors influencing O_2 consumption of isolated heart muscle. *Am. J. Physiol.* 198: 1153-1156, 1960.

135.   Williamson, J. R. Mitochondrial function in the heart. *Ann. Rev. Physiol.* 41: 485-506, 1979.

136.   Williamson, J. R., and B. E. Corkey. Assays of intermediates of the citric acid cycle and related compounds by fluorometric enzyme methods. In: *Methods in Enzymology,* edited by J. M. Colowick. New York: Academic Press, 1969, p. 434-514.

137. Williamson, J. R., C. Ford, J. Illingworth, and B. Safer. Coordination of citric acid cycle activity with electron transport flux. *Circ. Res.* 38: 39-51, 1976.

138. Williamson, J. R., and K. Kobayashi. Use of the perfused rat heart to study cardiac metabolism: retrospective and prospective views. *Basic Res. Cardiol.* 79: 283-291, 1984.

139. Yu, X., N. M. Alpert, L. A. Damico, and E. D. Lewandowski. Kinetic analysis of ^{13}C turnover in intact hearts at varied flux rates due to workload and β-oxidation. *Second Scientific Meeting of Society of Magnetic Resonance*, San Francisco, California, 1994, p. 87.

140. Yu, X., L. T. White, C. Doumen, L. A. Damico, K. F. LaNoue, N. M. Alpert, and E. D. Lewandowski. Kinetic analysis of dynamic ^{13}C NMR spectra: metabolic flux, regulation, and compartmentation in hearts. *Biophysical J.* 69: 2090-2102, 1995.

141. Yu, X., L. T. White, and E. D. Lewandowski. Cytosolic redox state drives carbon flux across the mitochondrial membrane as shown by ^{13}C NMR of intact hearts. *Circulation* 92: I-771, 1995.

142. Zhao, P., A. J. Wiethoff, A. D. Sherry, and C. R. Malloy. ^{13}C NMR spectra of perfused rat hearts in the presence of the transaminase inhibitor, aminooxyacetate. *Third Scientific Meeting of the Society of Magnetic Resonance*, Nice, France, 1995, p. 301.

Appendix A　　　　Biochemical Assays

A.1　　Glutamate Assay

<u>Principle:</u>

$$\text{L-Glutamate} + \text{NAD}^+ + \text{H}_2\text{O} \xleftarrow{\quad GDH \quad} \alpha\text{-Ketoglutarate} + \text{NADH} + \text{H}^+$$

$$\text{NADH} + \text{INT} + \text{H}^+ \xrightarrow{\quad diaphorase \quad} \text{NAD}^+ + \text{Formazan}$$
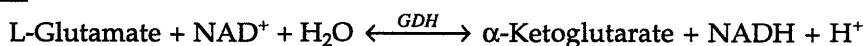
fomazan is measured in the visible range at 492 nm.

<u>Materials:</u>

Solution #1: potassium phosphate/triethanolamine buffer, pH 8.6; Triton X-100.
Solution #2: diaphorase from pig heart; NAD$^+$; stabilizer.
Solution #3: iodonitro tetrazolium chloride (INT) solution.
Solution #4: glutamate dehydrogenase (GDH) solution.

<u>Procedure:</u>

1. Pipette into cuvettes:

	Blank	Sample
Distilled H$_2$O	1 ml	950 µl
Solution #1	300 µl	300 µl
Solution #2	100 µl	100 µl
Sample Solution	-	50 µl
Solution #3	100 µl	100 µl

2. Mix, after 3 minutes read absorbances (A_i) of the solution at 492 nm;
3. Start the readtion by adding 15 ml GDH (solution #4);
4. Mix, wait until reaction has stopped (20 minutes), read absorbance (A_f);

<u>Calulation of glutamate concentrations:</u>

$$c = \frac{V}{\varepsilon \times l \times v} \times (A_f - A_i)$$

$$= 1.50754 \times \Delta A (\mu\text{moles} / \text{ml})$$

where　　V = total volume in cuvette (1.5 ml),

l = path length (1 cm),

ε = extinction coefficient (19.9 l/µmole/cm),

v = sample volume (50 ml),

ΔA = change in absorbance.

* ΔA should be at least 0.100 OD units for accuracy.

A.2   α-Ketoglutarate Assay

<u>Principle:</u>

$$\alpha\text{-Ketoglutarate} + \text{L-Aspartate} \xleftrightarrow{\quad GOT \quad} \text{L-Glutamate} + \text{Oxaloacetate}$$

$$\text{Oxaloacetate} + \text{NADH} + \text{H}^+ \xrightarrow{\quad MDH \quad} \text{L-Malate} + \text{NAD}^+$$
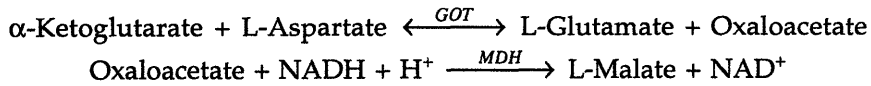
<u>Buffer components:</u>

Hepes	(50 mM)	1.19 gr	pH to 7.4;
Mg$_2$Cl$_2$	(10 mM)	0.203 gr	
EDTA	(5 mM)	1 ml of 0.5 M	
Distilled H$_2$0 to 100 ml			

<u>Procedures:</u>

1. Determine the exact concentration of an α-ketoglutarate standard solution (around 0.5 mM) using a spectrophotometer:

   - Make an assay cocktail: 10 ml buffer
     0.2 ml of 250 mM aspartate
     2 mg NADH
     20 units malate dehydrogenase (MDH)
   - In a 1 ml cuvette, add   1 ml assay cocktail
     200 µl sample
   - Read absorbance at 340 nm
   - Start reaction by adding 2 µl glutamate-oxaloacetate transaminase (GOT)
   - Calculate concentration:

   $$c = \frac{\Delta A}{6.22} \times \frac{V_{total}(1202\ \mu l)}{V_{sample}(200\ \mu l)} (\mu\text{moles} / \text{ml})$$

2. Fluorometrical determination:
   - Set up fluorometer to read excitation at 345 nm, emission at 450 nm
   - In a 3 ml cuvette, add   2.5 ml buffer
     40 µl 250 mM aspartate
     25 µl of 2 mg/ml NADH
     2 µl of MDH
     200 µl sample
   - Read fluorescence to make sure a steady state is obtained
   - Start the reaction with 2 µl GOT
   - Calculation:

   $$c_{spl} = \frac{\Delta F_{spl} + \Delta B}{\Delta F_{std} + \Delta B} \times \frac{V_{std}}{V_{spl}} \times c_{std}$$

   where ΔF_{spl} = change in fluoresence in the sample,

   ΔF_{std} = change in fluoresence in the standard solution,

   V_{spl} = sample volume added to cuvette (200 µl),

   V_{std} = volume of standard solution added to cuvette,

   c_{std} = concentration of the standard solution,

   ΔB = internal blank, i.e. baseline increase with the addition of GOT.

A.3   Aspartate Assay

<u>Principle:</u>

$$\text{L-Aspartate} + \alpha\text{-Ketoglutarate} \xleftrightarrow{GOT} \text{Oxaloacetate} + \text{L-Glutamate}$$

$$\text{Oxaloacetate} + \text{NADH} + \text{H}^+ \xrightarrow{MDH} \text{L-Malate} + \text{NAD}^+$$
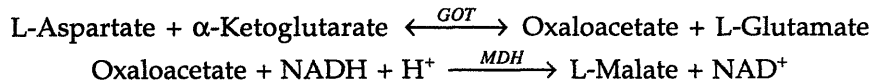
<u>Buffer components:</u>

Tra	(50 mM)
MgSO4	(5 mM)
EDTA	(5 mM)

<u>Procedures:</u>

1. Determine the exact concentration of an aspartate standard solution (around 0.5 mM) using a spectrophotometer:
   - In a 1 ml cuvette, add   1.5 ml buffer
     0.1 ml standard aspartate (0.5 mM)
     50 μl NADH (2 mg/ml)
     50 μl a-ketoglutarate (100 mM)
     5 μl MDH (1 mg/ml)
   - Read absorbance at 340 nm
   - Start reaction by adding 5 μl glutamate-oxaloacetate transaminase (GOT)
   - Calculate concentration:

$$c = \frac{\Delta A}{6.22} \times \frac{V_{total}(1.71\ ml)}{V_{sample}(0.1\ ml)} (\mu moles\,/\,ml)$$

2. Fluorometrical determination:
   - Set up fluometer to read excitation at 345 nm, emission at 450 nm
   - In a 3 ml cuvette, add   2.0 ml buffer
     20 μl 100 mM α-ketoglutarate
     20 μl of 2 mg/ml NADH
     5 μl of MDH
     200 μl sample (50 ml for 0.5 mM standard aspartate)
   - Read fluorescence to make sure a steady state is obtained
   - Start the reaction with 5 μl GOT
   - Calculation:

$$c_{spl} = \frac{\Delta F_{spl} + \Delta B}{\Delta F_{std} + \Delta B} \times \frac{V_{std}}{V_{spl}} \times c_{std}$$

where ΔF_{spl} = change in fluoresence in the sample,

ΔF_{std} = change in fluoresence in the standard solution,

V_{spl} = sample volume added to cuvette (200 μl),

V_{std} = volume of standard solution added to cuvette,

c_{std} = concentration of the standard solution,

ΔB = internal blank, i.e. baseline increase with the addition of GOT.

A.4   Citrate Assay

<u>Principle:</u>

$$\text{Citrate} \xleftrightarrow{CL, Mg^{++}} \text{Oxaloacetate + Acetate}$$

$$\text{Oxaloacetate + NADH + H}^+ \xrightarrow{MDH} \text{L-Malate + NAD}^+$$
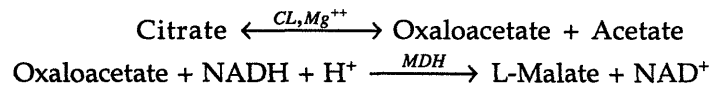
<u>Buffer:</u>

Hepes	(50 mM)	1.19 gr	pH to 7.4
Mg_2Cl_2	(10 mM)	0.203 gr	
EDTA	(5 mM)	1 ml of 0.5 M	
Distilled H_2O to 100 ml			

<u>Procedures:</u>
- Make an assay cocktail: 10ml buffer
    2 mg NADH
    20 units MDH (10 µl)
- In a 1 ml cuvette, add   1 ml assay cocktail
    300 µl sample
- Read absorbance at 340 nm
- Start reaction with 10 µl citrate lyase
- Calculate concentration:

$$c = \frac{\Delta A}{6.22} \times \frac{V_{total}(1310 \ \mu l)}{V_{sample}(300 \ \mu l)} (\mu \text{moles} / \text{ml})$$

Appendix B.   MATLAB Programs for the Analysis of ^{13}C NMR Spectra from Tissue Extracts

```
% INVITRO.m:
%            Analysis of the in vitro spectrum to determine Fc and y
%            (ref. CR Malloy, JBC 263, 1988)

clg
global data plthd plthd_dat hd_text1 hd_text2 hd_text3 hd_text4 hd_text5 hd_text6

% Glutamate C2
c2q1=2.90; c2q2=0.92; c2q3=2.55; c2q4=3.39;
c2d121=4.10; c2d122=7.01;
c2d231=19.81; c2d232=21.04;
c2s=57.73;
c2d12=c2d121+c2d122;
c2d23=c2d231+c2d232;
c2q=c2q1+c2q2+c2q3+c2q4;
c2=c2s+c2d12+c2d23+c2q;

% Glutamate C3
c3s=36.31;
c3d1=30.86; c3d2=29.53;
c3t1=5.59; c3t2=13.06; c3t3=6.89;
c3t=c3t1+c3t2+c3t3;
c3=c3t+c3s+c3d1+c3d2;

% Glutamate C4
c4s=100.00;
c4d1=28.78; c4d2=35.92;
c4d34=c4d1+c4d2;
c4=c4s+c4d34;

data=zeros(6,2);
data(:,1)=(1:6)';
data(1,2)=c2s/c2;
data(2,2)=c2d12/c2;
data(3,2)=c2d23/c2;
data(4,2)=c3s/c3;
data(5,2)=c3t/c3;
data(6,2)=c4d34/c4;

% Initial Fc and y values for data fitting
p0=[0.1 0.1];

% Setup graphics
figure(1)
set(1,'Name','In vitro Analysis: Fc & y');

C4_field1=uicontrol('Style','edit','Position',[.05 .12 .07 .05],...
            'Units','normalized','String',num2str(c4d1),...
```

```
                  'CallBack','c4d1=str2num(get(C4_field1,"String")); extdat');

C4_field2=uicontrol('Style','edit','Position',[.12 .12 .07 .05],...
                  'BackgroundColor','c','Units','normalized','String',num2str(c4s),...
                  'CallBack','c4s=str2num(get(C4_field2,"String")); extdat');

C4_field3=uicontrol('Style','edit','Position',[.19 .12 .07 .05],...
                  'Units','normalized','String',num2str(c4d2),...
                  'CallBack','c4d2=str2num(get(C4_field3,"String")); extdat');

C3_field1=uicontrol('Style','edit','Position',[.33 .12 .07 .05],...
                  'BackgroundColor','y','Units','normalized','String',num2str(c3t1),...
                  'CallBack','c3t1=str2num(get(C3_field1,"String")); extdat');

C3_field2=uicontrol('Style','edit','Position',[.40 .12 .07 .05],...
                  'Units','normalized','String',num2str(c3d1),...
                  'CallBack','c3d1=str2num(get(C3_field2,"String")); extdat');

C3_field3=uicontrol('Style','edit','Position',[.47 .12 .07 .05],...
                  'BackgroundColor','c','Units','normalized','String',num2str(c3s),...
                  'CallBack','c3s=str2num(get(C3_field3,"String")); extdat');

C3_field4=uicontrol('Style','edit','Position',[.54 .12 .07 .05],...
                  'BackgroundColor','y','Units','normalized','String',num2str(c3t2),...
                  'CallBack','c3t2=str2num(get(C3_field4,"String")); extdat');

C3_field5=uicontrol('Style','edit','Position',[.61 .12 .07 .05],...
                  'Units','normalized','String',num2str(c3d2),...
                  'CallBack','c3d2=str2num(get(C3_field5,"String")); extdat');

C3_field6=uicontrol('Style','edit','Position',[.68 .12 .07 .05],...
                  'BackgroundColor','y','Units','normalized','String',num2str(c3t3),...
                  'CallBack','c3t3=str2num(get(C3_field6,"String")); extdat');

C2_field1=uicontrol('Style','edit','Position',[.05 .05 .07 .05],...
                  'Units','normalized','String',num2str(c2q1),...
                  'CallBack','c2q1=str2num(get(C2_field1,"String")); extdat');

C2_field2=uicontrol('Style','edit','Position',[.12 .05 .07 .05],...
                  'BackgroundColor','y','Units','normalized','String',num2str(c2d121),...
                  'CallBack','c2d121=str2num(get(C2_field2,"String")); extdat');

C2_field3=uicontrol('Style','edit','Position',[.19 .05 .07 .05],...
                  'BackgroundColor','m','Units','normalized','String',num2str(c2d231),...
                  'CallBack','c2d231=str2num(get(C2_field3,"String")); extdat');

C2_field4=uicontrol('Style','edit','Position',[.26 .05 .07 .05],...
                  'Units','normalized','String',num2str(c2q2),...
                  'CallBack','c2q2=str2num(get(C2_field4,"String")); extdat');

C2_field5=uicontrol('Style','edit','Position',[.33 .05 .07 .05],...
                  'BackgroundColor','c','Units','normalized','String',num2str(c2s),...
                  'CallBack','c2s=str2num(get(C2_field5,"String")); extdat');
```

```
C2_field6=uicontrol('Style','edit','Position',[.40 .05 .07 .05],...
            'Units','normalized','String',num2str(c2q3),...
            'CallBack','c2q3=str2num(get(C2_field6,"String")); extdat');

C2_field7=uicontrol('Style','edit','Position',[.47 .05 .07 .05],...
            'BackgroundColor','m','Units','normalized','String',num2str(c2d232),...
            'CallBack','c2d232=str2num(get(C2_field7,"String")); extdat');

C2_field8=uicontrol('Style','edit','Position',[.54 .05 .07 .05],...
            'BackgroundColor','y','Units','normalized','String',num2str(c2d122),...
            'CallBack','c2d122=str2num(get(C2_field8,"String")); extdat');

C2_field9=uicontrol('Style','edit','Position',[.61 .05 .07 .05],...
            'Units','normalized','String',num2str(c2q4),...
            'CallBack','c2q4=str2num(get(C2_field9,"String")); extdat');

C2S_field=uicontrol('Style','text','Position',[.78 .85 .20 .08],...
            'Units','normalized','BackgroundColor',[.5 .7 .5],...
            'ForegroundColor','black','String',['C2S=' num2str(data(1,2))],...
            'CallBack','extdat');

C2D12_field=uicontrol('Style','text','Position',[.78 .75 .20 .08],...
            'Units','normalized','BackgroundColor',[.5 .7 .5],...
            'ForegroundColor','black','String',['C2D12=' num2str(data(2,2))],...
            'CallBack','extdat');

C2D23_field=uicontrol('Style','text','Position',[.78 .65 .20 .08],...
            'Units','normalized','BackgroundColor',[.5 .7 .5],...
            'ForegroundColor','black','String',['C2D23=' num2str(data(3,2))],...
            'CallBack','extdat');

C3S_field=uicontrol('Style','text','Position',[.78 .55 .20 .08],...
            'Units','normalized','BackgroundColor',[.5 .7 .5],...
            'ForegroundColor','black','String',['C3S=' num2str(data(4,2))],...
            'CallBack','extdat');

C3T_field=uicontrol('Style','text','Position',[.78 .45 .20 .08],...
            'Units','normalized','BackgroundColor',[.5 .7 .5],...
            'ForegroundColor','black','String',['C3T=' num2str(data(5,2))],...
            'CallBack','extdat');

C4D34_field=uicontrol('Style','text','Position',[.78 .35 .20 .08],...
            'Units','normalized','BackgroundColor',[.5 .7 .5],...
            'ForegroundColor','black','String',['C4D=' num2str(data(6,2))],...
            'CallBack','extdat');

Fc_field=uicontrol('Style','text','Position',[.78 .25 .20 .08],...
            'Units','normalized','BackgroundColor','red',...
            'ForegroundColor','white','String','Fc=0.0',...
            'CallBack','extdat');

y_field=uicontrol('Style','text','Position',[.78 .15 .20 .08],...
            'Units','normalized','BackgroundColor','red',...
            'ForegroundColor','white','String','y=0.0',...
```

```
                'CallBack','extdat');

int_text=uicontrol('Style','text','Position',[.05 .20 .16 .05],...
                'Units','normalized','BackgroundColor','black',...
                'ForegroundColor','white','String','Initial Fc & y:');

p_field1=uicontrol('Style','edit','Position',[.22 .20 .10 .05],...
                'Units','normalized','String',num2str(p0(1)),...
                'CallBack','p0(1)=str2num(get(p_field1,"String")); extfit');

p_field2=uicontrol('Style','edit','Position',[.342 .20 .10 .05],...
                'Units','normalized','String',num2str(p0(2)),...
                'CallBack','p0(2)=str2num(get(p_field2,"String")); extfit');

start_button=uicontrol('Style','Pushbutton','Position',[.85 .04 .12 .08],...
                'Units','normalized','Callback','extfit','String','Start');

ax_smith=axes('Position',[.1 .30 .6 .65],'XLim',[1 6],'YLim',[0 1]);

plthd_dat=plot(data(:,1),data(:,2),'r.','MarkerSize',25,'EraseMode','xor');
hd_text1=text(1.1,data(1,2),'C2S','EraseMode','xor');
hd_text2=text(2.1,data(2,2),'C2D12','EraseMode','xor');
hd_text3=text(3.1,data(3,2),'C2D23','EraseMode','xor');
hd_text4=text(4.1,data(4,2),'C3S','EraseMode','xor');
hd_text5=text(5.1,data(5,2),'C3T','EraseMode','xor');
hd_text6=text(5.5,data(6,2),'C4D','EraseMode','xor');
hold on
plthd=plot(data(:,1),data(:,2),'EraseMode','xor');
axis([1 6 -.05 1]);

drawnow


% EXTDAT.m
%               called by invitro.m to calculate C2S, C2D12, C2D23, C3S, C3T, and C4D
%               from the in vitro carbon-13 spectrum and update the graphic display

global data plthd plthd_dat hd_text1 hd_text2 hd_text3 hd_text4 hd_text5 hd_text6

c2d12=c2d121+c2d122;
c2d23=c2d231+c2d232;
c2q=c2q1+c2q2+c2q3+c2q4;
c2=c2s+c2d12+c2d23+c2q;

c3t=c3t1+c3t2+c3t3;
c3=c3t+c3s+c3d1+c3d2;

c4d34=c4d1+c4d2;
c4=c4s+c4d34;

data=zeros(6,2);
data(:,1)=(1:6)';
data(1,2)=c2s/c2;
data(2,2)=c2d12/c2;
```

```
data(3,2)=c2d23/c2;
data(4,2)=c3s/c3;
data(5,2)=c3t/c3;
data(6,2)=c4d34/c4;


set(C2S_field,'String',['C2S=' num2str(data(1,2))]);
set(hd_text1,'Position',[1.1 data(1,2)]);
set(C2D12_field,'String',['C2D12=' num2str(data(2,2))]);
set(hd_text2,'Position',[2.1 data(2,2)]);
set(C2D23_field,'String',['C2D23=' num2str(data(3,2))]);
set(hd_text3,'Position',[3.1 data(3,2)]);
set(C3S_field,'String',['C3S=' num2str(data(4,2))]);
set(hd_text4,'Position',[4.1 data(4,2)]);
set(C3T_field,'String',['C3T=' num2str(data(5,2))]);
set(hd_text5,'Position',[5.1 data(5,2)]);
set(C4D34_field,'String',['C4D34=' num2str(data(6,2))]);
set(hd_text6,'Position',[5.3 data(6,2)]);
set(plthd_dat,'ydata',data(:,2))


% EXTFIT.m
%              called by INVITRO.m to determine Fc & y by data fitting

global data plthd

trace=1;
tol=0.0001;
p0
p=fmins('malloy',p0,[trace tol]);

set(Fc_field,'String',['Fc=' num2str(p(1))]);
set(y_field,'String',['y=' num2str(p(2))]);

drawnow


% MALLOY.m
%              objective function to be optimized by EXTFIT.m

function err=malloy(p)

global data plthd

Fc=p(1);
y=p(2);
y1=y+1;
y2=2*y1^2;
Fc0=1-Fc;
s=zeros(6,1);
s(1)=(y2-2*Fc*y1-Fc+Fc^2)/y2;
s(2)=Fc0*Fc/y2;
s(3)=Fc*(2*y1-Fc)/y2;
s(4)=Fc0*(Fc0+y)/y1;
s(5)=Fc^2/y1;
```

```
s(6)=Fc/(2*y+1);
set(plthd,'ydata',s)
%disp('Press any key to continue ...')
%pause

err=sum((data(:,2)-s).*(data(:,2)-s));
```

Appendix C   Optimization and Simulation Programs

```
%TCAVF.m:   Optimization program used to optimize flux parameters that determine the
%           labeling kinetics of glutamate C-4 and C-2 using Levenberg-Marquardt least
%           square optimization method. Simulation of presteady state labeling of C13 in
%           the TCA cycle metabolites is performed by solving the differential equations
%           that describe the labeling and the gradient of labeling.

clear
global Fc Y V F CIT aKG GLU MAL OAA ASP V0 V_err V_weight
global c4_dat c2_dat c4_std c2_std c4_err c2_err
global c4_hdl c2_hdl tlt glu4 glu2 akg4 akg2
global time tf ts M tlt

% Read in parameters
[prm, prm_file]=get_file('Name of the parameter file:','*.prm');
CIT=prm(1);
aKG=prm(2);
GLU=prm(3);
MAL=prm(4);
OAA=prm(5);
ASP=prm(6);
Fc=prm(7);
Y=prm(8);
Fc_err=prm(9);
V0=prm(10);
V_err=prm(11);
V_weight=prm(12);

% Read in NMR data
[data,data_file]=get_file('Name of the data file:','*.dat');
[M, N]=size(data);
time = data(:,1);
tf=time;
ts=tf-tf(1);
maxglu=max(data(:,2));
c4_dat = data(:,2)*(Fc+Fc_err)/maxglu;
c4_std = data(:,3)*Fc;  ·
c2_dat = data(:,4)*(Fc+Fc_err)/maxglu;
c2_std = data(:,5)*Fc;
c4_stdm=max(c4_std);
c2_stdm=max(c2_std);
c4_err=c4_std+(c4_std<2e-2)*c4_stdm;
c2_err=c2_std+(c2_std<2e-2)*c2_stdm;

savefile=input('Save in *.mat file? ','s');

% Plot the glutamate enrichment curves
figure(1)
clf
set(1,'Name','Curve Fitting','Position',[5 400 350 500])
ymax=0.5+(Fc>0.5)*0.5;
figure(2)
```

```
clf
set(2,'Name','13C Labeling & Gradient Curve','Position',[380 480 600 250])

figure(1)
subplot(2,1,1)
errorbar(time, c4_dat, c4_std)
hold on
plot(time,c4_dat,'k-')
c4_hdl=plot(time,c4_dat,'c-','EraseMode','xor');
plot(time,c4_dat,'r.', 'MarkerSize',15)
grid
xlabel('time(min)')
ylabel('C4 Concentration')
title(data_file)
axis([0 time(M) 0 ymax])

subplot(2,1,2)
errorbar(time, c2_dat, c2_std)
hold on
plot(time,c2_dat,'k-')
c2_hdl=plot(time,c2_dat,'c-','EraseMode','xor');
plot(time,c2_dat,'r.', 'MarkerSize',15,'EraseMode','none')
grid
xlabel('time(min)')
ylabel('C2 Concentration')
axis([0 time(M) 0 ymax])

disp('Now, start optimization ...')

% p vector:
%        p(2) = V -- TCA flux
%        p(1) = F -- interconversion flux

p0=input('Initial parameters ([F1 V-TCA])?');
tic
options=[];
options(1)=1;
options(2)=1e-3;
options(3)=1e-2;
options(16)=1e-2;
[p,OPTIONS,SSQ,J]=nleastsq('simu9',p0,options,'tca9_grad');
covar=covariance_new(p,SSQ,J)
error=OPTIONS(8);
err4=sum(SSQ(1:M).*SSQ(1:M));
err2=sum(SSQ(M+1:2*M).*SSQ(M+1:2*M));
disp(['TCAflux= ' num2str(p(2)) ',   aKG<->GLU= ' num2str(p(1))])
disp(['err4=' num2str(err4) ', err2=' num2str(err2)])
simu_time=toc/60

eval(['save ' savefile ' ;']);
```

```
%SIMU9.m:      simulation of presteady-state labeling of C13 in TCA cycle metabolits.
%              ssq returns the cost function that also includes the penalty term for MVO2.

function ssq = simu9(p)

% TCA intermediates:
%              CIT: citrate;
%              aKG: a-ketoglutarate;
%              GLU: glutamate;
%              MAL: malate;
%              OAA: oxaloacetate;
%              ASP: aspartate;

global Fc Y V F CIT aKG GLU MAL OAA ASP V0 V_err V_weight
global c4_dat c2_dat c4_std c2_std c4_err c2_err
global c4_hdl c2_hdl tlt glu4 glu2 akg4 akg2
global time tf ts M

V=p(2);
F=p(1);

% y vextor of fractional enrichment levels:
%              yd(1) = CIT-C4
%              yd(2) = aKG-C4
%              yd(3) = GLU-C4
%              yd(4) = CIT-C2
%              yd(5) = aKG-C2
%              yd(6) = GLU-C2
%              yd(7) = MAL-C3
%              yd(8) = OAA-C3
%              yd(9) = ASP-C3

t0=0.0;
tfinal=time(M);
yd0 = zeros(9,1);
tol=1e-3;

[td,yd]=ode45('model9',t0,tfinal,yd0,tol);
c4_sim=yd(:,3);
c2_sim=yd(:,6);
glu4=(mgh_integrate(td,c4_sim,tf)-mgh_integrate(td,c4_sim,ts))/time(1);
glu2=(mgh_integrate(td,c2_sim,tf)-mgh_integrate(td,c2_sim,ts))/time(1);
akg4=(mgh_integrate(td,yd(:,2),tf)-mgh_integrate(td,yd(:,2),ts))/time(1);
akg2=(mgh_integrate(td,yd(:,5),tf)-mgh_integrate(td,yd(:,5),ts))/time(1);
ssq=[(glu4-c4_dat)./c4_err; (glu2-c2_dat)./c2_err; V_weight*(V-V0)/V_err];

figure(1)
subplot(2,1,1)
tlt=['V=' num2str(V) ', F=' num2str(F)];
title(tlt)
set(c4_hdl,'ydata',glu4)
set(c2_hdl,'ydata',glu2)

figure(2)
```

```
subplot(1,2,1)
plot(td,yd(:,1),'g-',td,yd(:,2),'r-',td,yd(:,3),'c-',  ...
    td,yd(:,4),'g:',td,yd(:,5),'r:',td,yd(:,6),'c:');
ylabel(tlt)
grid
```

%MODEL9.m: Mathematical description of the kinetic model of the TCA cycle enrichment
%   kinetics (9 equations).

```
function ydp = model9(td,yd)

global Fc Y V F CIT aKG GLU MAL OAA ASP

% yd vextor of fractional enrichment levels:
%           yd(1) = CIT-C4
%           yd(2) = aKG-C4
%           yd(3) = GLU-C4
%           yd(4) = CIT-C3
%           yd(5) = aKG-C3
%           yd(6) = GLU-C3
%           yd(7) = MAL-C3
%           yd(8) = OAA-C3
%           yd(9) = ASP-C3

B=zeros(9,9);
B(1,1)=-V/CIT;                                                       % CIT-C4
B(2,1)=V/aKG;       B(2,2)=-(F+V)/aKG;      B(2,3)=F/aKG;           % aKG-C4
B(3,2)=F/GLU;       B(3,3)=-F/GLU;                                   % GLU-C4
B(4,4)=-V/CIT;      B(4,8)=V/CIT;                                    % CIT-C3
B(5,4)=V/aKG;       B(5,5)=-(F+V)/aKG;      B(5,6)=F/aKG;           % aKG-C3
B(6,5)=F/GLU;       B(6,6)=-F/GLU;                                   % GLU-C3
B(7,2)=V/2/MAL;     B(7,5)=V/2/MAL;         B(7,7)=-(1+Y)*V/MAL;    % MAL-C3
B(8,7)=V/OAA;       B(8,8)=-(F+V)/OAA;      B(8,9)=F/OAA;           % OAA-C3
B(9,8)=F/ASP;       B(9,9)=-F/ASP;                                   % ASP-C3

ui=zeros(9,1);
ui(1,1)=V*Fc/CIT;

ydp=B*[yd(1),yd(2),yd(3),yd(4),yd(5),yd(6),yd(7),yd(8),yd(9)]'+ui;
```

%TCA9_GRAD.m: gradient(d*/dF) and (d*/dV) of TCA model.
%   function returns a transposed Jacobian matrix:
%
%   df/dF   0
%   df/dV   1/V_err

function glu_dFdV=tca9_grad(p)

% y vextor of fractional enrichment levels:
%   y(1) = CIT-C4
%   y(2) = aKG-C4
%   y(3) = GLU-C4
%   y(4) = CIT-C3
%   y(5) = aKG-C3
%   y(6) = GLU-C3
%   y(7) = MAL-C3
%   y(8) = OAA-C3
%   y(9) = ASP-C3
%   y(10) = d(CIT-C4)/dF
%   y(11) = d(aKG-C4)/dF
%   y(12) = d(GLU-C4)/dF
%   y(13) = d(CIT-C3)/dF
%   y(14) = d(aKG-C3)/dF
%   y(15) = d(GLU-C3)/dF
%   y(16) = d(MAL-C3)/dF
%   y(17) = d(OAA-C3)/dF
%   y(18) = d(ASP-C3)/dF
%   y(19) = d(CIT-C4)/dV
%   y(20) = d(aKG-C4)/dV
%   y(21) = d(GLU-C4)/dV
%   y(22) = d(CIT-C3)/dV
%   y(23) = d(aKG-C3)/dV
%   y(24) = d(GLU-C3)/dV
%   y(25) = d(MAL-C3)/dV
%   y(26) = d(OAA-C3)/dV
%   y(27) = d(ASP-C3)/dV

global Fc Y V F CIT aKG GLU MAL OAA ASP V0 V_err
global c4_dat c2_dat c4_std c2_std c4_err c2_err
global time tf ts M tlt

t0=0.0;
tfinal=time(M);
y0=zeros(27,1);
tol=1e-3;
V=p(2);
F=p(1);
[t,y]=ode45('model_grad',t0,tfinal,y0,tol);
glu4_df=((mgh_integrate(t,y(:,12),tf)-mgh_integrate(t,y(:,12),ts))/time(1))./c4_err;
glu2_df=((mgh_integrate(t,y(:,15),tf)-mgh_integrate(t,y(:,15),ts))/time(1))./c2_err;
glu4_dv=((mgh_integrate(t,y(:,21),tf)-mgh_integrate(t,y(:,21),ts))/time(1))./c4_err;
glu2_dv=((mgh_integrate(t,y(:,24),tf)-mgh_integrate(t,y(:,24),ts))/time(1))./c2_err;
glu_dFdV=[glu4_df' glu2_df' 0.0; glu4_dv' glu2_dv' 1/V_err];
%size(glu_dF)

```
figure(2)
subplot(1,2,2)
plot(time,glu4_df,'m-',time,glu4_dv,'c-', time,glu2_df,'m--',time,glu2_dv,'c--');
grid
ylabel(tlt)
```

%MODEL_GRAD.m: Mathematical description of the kinetic model of TCA
%   cycle metabolism with gradient calculated for optimization

function yp = model_grad(t,y)

% y vextor of fractional enrichment levels:
%   y(1) = CIT-C4
%   y(2) = aKG-C4
%   y(3) = GLU-C4
%   y(4) = CIT-C3
%   y(5) = aKG-C3
%   y(6) = GLU-C3
%   y(7) = MAL-C3
%   y(8) = OAA-C3
%   y(9) = ASP-C3
%   y(10) = d(CIT-C4)/dF
%   y(11) = d(aKG-C4)/dF
%   y(12) = d(GLU-C4)/dF
%   y(13) = d(CIT-C3)/dF
%   y(14) = d(aKG-C3)/dF
%   y(15) = d(GLU-C3)/dF
%   y(16) = d(MAL-C3)/dF
%   y(17) = d(OAA-C3)/dF
%   y(18) = d(ASP-C3)/dF
%   y(19) = d(CIT-C4)/dV
%   y(20) = d(aKG-C4)/dV
%   y(21) = d(GLU-C4)/dV
%   y(22) = d(CIT-C3)/dV
%   y(23) = d(aKG-C3)/dV
%   y(24) = d(GLU-C3)/dV
%   y(25) = d(MAL-C3)/dV
%   y(26) = d(OAA-C3)/dV
%   y(27) = d(ASP-C3)/dV

global Fc Y V F CIT aKG GLU MAL OAA ASP

```
A=zeros(27,27);
A(1,1)=-V/CIT;                                              % CIT-C4
A(2,1)=V/aKG;      A(2,2)=-(F+V)/aKG;   A(2,3)=F/aKG;       % aKG-C4
A(3,2)=F/GLU;      A(3,3)=-F/GLU;                           % GLU-C4
A(4,4)=-V/CIT;     A(4,8)=V/CIT;                            % CIT-C3
A(5,4)=V/aKG;      A(5,5)=-(F+V)/aKG;   A(5,6)=F/aKG;       % aKG-C3
A(6,5)=F/GLU;      A(6,6)=-F/GLU;                           % GLU-C3
A(7,2)=V/2/MAL;    A(7,5)=V/2/MAL;      A(7,7)=-(1+Y)*V/MAL; % MAL-C3
A(8,7)=V/OAA;      A(8,8)=-(F+V)/OAA;   A(8,9)=F/OAA;       % OAA-C3
A(9,8)=F/ASP;      A(9,9)=-F/ASP;                          % ASP-C3
```

```
A(10,10)=-V/CIT;                                          % d(CIT-C4)/dF
A(11,2)=-1/aKG;           A(11,3)=1/aKG;
A(11,10)=V/aKG;           A(11,11)=-(F+V)/aKG;
A(11,12)=F/aKG;                                           % d(aKG-C4)/dF
A(12,2)=1/GLU;            A(12,3)=-1/GLU;
A(12,11)=F/GLU;           A(12,12)=-F/GLU;                % d(GLU-C4)/dF
A(13,13)=-V/CIT;          A(13,17)=V/CIT;                 % d(CIT-C3)/dF
A(14,5)=-1/aKG;           A(14,6)=1/aKG;
A(14,13)=V/aKG;           A(14,14)=-(F+V)/aKG;
A(14,15)=F/aKG;                                           % d(aKG-C3)/dF
A(15,5)=1/GLU;            A(15,6)=-1/GLU;
A(15,14)=F/GLU;           A(15,15)=-F/GLU;                % d(GLU-C3)/dF
A(16,11)=V/2/MAL;         A(16,14)=V/2/MAL;
A(16,16)=-(1+Y)*V/MAL;                                    % d(MAL-C3)/dF
A(17,8)=-1/OAA;           A(17,9)=1/OAA;
A(17,16)=V/OAA;           A(17,17)=-(F+V)/OAA;
A(17,18)=F/OAA;                                           % d(OAA-C3)/dF
A(18,8)=1/ASP;            A(18,9)=-1/ASP;
A(18,17)=F/ASP;           A(18,18)=-F/ASP;                % d(ASP-C3)/dF

A(19,1)=-1/CIT;           A(19,19)=-V/CIT;                % d(CIT-C4)/dV
A(20,1)=1/aKG;            A(20,2)=-1/aKG;
A(20,19)=V/aKG;           A(20,20)=-(F+V)/aKG;
A(20,21)=F/aKG;                                           % d(aKG-C4)/dV
A(21,20)=F/GLU;           A(21,21)=-F/GLU;                % d(GLU-C4)/dV
A(22,4)=-1/CIT;           A(22,8)=1/CIT;
A(22,22)=-V/CIT;          A(22,26)=V/CIT;                 % d(CIT-C3)/dV
A(23,4)=1/aKG;            A(23,5)=-1/aKG;
A(23,22)=V/aKG;           A(23,23)=-(F+V)/aKG;
A(23,24)=F/aKG;                                           % d(aKG-C3)/dV
A(24,23)=F/GLU;           A(24,24)=-F/GLU;                % d(GLU-C3)/dV
A(25,2)=1/2/MAL;          A(25,5)=1/2/MAL;
A(25,7)=-(1+Y)/MAL;       A(25,20)=V/2/MAL;
A(25,23)=V/2/MAL;         A(25,25)=-(1+Y)*V/MAL;          % d(MAL-C3)/dV
A(26,7)=1/OAA;            A(26,8)=-1/OAA;
A(26,25)=V/OAA;           A(26,26)=-(F+V)/OAA;
A(26,27)=F/OAA;                                           % d(OAA-C3)/dV
A(27,26)=F/ASP;           A(27,27)=-F/ASP;                % d(ASP-C3)/dV

u=zeros(27,1);
u(1,1)=V*Fc/CIT;
u(19,1)=Fc/CIT;

yp=A*[y(1),y(2),y(3),y(4),y(5),y(6),y(7),y(8),y(9),y(10), ...
      y(11),y(12),y(13),y(14),y(15),y(16),y(17),y(18), ...
      y(19),y(20),y(21),y(22),y(23),y(24),y(25),y(26),y(27)]'+u;
```